Doctoral Dissertation

Studies on Development of Organic Devices and Long-chain Molecular Wires Based on Fused π-Conjugated Molecules with High-efficient Hopping Transport

（高効率ホッピング伝導を示す縮環型π共役分子を基本骨格とした有機デバイスおよび長鎖分子ワイヤ開発に関する研究）

Ryo Asakawa

January 2025

Department of Applied Chemistry

Graduate School of Engineering

Osaka University

Preface

The study presented in this thesis has been carried out under the guidance of Professor Yutaka Ie at SANKEN (The Institute of Scientific and Industrial Research), Osaka University from April 2020 to March 2025.

This thesis concerns the synthesis, structure, properties, semiconducting characteristics and single molecule conductance of new fused π-conjugated molecules and long-chain molecular wires having high-efficient hopping transport characteristics by molecular modification. The objective of this work is to reveal the structure–property relationship of π-conjugated compounds having fused structure for application to molecular wires and organic semiconducting materials. The findings obtained in this study are not only expected to improve the single-molecule conductance characteristics through hopping conduction in long-chain molecular wires, but also to contribute to enhancing the efficiency of organic electronics, serving as a foundation for further developments in these fields.

Department of Applied Chemistry
Graduate School of Engineering
Osaka University

Suita, Osaka, Japan
January 2025

Ryo Asakawa

Table of Contents

General introduction

In 1974, Aviram and Ratner proposed that it would be possible to construct electronic devices at the single-molecule level by using organic molecules as elements, and this concept was named molecular electronics.[1] With the expected limits of miniaturization for conventional silicon semiconductors, molecular electronics is gaining attention as a promising candidate for next-generation devices. Unlike existing miniaturization processes, molecular electronics enables device fabrication through environmentally friendly, low-cost processes such as self-assembly, making it a promising candidate for green devices. To experimentally conduct research in molecular electronics, it is necessary to stably form metal/single-molecule/metal junctions (single-molecule junctions). From this perspective, extensive research has been conducted on the fabrication of single-molecule junctions and the measurement of their single-molecule conductance.[2] In 1997, Tour and colleagues succeeded in measuring the single-molecule conductance of 1,4-benzenedithiol bridged between a nano-gap formed by breaking gold nanowires on an elastic substrate (Fig. 1a).[3] Furthermore, in 2003, Tao and colleagues established the scanning tunneling microscope break junction (STM-BJ) method, which forms single-molecule junctions by bringing an STM metal probe into contact with a metal substrate (Fig. 1b).[4] On the other hand, in terms of molecular structure, single-molecule conductance measurements using STM-BJ have been conducted on relatively short molecules such as alkane dithiols and π-conjugated compounds like 1,4-benzenedithiol. Through these studies, the charge transport mechanism has been clarified, and correlations between molecular structure and the conductance properties within the molecule have been revealed.[5-8]

It is known that the intramolecular charge transport mechanism depends on the length of the molecule: coherent tunneling transport occurs in short molecular length whereas incoherent hopping transport occurs in several-nanometer-scale molecular length.[9] In hopping transport, charge carriers hop between localized electronic sites, called hopping sites. Charge flow in hopping transport can be articulated by the Arrhenius equation (eq 1).

$$k = Ae^{\frac{-E_a}{k_B T}} \qquad (1)$$

where k is the rate constant, A is the pre-exponential factor, k_B is the Boltzmann constant, T is the temperature, and E_a is the activation energy.

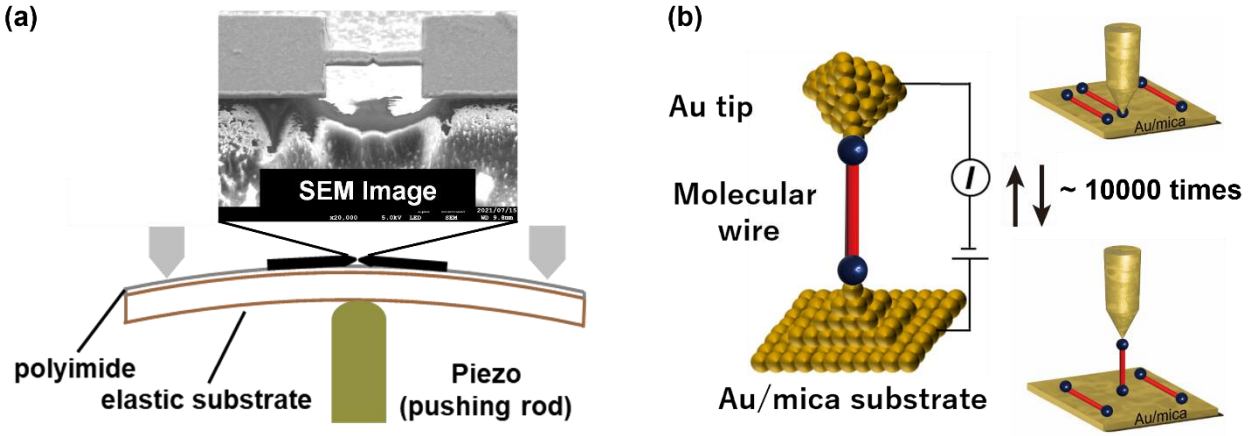

Figure 1. Schematic of (a) Mechanically controllable break junction (MCBJ) and (b) Scanning tunneling microscope (STM) break junction (STM-BJ).

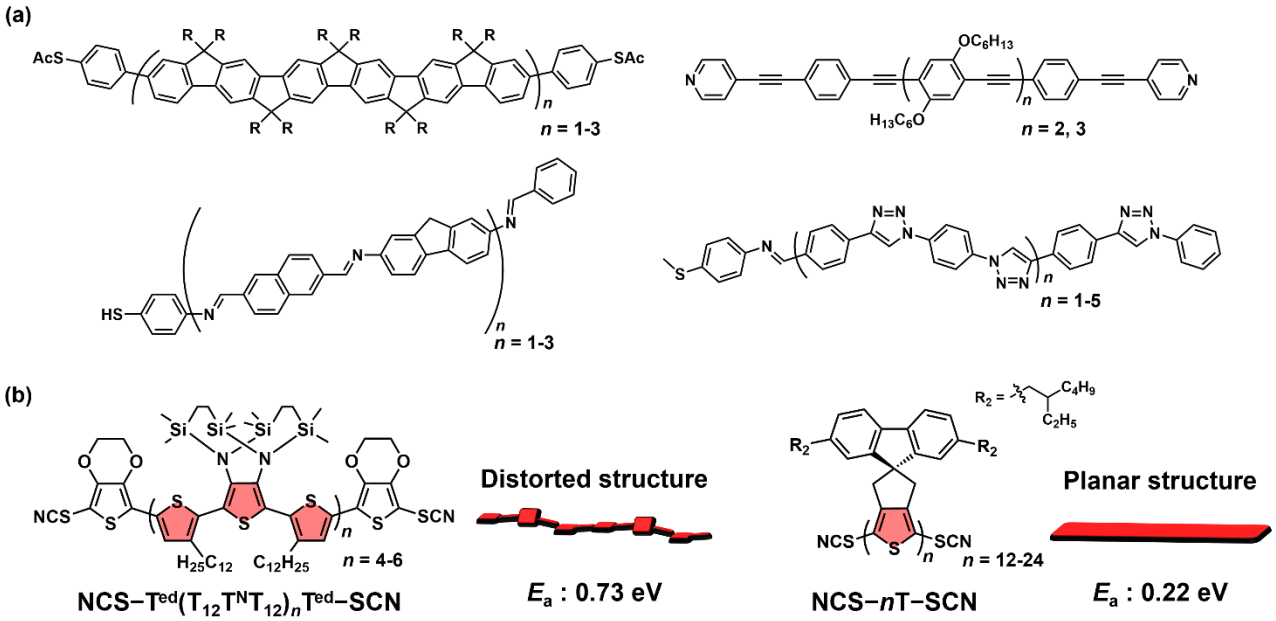

Figure 2. (a) Molecular structures of reported molecular wires with hopping-transport characteristics. (b) Molecular structures of oligothiophene-based molecular wires.

Thus, it is well known that intramolecular hopping efficiency shows temperature dependent. Reducing the activation energy (E_a), which is a key factor for improving the intramolecular hopping efficiency, is essential. From this perspective, it is important to clarify the correlation between the electronic structure of the hopping sites and E_a. As shown in Fig. 2a, long molecular wires have been developed and the relationship between hopping sites and E_a as well as single-molecule conductance has been experimentally investigated.[10-13] In 2019, Ie and coworkers succeeded in developing highly planer and completely insulated oligothiophenes **NCS−*n*T−SCN** (n = 12-24).[14] By comparing the single-molecule conductance of **NCS−*n*T−SCN** (n = 12-24) with non-planer oligothiophene **NCS−T^{ed}(T$_{12}$T^{N}T$_{12}$)$_n$T^{ed}−SCN** (n = 4-6),[15] they experimentally demonstrated the reduction of E_a and the enhancement of single-molecule conductance due to their highly planar structure (Fig. 2b). On the other hand, the correlation between hopping sites and single-molecule conductance remains largely unexplored. Thus, development of long molecular wires composed of a hopping site with a defined electronic structure and their single-molecule conductance measurements are desired.

Hopping conduction plays a critical role not only in molecular electronics but also in organic electronics, where organic semiconductor thin films serve as the active layers. In organic electronics, both intra- and inter-molecular hopping significantly influence charge transport properties.[16] Therefore, understanding the relationship between the electronic structure of organic semiconductors and their charge transport characteristics is crucial.

Against this background, this research focuses on the development of π-conjugated compounds where the electronic structure is defined as hopping sites, aiming to clarify the relationship among molecular structure, physical properties, and functions. The findings from this research will contribute not only to enhancing the single-molecule conductance properties of long-chain molecular wires but also to improving the efficiency of organic electronics, thus laying the foundation for further advancements in these fields.

The thesis consists of following three chapters:

Chapter 1 focuses on the development of a novel D-A-D type conjugated molecule containing naphtho[1,2-c:5,6-c']bis[1,2,5]thiadiazole (**NTz**) backbone, which has attracted attention due to its strong intermolecular interactions. The physical properties and semiconductor characteristics of this molecule were evaluated, and the correlation between its electronic structure and physical properties was investigated.

Chapter 2 aims to achieve efficient long-range intramolecular hopping transport. A molecular design strategy was proposed to reduce the activation energy required for hopping transport. Periodically twisted molecular wires based on a fused unit were developed. Single-molecule conductance measurements revealed that high-efficiency long-range hopping transport was realized through the reduction of activation energy.

Chapter 3 provides a detailed evaluation of the structural advantages of the hopping site **TBID** developed in chapter 2. A new hopping site, **BPB**, was designed by removing the fused structure from **TBID**. Compared to **TBID**, **BPB** exhibited a larger reorganization energy, injection barrier, and a broader distribution of the HOMO. Molecular wires composed of **BPB** showed lower single-molecule conductance than those composed of **TBID**. From this, it was concluded that the strategy of utilizing fused structures for hopping sites is crucial for improving intramolecular hopping charge transport.

References

1. Aviram, A.; Ratner, M. A. *Chem. Phys. Lett.*, **1974**, *29*, 277-283.
2. Lindsay, S. M.; Ratner, M. A. *Adv. Mater.* **2007**, *19*, 23-31.
3. Reed, A.; Zhou, C.; Muller, J.; Burgin, T.; Tour, M. J. *Science*, **1997**, *278*, 252-254.
4. Xu, B.; Tao, N. J. *Science* **2003***, 301*, 2332-1223.
5. Aradhya, V.; Venkataraman, L. *Nat*. *Nanotechnol*. **2013**, *8*, 399-410.
6. Metzger, M. *Chem*. *Rev*. **2015**, *115*, 5056-5115.
7. Su, A.; Neupane, M.; Steigerwald, L.; Venkataraman, L.; Nuckolls, C. *Nat*. *Rev*. *Mater*. **2016**, *1*, 16002.
8. Venkataraman, L.; Park, S.; Whalley, C.; Nuckolls, C.; Hybertsen, S.; Steigerwald, L. *Nano*. *Lett*. **2007**, *7*, 502-506.
9. Choi, H.; Kim, B.; Frisbie, D. *Science* **2008**, *320*, 1482-1486.
10. Hines, T.; Diez-Perez, I.; Hihath, J.; Liu, H.; Wang, Z.; Zhao, J.; Zhou, G.; Müllen, K.; Tao, N. *J*. *Am*. *Chem*. *Soc*. **2010**, *132*, 11658-11664.
11. Zhao, X.; Huang, C.; Gulcur, M.; Batsunov, A.; Baghernejad, M.; Hong, W.; Bryce, M.; Wandlowski, T. *Chem*. *Mater*. **2013**, *25*, 4340-4347.
12. Choi, H.; Risko, C.; Delgado, M.; Kim, B.; Brèdas, J.; Frisbie, D. *J*. *Am*. *Chem*. *Soc*. **2010**, *132*, 4358-4368.
13. Luo, L.; Frisbie, D. *J*. *Am*. *Chem*. *Soc*. **2010**, *132*, 8854-8855.
14. Ie, Y.; Okamoto, Y.; Inoue, T.; Tone, S.; Seo, T.; Honda, Y.; Tanaka, S.; Lee, S. K.; Ohto, T.; Yamada, R.; Tada, H.; Aso, Y. *J*. *Phys*. *Chem*. *Lett*. **2019**, *10*, 3197-3204.
15. Yamada, R.; Kumazawa, H.; Tanaka, S.; Tada, H. *Appl*. *Phys*. *Exp*. **2009**, *2*, 025002.
16. Saito, M.; Yamada, H.; Kranthiraja, K.; Jeon, J.; Kim, D.; Mikie, T.; Saeki, A.; Ohkita, H.; Osaka, I. *Commun*. *Mater*. **2023**, *4*, 72-81.

Chapter 1
Development of fused π-conjugated molecule containing naphthobisthiadiazole

1.1 Introduction

The development of fused π-conjugated molecules has attracted significant interest in recent years, with considerable efforts focused on the development of organic semiconducting materials for organic field-effect transistors (OFETs) and organic solar cells (OSCs).[1-8] Notably, oligorylene and oligoacene molecules have been reported to exhibit superior carrier transport characteristics in OFET devices.[9-12] Additionally, recent advancements in the use of nonfullerene acceptors in OSCs have heavily relied on fused π-conjugated molecules as central units.[13-16] One advantage of such fused π-conjugated frameworks is the small structural differences between neutral and charged species (cationic or anionic) — specifically, the low reorganization energy — which is beneficial for efficient charge transport. Another important molecular-level property is the ability to tune the electronic state, which allows for the incorporation of electron-withdrawing substituents such as fluorine, perfluoroalkyl, cyano, and imide groups into fused π-conjugated molecules.[17-23] In this context, the construction of donor (D)-acceptor (A) configurations has proven to be an effective molecular design strategy, with pyrazine, naphthalenediimide (**NDI**), perylenediimide (**PDI**), and benzothiadiazole (**BTz**) units commonly used as acceptor units in fused D-A-type molecules.[24-30] However, the development of fused D-A-D (hereafter referred to as DAD) π-conjugated systems has been hindered by the limited availability and synthetic accessibility of suitable acceptor units.

Naphtho[1,2-c:5,6-c']bis[1,2,5]thiadiazole (**NTz**) has been employed as an electron-accepting unit in π-conjugated systems.[31-33] However, chemical modifications to the **NTz** unit at the 4 and 9 positions are challenging. Recently, Ie and coworkers synthesized a fluorinated naphtho[1,2-c:5,6-c']bis[1,2,5]thiadiazole (**FNTz**) derivative as a novel electron-accepting unit, and developed a series of FNTz-based molecules as nonfullerene acceptors[34] and D-A-type donor copolymers.[35] (Fig. 1-1a). They also discovered that the fluorine atoms in **FNTz** could be replaced by cyano groups, and π-conjugated systems containing cyano-substituted **NTz** functioned effectively in OFET and OSC applications.[36] Building on these studies, the author hypothesized that functionalization at the 4 and 9 positions of **FNTz** could facilitate the further construction of fused DAD π-extended molecules (Fig. 1-1b). This chapter reports the design and synthesis of a new fused DAD molecule, **BDT-NTz**, which incorporates electron-donating benzodithiophene (**BDT**) units and electron-accepting naphthobisthiadiazole (**NTz**) units, forming a structure with 12 fused aromatic rings. To the best of our knowledge, fused π-conjugated structures containing **NTz** units have not been previously reported, despite their potential value. The photophysical and electrochemical properties of **BDT-NTz** were studied to assess the effects of the fused ring structure on these properties. OFETs based on **BDT-NTz** demonstrated hole transport characteristics. Furthermore, to investigate the potential of **BDT-NTz** as an electron-donating unit, the author developed a new copolymer based on both **BDT-NTz** and **FNTz**.

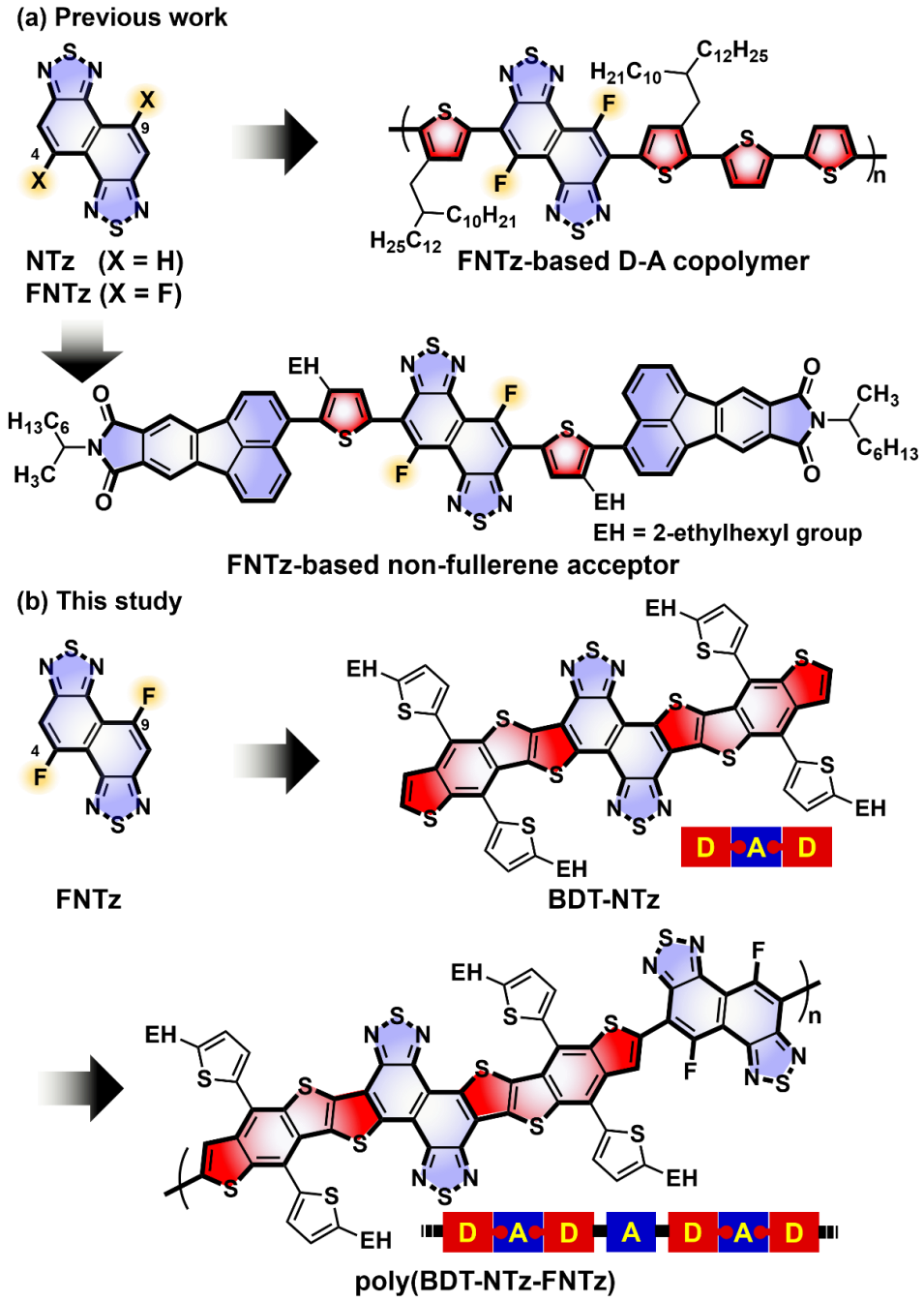

Figure 1-1. (a) Chemical structure of **FNTz** and organic semiconductors based on it. (b) Molecular design of a **NTz**-based DAD molecule and its copolymer.

1.2 Molecular design and synthesis

Scheme 1-1. Synthesis of **BDT-NTz**.

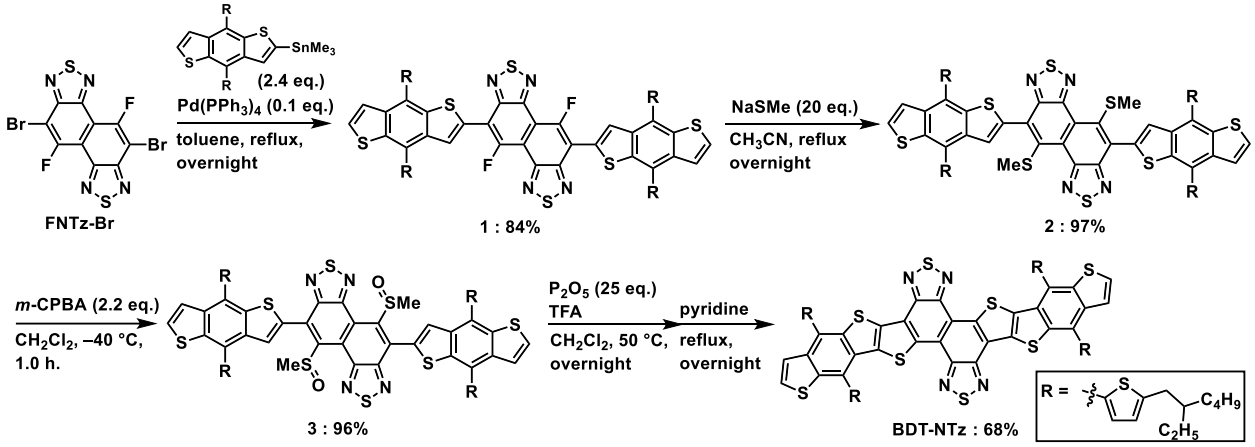

Electron-withdrawing aromatic molecules containing fluorine substituents undergo aromatic nucleophilic substitution (S_NAr) reactions with nucleophiles via the formation of Meisenheimer intermediates. For instance, 5,6-difluoro-2,1,3-benzothiadiazole reacts with sodium thiomethoxide (NaSMe) in an S_NAr reaction to yield the corresponding thiomethoxy-substituted compound.[27] Recently, Ie and coworkers demonstrated that S_NAr reactions between **FNTz** and KCN produced cyano-substituted **NTz** derivatives.[35, 36] Building on these precedents, our goal was to synthesize the thiomethoxy **NTz** unit and use it as a key component for creating fused π-conjugation through a sulfur atom linkage.

The synthetic route for **BDT-NTz** is shown in Scheme 1-1. To ensure solubility in common organic solvents, 2-(2-Ethylhexyl)thiophene groups were selected as solubilizing units. Migita-Kosugi-Stille cross-coupling between **FNTz-Br**[34] and stannylated benzodithiophene yielded compound **1** in 84% yield. Compound **1** was then converted to compound **2** in 97% yield through an S_NAr reaction with NaSMe. The thioether was subsequently oxidized using *m*-chloroperbenzoic acid (*m*-CPBA). The yield of **3** was highly dependent on the concentration of the reactants, as shown in Table S1-1. Finally, intramolecular double cyclization was achieved by reacting with excess trifluoroacetic acid in the presence of phosphorus pentoxide (P_2O_5), resulting in **BDT-NTz** with a yield of 71%. **BDT-NTz** was found to be soluble in common organic solvents, such as dichloromethane (CH_2Cl_2), chloroform ($CHCl_3$), toluene, and even hexane. The new compounds were unambiguously characterized by ^1H and ^{13}C NMR and high-resolution mass spectrometry (HR-MS).

Table S1-1. The effect of molar concentration in oxidation reactions.

Run	Concentration of **2** (M)	Yield of **3** (%)
1	9.3×10^{-3}	0
2	8.8×10^{-3}	53
3	1.3×10^{-3}	96

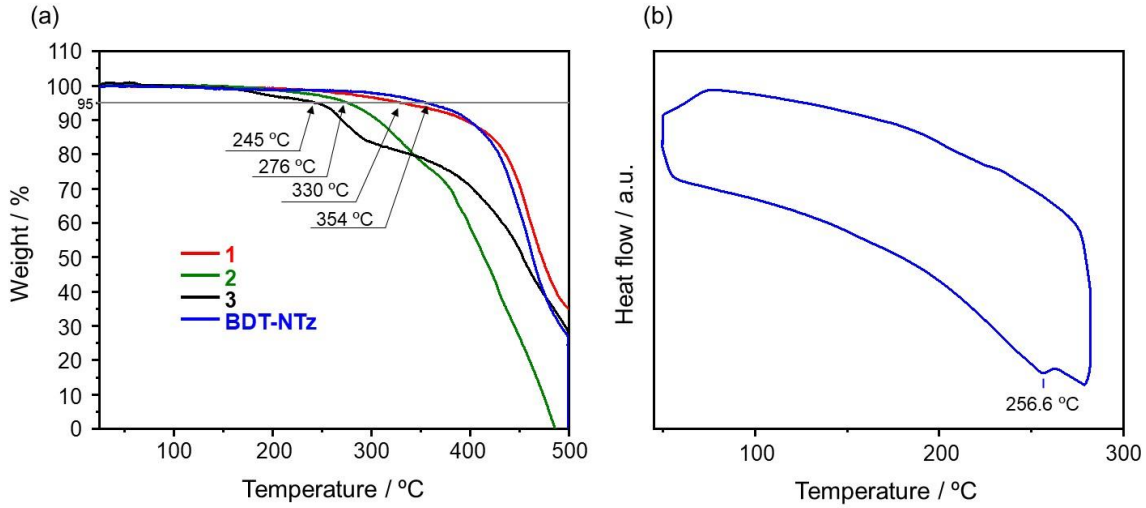

Figure S1-1. (a) TGA curves for **1** (red), **2** (green), **3** (black), and **BDT-NTz** (blue) and DSC curve of **BDT-NTz** for a heating rate of 10 °C min^{-1} in a N_2 atmosphere.

To assess the thermal properties of **BDT-NTz**, thermogravimetric analysis (TGA) and differential scanning calorimetry (DSC) measurements were performed under a nitrogen atmosphere (Fig. S1-1). The TGA curve revealed a 5% weight loss at 388 °C, indicating that **BDT-NTz** exhibits high thermal stability. The DSC curve displayed a single endothermic peak at 257 °C, corresponding to the melting point, suggesting that **BDT-NTz** is amorphous in the solid state, likely due to the presence of the bulky 2-ethylhexyl substituents.

1.3 Theoretical calculations

To optimize the structures and electronic states, density functional theory (DFT) calculations were performed at the B3LYP/6-31g(d,p) level. For these calculations, the 2-ethylhexyl groups in the original compounds were replaced with methyl groups to reduce computational cost (denoted as **1(Me)**, **2(Me)**, **3(Me)**, and **BDT-NTz(Me)**). As shown in Fig. 1-2a, **1(Me)** exhibited a nearly coplanar structure with a torsional angle of 1.2° between the **BDT** and **NTz** units, which the author attributes to intramolecular S-F interactions.[38-40] In contrast, the optimized structures of **2(Me)** and **3(Me)** showed larger torsional angles of 78.1° and 119.3°, respectively, due to significant steric repulsions between the **BDT** unit and the large sulfur atoms in the **NTz** unit. As expected, **BDT-NTz(Me)** adopted a completely planar geometry due to the fused thiophene ring structure.

Examining the Kohn-Sham molecular orbitals, the highest occupied molecular orbitals (HOMOs) of **1(Me)** and **BDT-NTz(Me)** were delocalized across the entire molecular backbone. In contrast, the HOMOs of **2(Me)** and **3(Me)** were localized on the electron-donating **BDT** units (Fig. 2b). This difference in HOMO distribution can be attributed to the degree of planarity deviation in these molecules. In contrast to the HOMOs, the lowest unoccupied molecular orbitals (LUMOs) for all molecules were localized in the electron-accepting **NTz** units.

To quantify the effect of the fused ring structure, the reorganization energies (λ^{+}) for the cationic states were estimated using the adiabatic potential energy surface method with the equation:

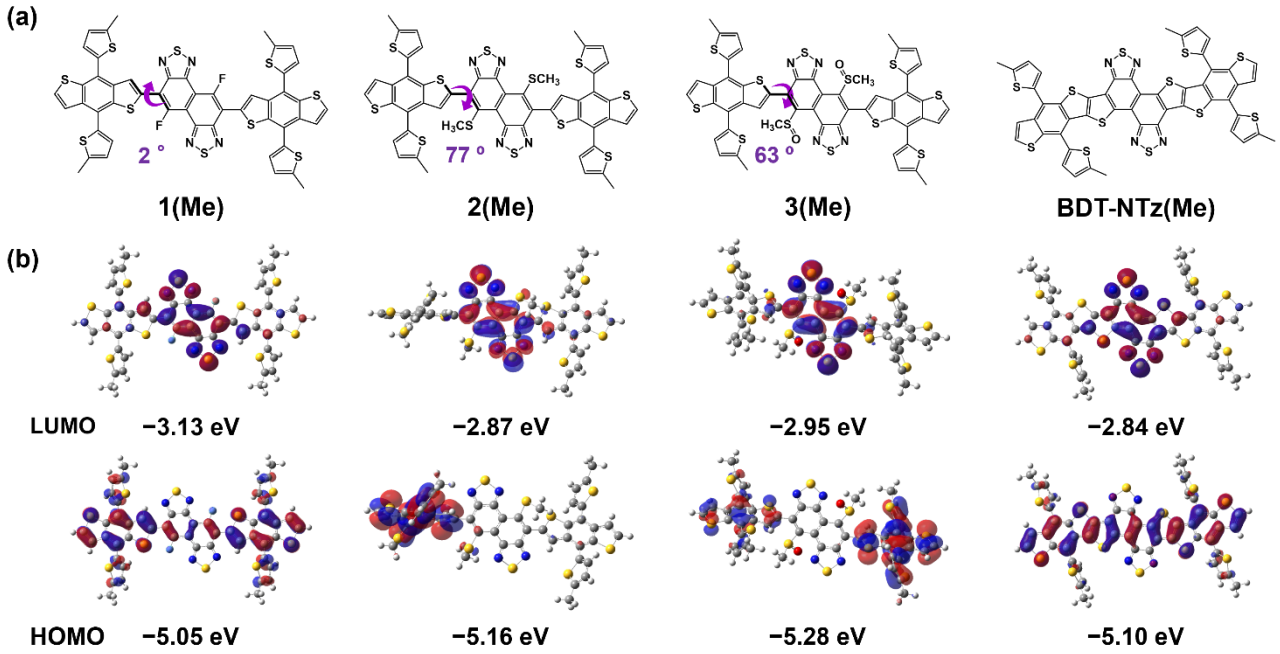

Figure 1-2. (a) Molecular structures and (b) Kohn-Sham molecular orbitals for **1(Me)**, **2(Me)**, **3(Me)**, and **BDT-NTz(Me)**. The structures were optimized at the B3LYP/6-31g(d,p) level.

$\lambda^{+} = (E_{+}^{*} - E_{+}) + (E^{*} - E)$

where E_{+}* is the energy of the cationic molecule in the neutral optimized geometry, E_{+} is the optimized energy of the cationic molecule, E* is the energy of the neutral molecule in the cationic optimized geometry, and E is the optimized energy of the neutral molecule. Energy calculations were performed at the B3LYP/6-31g(d,p) level for the optimized/transition structures of the ground and cationic states for derivatives **R(Me')** with methyl-substituted thiophene groups. The reorganization energy of **BDT-NTz(Me')** was calculated to be 166 meV, which was 54 meV lower than that of the non-fused molecule. Remarkably, this reorganization energy was close to that of rubrene (λ^{+} = 159 meV, calculated at the same level).[41] These results suggest that **BDT-NTz(Me')** could function as a π-extended donor unit with minimal structural fluctuations during hole transport.

1.4 Physicochemical properties

UV–vis absorption and fluorescence spectra were measured for $CHCl_3$ solutions of **BDT-NTz**, along with compounds **1**, **2**, and **3** (Fig. 1-3). The photophysical data are summarized in Table 1-1. As shown in Fig. 1-3(a), **BDT-NTz** exhibited an absorption band around 500–600 nm, corresponding to the π–π* transition, which was similar to that of **1**. **BDT-NTz** showed a relatively sharp absorption band with a higher extinction coefficient (ε) of 3.9×10^4 L mol^{-1} cm^{-1}, compared to **1** ($\varepsilon = 2.0 \times 10^4$ L mol^{-1} cm^{-1}). This was attributed to two factors: enhanced oscillator strength (f) and/or reduced thermodynamic perturbation.

To investigate the first factor, the f value was calculated using TD-DFT at the CAM-B3LYP/6-31g(d,p) level. The f value for **1(Me)** was 1.124, higher than that for **BDT-NTz(Me)** (f = 0.869), as shown in Table S1-2.

Table 1-1. Photophysical properties of **1**, **2**, **3**, and **BDT-NTz** in $CHCl_3$

Compounds	λ_{abs}/nm	ε/M^{-1} cm^{-1}	λ_{fl}/nm	Φ_f[a]	$<\tau_f>$/nsec	k_f[c]/$nsec^{-1}$	k_{nr}[c]/$nsec^{-1}$
1	564	2.0×10^4	694	0.05	1.63	0.031	0.58
2	470	1.6×10^4	677	0.01	0.53	0.019	1.9
3	535	3.0×10^3	631	<0.01	<0.10[b]	ND	ND
BDT-NTz	558	3.9×10^4	621	0.75	7.05	0.11	0.035

[a]Determined by the absolute method unless specifically stated. [b]Fluorescence decay was too fast to determine precisely with a streak scope. [c]Determined by the following equations: $\Phi_f = k_f/(k_f + k_{nr})$ and $<\tau_f> = 1/(k_f + k_{nr})$

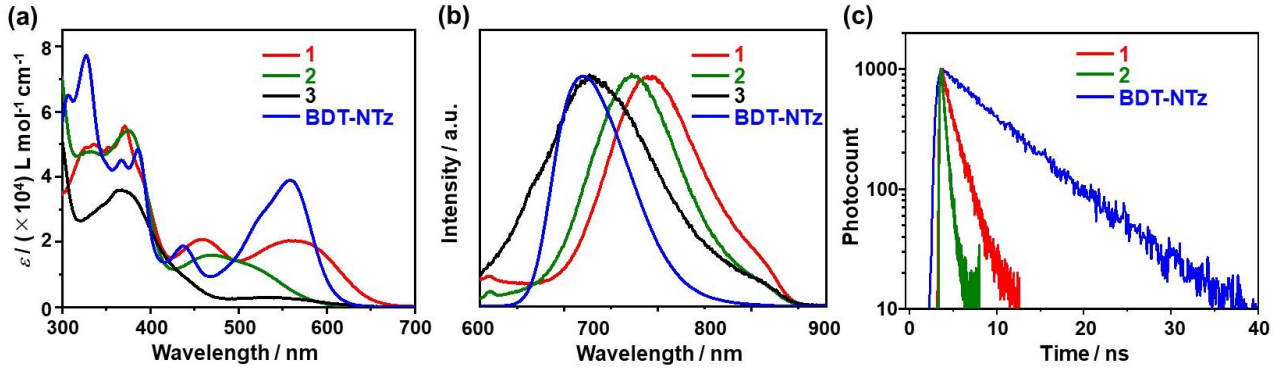

Figure 1-3. (a) UV–vis absorption spectra, (b) fluorescence spectra, and (c) fluorescence decay curves for **1** (red), **2** (green), **3** (black), and **BDT-NTz** (blue) in $CHCl_3$ solution.

To explore thermodynamic perturbation, torsional scan analyses were performed. As seen in Fig. S1-2, the energy distribution for **BDT-NTz(Me)** was largely confined to the planar structure, while **1(Me)** showed a broader distribution. These results suggest that the fused structure of **BDT-NTz** reduces thermodynamic perturbations, leading to a larger ε value. Compounds **2** and **3** displayed significant hypsochromic shifts of nearly 100 nm compared to **1**. The absorption spectrum of **BDT-NTz** in the film state is shown in Fig. S1-3.

Table S1-2. Photophysical properties of **1**, **2**, **3**, and **BDT-NTz** in $CHCl_3$.

Compounds	$\lambda_{calc,\ S1}$ / nm[a] (Oscillator strength *f*)	$\lambda_{abs,\ max}$ / nm (ε (10^4) / L mol^{-1} cm^{-1})	λ_{fl} / nm	Stokes Shift / cm^{-1}
1	531 (1.124)	564 (2.0)	694	3300
2	441 (0.544)	470 (1.6)	677	6500
3	407 (0.387)	535 (0.30)	631	2800
BDT-NTz	493 (0.869)	558 (3.9)	621	1800

[a]The maximum absorption wavelength $\lambda_{calc,\ S1}$ and its oscillator strength (*f*) is corresponding to S_0 to S_1 transition calculated from CAM-B3LYP/6-31g(d,p) level.

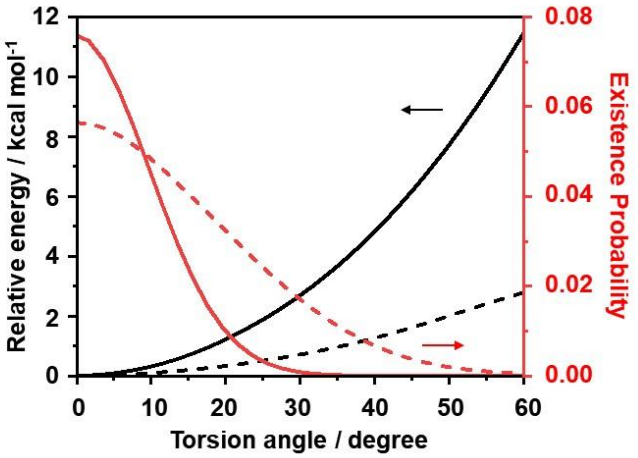

Figure S1-2. Torsional scan and population analysis of **1(Me)** (dashed line) and **BDT-NTz(Me)** (solid line) calculated from B3LYP/6-31g(d,p) level.

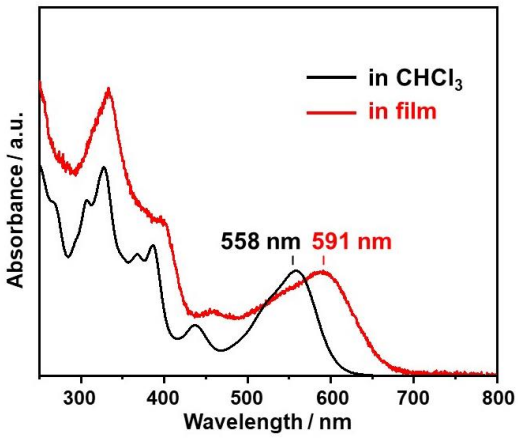

Figure S1-3. UV-vis absorption spectra of **BDT-NTz** in $CHCl_3$ solution (black line) and in the film state (red line).

The absorbance maximum (λ_{max} = 591 nm) in the film state was redshifted by 33 nm compared to the $CHCl_3$ solution, indicating that **BDT-NTz** molecules formed strong intermolecular interactions in the solid state.

As shown in Fig. 1-2(b), **BDT-NTz** exhibited a fluorescence emission with a maximum ($\lambda_{PL,max}$) at 621 nm, while $\lambda_{PL,max}$ for **1**, **2**, and **3** were 694, 677, and 631 nm, respectively. The Stokes shifts for **1**, **2**, **3**, and **BDT-NTz** were 3300, 6500, 2800, and 1800 cm^{-1}, respectively (Table S1-2). The relatively small Stokes shift of **BDT-NTz** suggests that structural relaxation in the excited state is suppressed for this molecule.

To gain further insights into the excited-state photophysical properties, photoluminescent quantum yields and time-resolved fluorescence spectra were measured for $CHCl_3$ solutions, with the results shown in Fig. 1-3c and Figs. S1-4-7. **BDT-NTz** exhibited a high quantum yield (Φ_f) of 0.75, while the Φ_f values for **1**, **2**, and **3** were 0.05, 0.01, and <0.01, respectively. The fluorescence decay lifetime ($<\tau_f>$) of **BDT-NTz** was 7.0 ns, significantly longer than those of the other derivatives (Fig. 1-3c, Table 1-1, and Table S1-3).

Table S1-3. Summary of photoexcited decay time

Compd.	τ_1	τ_2	$<\tau_f>^b$ / nsec
BDT-NTz	7.05 (100%)[a]	-	7.05
1	0.491 (13%)	1.80 (87%)	1.63
2	0.248 (63%)	1.01 (37%)	0.53
3	<0.1[c]	-	<0.1

[a]The area-weighted ratios ($A_n\tau_n$) are shown in parentheses. [b]The area-weighted mean fluorescence lifetime $<\tau_f>$ was estimated as following equation: $<\tau_f> = S(A_n\tau_n^2)/S(A_n\tau_n)$, where A_n is the coefficient of the exponential function for the n_{th} component. [c]The fluorescence decay was too fast to be determined.

Using these values and the equations provided below, the fluorescence rate constant (k_f) and nonradiative decay constant (k_{nr}) for **BDT-NTz** were calculated to be 0.11 and 0.035 ns^{-1}, respectively (Table 1-1):

$$\Phi_f = k_f/(k_f + k_{nr}) \quad (1)$$

$$<\tau_f> = (k_f + k_{nr})^{-1} \quad (2)$$

The k_{nr} value of **BDT-NTz** was the smallest among the molecules investigated, which indicated that suppression of thermal deactivation from the excited state due to the rigid structure of the highly fused backbone.

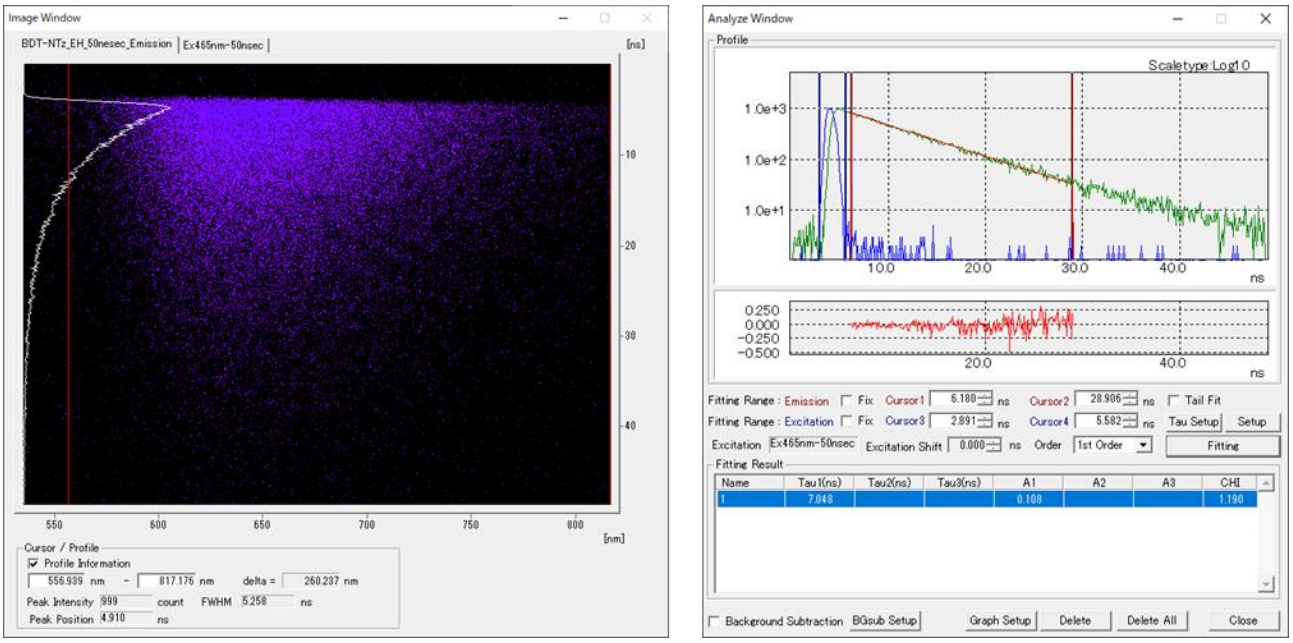

Figure S1-4. Streak image and (right) fluorescence decay analysis of **BDT-NTz** in a $CHCl_3$ solution.

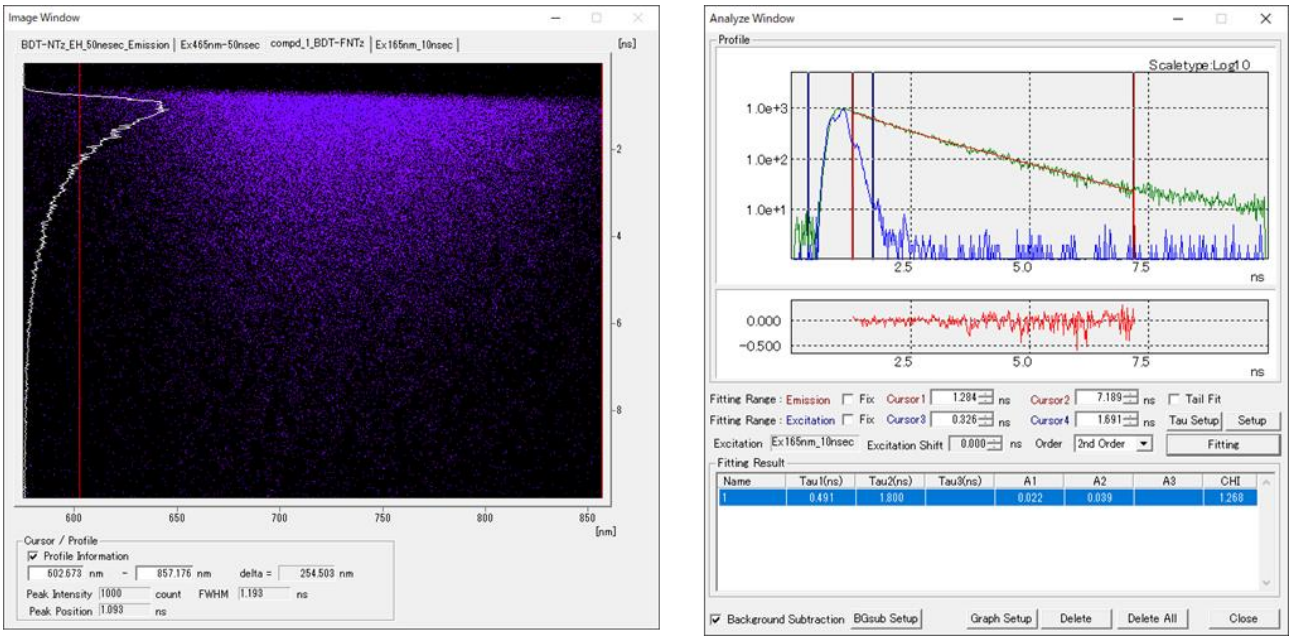

Figure S1-5. (left) Streak image and (right) fluorescence decay analysis of **1** in a $CHCl_3$ solution.

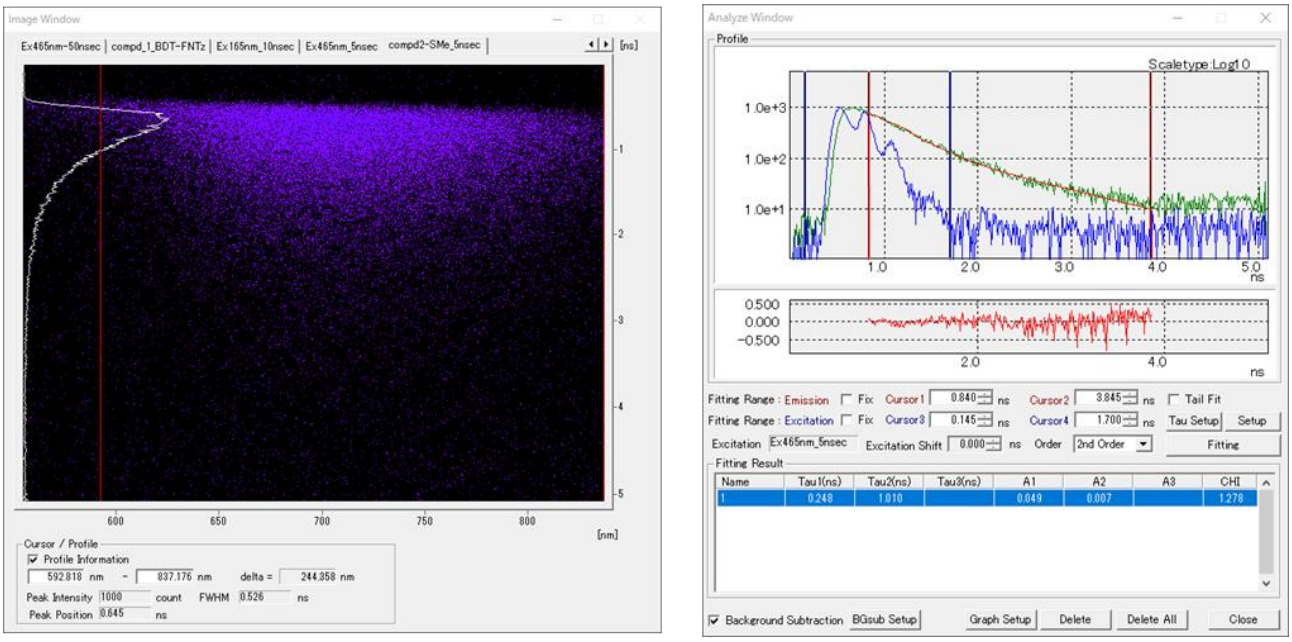

Figure S1-6. (left) Streak image and (right) fluorescence decay analysis of **2** in a $CHCl_3$ solution.

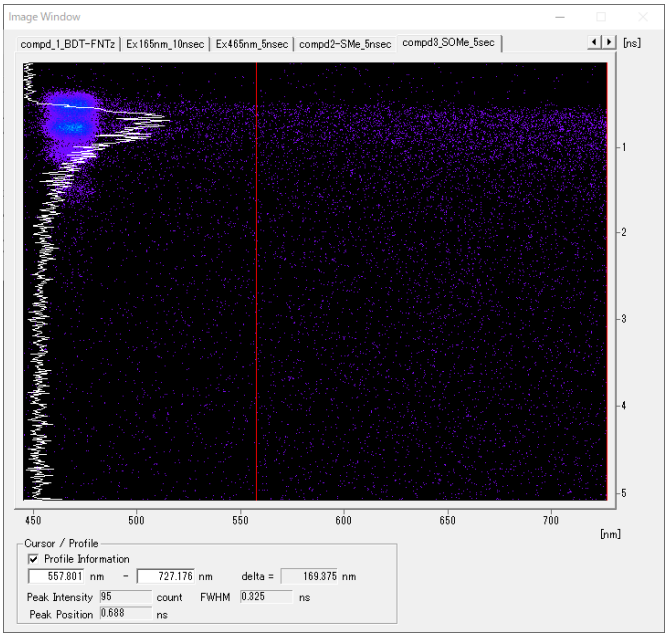

Figure S1-7. Streak image of **3** in a $CHCl_3$ solution.

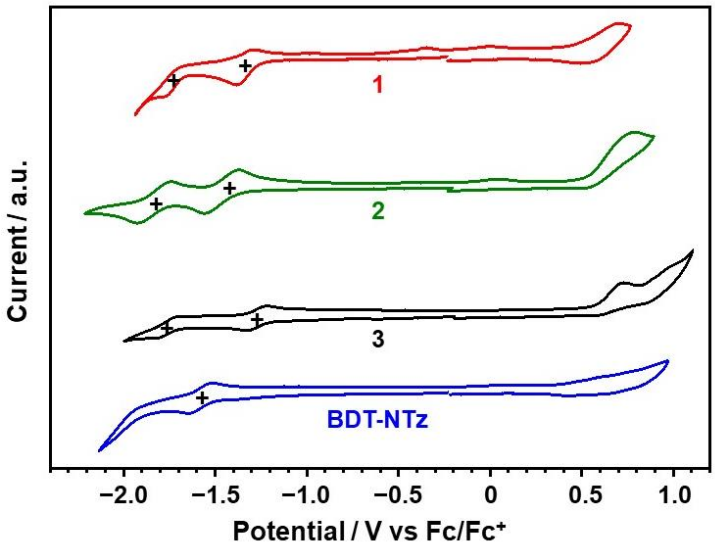

Figure 1-4. (a) Cyclic voltammograms for **1** (red), **2** (green), **3** (black), and **BDT-NTz** (blue) in CH_3CN/CH_2Cl_2 containing 0.1 M $TBAPF_6$.

To investigate the electrochemical properties, cyclic voltammetry (CV) and differential pulse voltammetry (DPV) measurements were performed in CH_2Cl_2/acetonitrile (CH_3CN) solutions containing 0.1 M tetrabutylammonium hexafluorophosphate ($TBAPF_6$). The redox potentials were referenced against ferrocene/ferrocenium (Fc/Fc^+), used as an internal standard. As shown in Fig. 1-4, **BDT-NTz** and derivatives **1-3** exhibited one and two reversible reduction waves during cathodic scans, respectively. The second reduction wave for **BDT-NTz** occurred outside the potential window of the solvent, indicating the formation of a stable radical anion. Two reduction waves were also observed in the DPV for all molecules (Fig. S1-8).

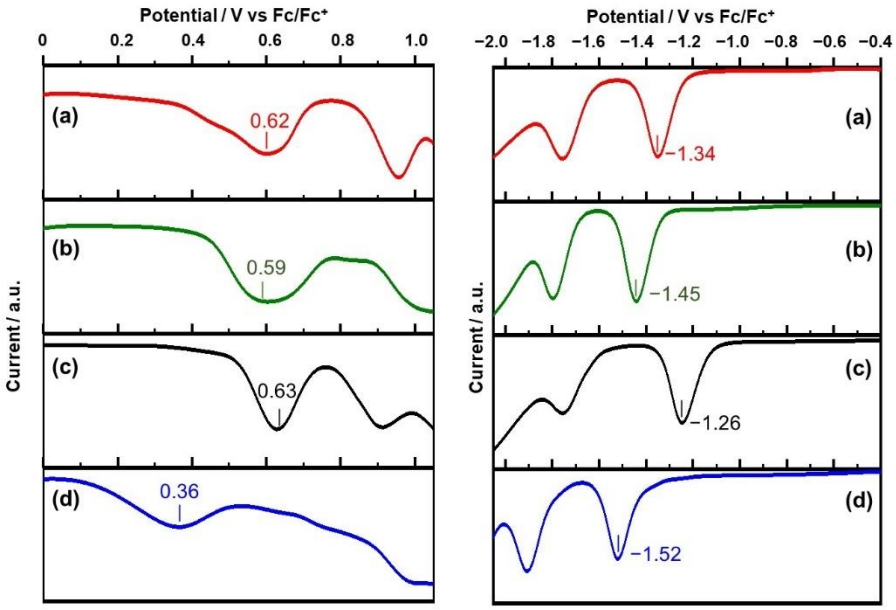

Figure S1-8. Differential pulse voltammograms of (a) **1**, (b) **2**, (c) **3**, and (d) **BDT-NTz**.

Table S1-4. Electrochemical properties of **1**, **2**, **3**, and **BDT-NTz**.

Compounds	E^{red} / V [a]	E^{ox} / V [a]	E_{LUMO} / eV [b]	E_{HOMO} / eV [c]	E_g / eV [d]
1	−1.34	0.62	−3.46	−5.42	1.96
2	−1.45	0.59	−3.35	−5.39	2.04
3	−1.26	0.63	−3.54	−5.43	1.89
BDT-NTz	−1.52	0.36	−3.28	−5.16	1.88

[a] In CH_3CN/CH_2Cl_2 containing 0.1 M $TBAPF_6$ V *vs*. Fc/Fc^+. [b] $E_{LUMO} = -E^{red} - 4.8$. [c] $E_{HOMO} = -E^{ox} - 4.8$. [d] $E_g = E_{LUMO} - E_{HOMO}$.

The first reduction peak (E^{red}) for **BDT-NTz** (−1.52 V) was observed at a more negative potential compared to **1** (−1.34 V), **2** (−1.45 V), and **3** (−1.26 V) (Fig. S1-8). In contrast, irreversible oxidation waves were seen for the other derivatives, with oxidation potentials determined by DPV analysis (Fig. S1-8).

The HOMO and LUMO energy levels for each molecule were estimated from the first oxidation and reduction peaks, respectively (Table S1-4). For **BDT-NTz**, the HOMO and LUMO energy levels were −5.16 and −3.28 eV, which are 0.23 and 0.07 eV higher than those of **2**, respectively. This suggests that the incorporation of sulfur atoms into the fused π-conjugated structure efficiently raised the HOMO/LUMO energy levels of **BDT-NTz**.

To gather information on the ionization potential (IP) and electron affinity (EA), photoelectron yield spectroscopy (PYS) and low-energy inverted photoemission spectroscopy (LEIPS) measurements were conducted for **BDT-NTz** in the film state (Fig. S1-9). The LEIPS spectrum was well reproduced by the density of states calculated for **BDT-NTz(Me)** (Fig. S1-9b). From the onset points of these spectra, the IP and EA values for **BDT-NTz** were found to be 5.39 and 3.52 eV, respectively. These energy levels indicate that **BDT-NTz** is suitable for use in OFET semiconducting materials when gold is used as the source and drain electrodes.

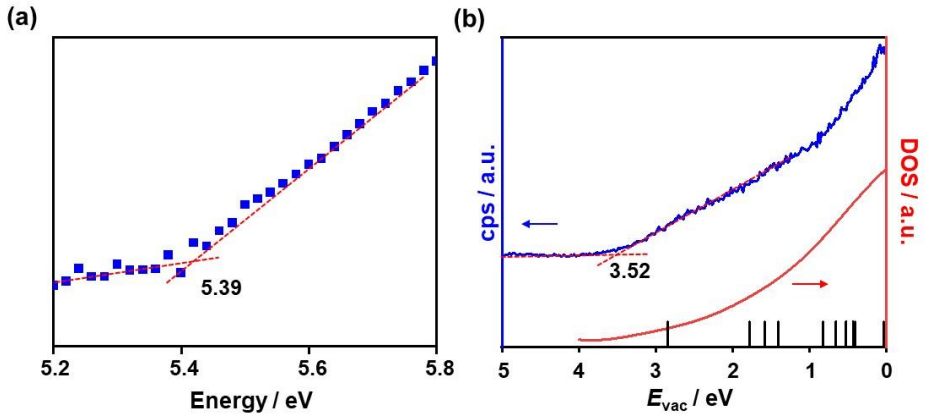

Figure S1-9. (a) PYS and (b) LEIPS spectra of **BDT-NTz** in the film state. DOS spectrum (red solid line) and LUMO energy levels (black solid line) were estimated by DFT calculation at B3LYP/6-31G(d,p) level.

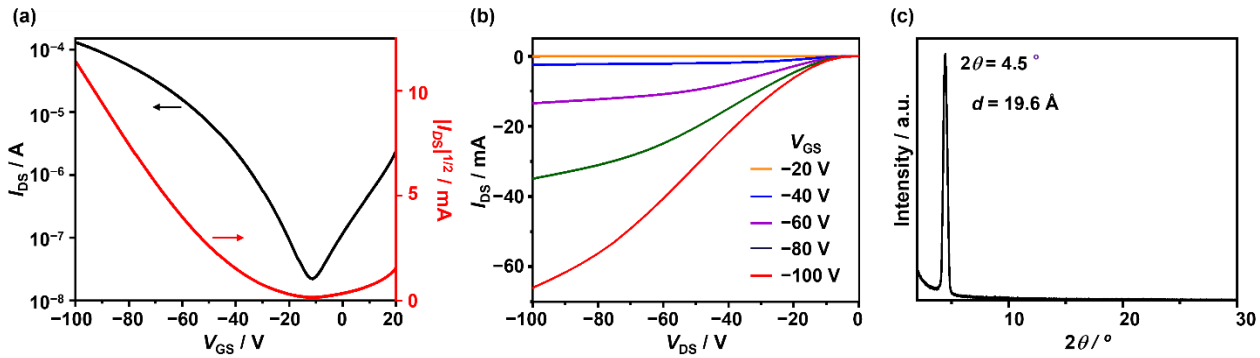

Figure 1-5. (a) Transfer and (b) output characteristics. (c) X-ray diffraction patterns for OFETs based on **BDT-NTz**.

Table S1-5. FET characteristics of **BDT-NTz**-based OFETs.

SAM[a]	T_{anneal} / °C[b]	V_{th} / V	I_{on} / I_{off}	μ_h / $cm^2\ V^{-1}\ s^{-1}$
None	100	14	10^4	1.7×10^{-4}
	150	−3.7	10^5	6.4×10^{-4}
	180	−43	10^4	1.1×10^{-3}
HMDS[c]	100	−21	10^4	3.2×10^{-4}
	150	−17	10^4	7.5×10^{-4}
	180	−22	10^3	9.2×10^{-4}
ODTS[d]	100	–	–	no FET
	150	–	–	no FET
	180	–	–	no FET

[a] SAM denotes self-assembled monolayer on the surface of Si/SiO_2 substrate. [b] T_{anneal} denotes substrate temperature during deposition. [c] HMDS denotes hexamethyldisilazane. [d] ODTS denotes octadecyltrichlorosilane.

1.5 Transistor characteristics

The semiconducting properties of **BDT-NTz** were evaluated using bottom-gate bottom-contact FET devices. The active layer was prepared by spin-coating from a $CHCl_3$ solution. As shown in Fig. 1-5 and Table S1-5, these devices exhibited typical p-type behavior under vacuum, with a hole mobility of 1.1×10^{-3} $cm^2\ V^{-1}\ s^{-1}$, a threshold voltage of −43 V, and an on/off current ratio of 10^4. No n-type characteristics were observed. The absence of electron-withdrawing end-capping groups in **BDT-NTz** is believed to hinder electron transfer from the Au electrode to the molecule. The output curve was nonlinear at low source-drain voltages, indicating contact resistance between the gold electrodes and the **BDT** molecules (Fig. 1-5b). Reducing this contact resistance is expected to improve the transistor performance.

To examine the crystallinity and surface morphology of the **BDT-NTz** film, X-ray diffraction (XRD) and atomic force microscopy (AFM) measurements were conducted. As shown in Fig. 1-5c, the out-of-plane XRD pattern revealed a peak at $2\theta = 4.5°$, corresponding to lamellar packing with a *d*-spacing of 19.6 Å.

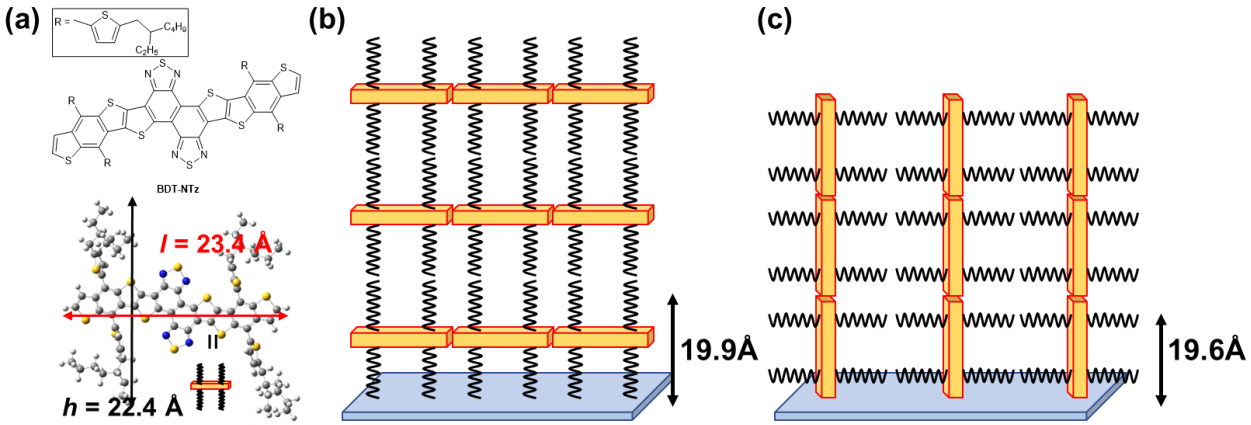

Figure S1-10. (a) The optimized structure of **BDT-NTz** and (b,c) the plausible packing structures of **BDT-NTz** in the film states on the Si substrate. The monomer structure was optimized by DFT calculation at PM6 level.

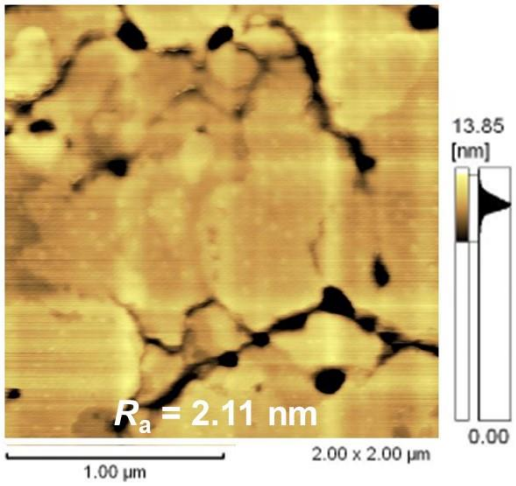

Figure S1-11. AFM image of **BDT-NTz** film. R_a denotes average surface roughness of **BDT-NTz** film.

This value matches the edge-to-edge molecular length between the α-positions of the terminal thiophenes or the terminal carbons in the alkyl chains of **BDT-NTz**. The film structure showed that the molecules were arranged in a lamellar packing, with the alkyl chains or π-conjugated backbones aligned perpendicular to the SiO_2/Si substrates (Fig. S1-10). AFM images of the **BDT-NTz** film displayed sheet-like grains and a relatively smooth surface (Fig. S1-11), suggesting that the lamellar packing structure facilitated charge transport through π-π interactions between the electrodes.

1.6 Synthesis of copolymer

For potential use as a donor unit in D-A type π-conjugated polymers, functional groups such as bromine or trimethylstannyl groups were introduced at the terminal α-positions of **BDT-NTz**. Bromination with Br_2 resulted in a mixture of mono-, di-, and tri-brominated products (Scheme S1-1), likely due to regioselectivity issues.

Scheme S1-1. Functionalization reactions of **BDT-NTz**.

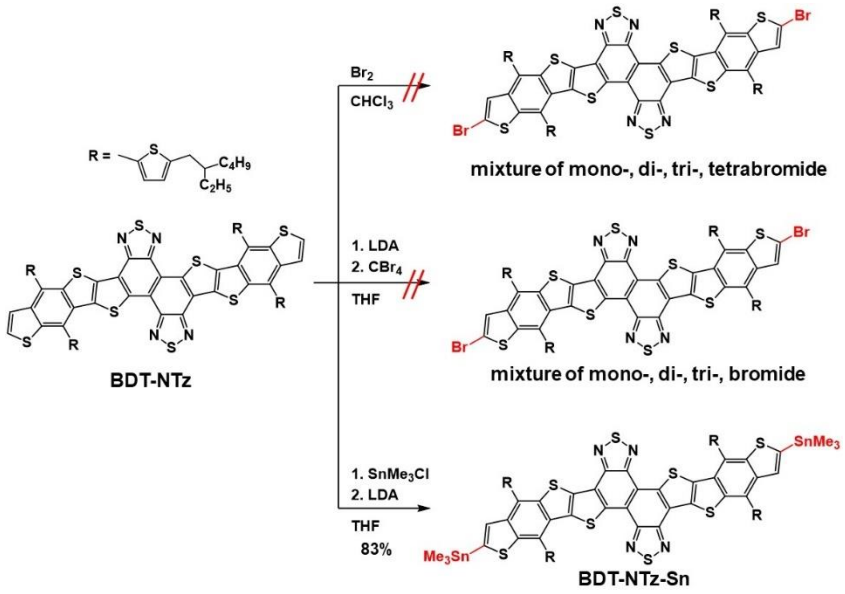

Scheme 1-2. Synthetic route for the preparation of **poly(BDT-NTz-FNTz)*n***

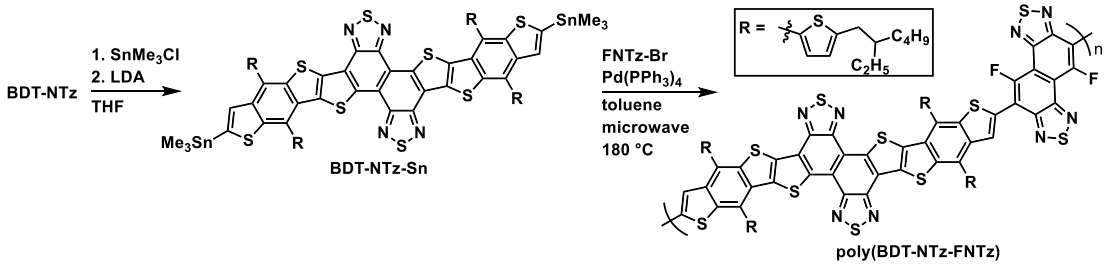

To control bromination, the dianion of **BDT-NTz** was reacted with tetrabromomethane (CBr_4), but this resulted in a mixture of α- and β-brominated compounds. Trimethylstannyl groups were successfully introduced by reacting the dianion with trimethylstannyl chloride, yielding **BDT-NTz-Sn** in 83% yield (Scheme 1-2). The *in situ* anion-trapping condition was crucial for stabilizing the **BDT-NTz** anions. A subsequent Stille coupling with **FNTz-Br** in the presence of $Pd(PPh_3)_4$ under microwave conditions produced the target copolymer **poly(BDT-NTz-FNTz)**, which was isolated via Soxhlet extraction using $CHCl_3$.

Poly(BDT-NTz-FNTz) showed relatively low solubility (1.0 mg/mL) in common solvents like $CHCl_3$. Gel permeation chromatography (GPC) analysis revealed a number average molecular weight (M_n) of 5.01 kDa and a polydispersity index (PDI) of 1.27 (Fig. S1-12). The relatively low M_n was attributed to the low solubility of the polymer during the Stille coupling reaction.

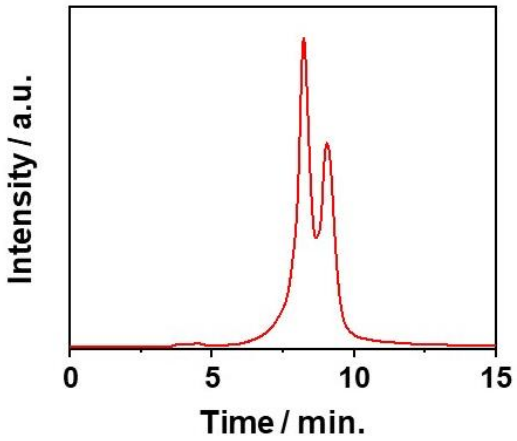

Figure S1-12. GPC chart of **poly(BDT-NTz-FNTz)**.

1.7 Properties and semiconducting characteristics of the copolymer

The UV-vis absorption spectrum of **poly(BDT-NTz-FNTz)** in $CHCl_3$ showed a sharp absorption band at 650 nm, indicating a highly planar structure with minimal structural variation in solution. In the film state, the absorption maximum shifted to 629 nm, redshifted by 21 nm compared to the solution, indicating strong intermolecular interactions in the film state.

To determine the ionization potential (IP) and electron affinity (EA) for **poly(BDT-NTz-FNTz)** in the solid state, photoelectron yield spectroscopy (PYS) and low-energy inverted photoemission spectroscopy (LEIPS) measurements were performed (Fig. S1-13). From the onset energies, the IP and EA values were determined to be 5.17 and 3.75 eV, respectively. FET devices fabricated with **poly(BDT-NTz-FNTz)** by spin-coating a $CHCl_3$ solution onto an octadecyltrichlorosilane (ODTS)-modified silicon substrate exhibited p-type behavior with a hole mobility of 2.7×10^{-4} cm^2 V^{-1} cm^{-1}, a V_{th} of −20 V, and a current on/off ratio of 10^4 (Fig. 1-7). AFM images of the film surface showed a relatively smooth surface (Fig. S1-14).

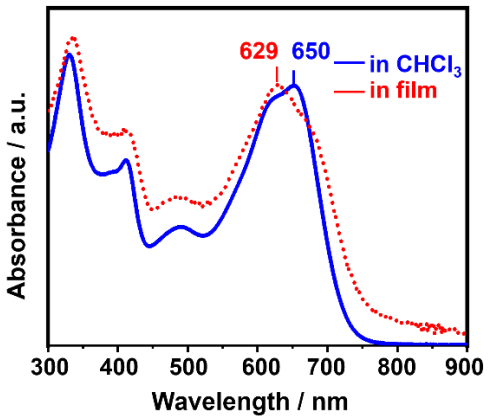

Figure 1-6. UV–vis absorption spectra for **poly(BDT-NTz-FNTz)** in $CHCl_3$ solution (blue solid line) and as a film (red dotted line).

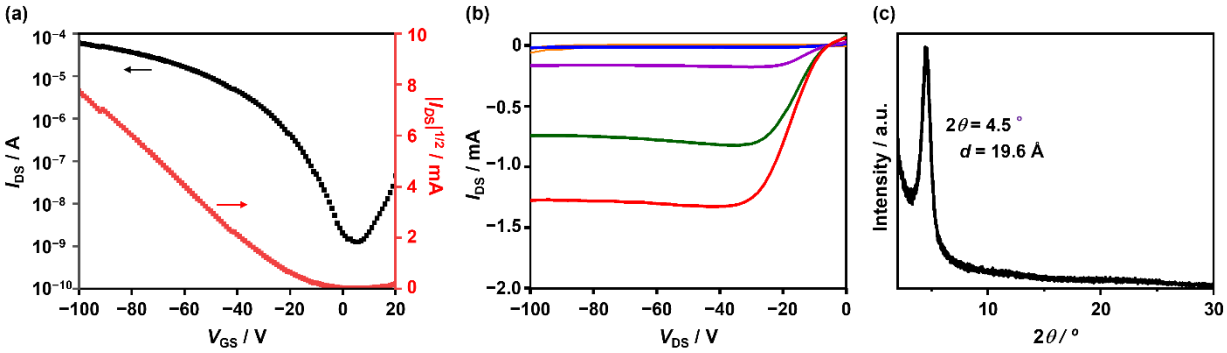

Figure 1-7. (a) Transfer, (b) output characteristics, and (c) XRD data for the **poly(BDT-NTz-FNTz)** film.

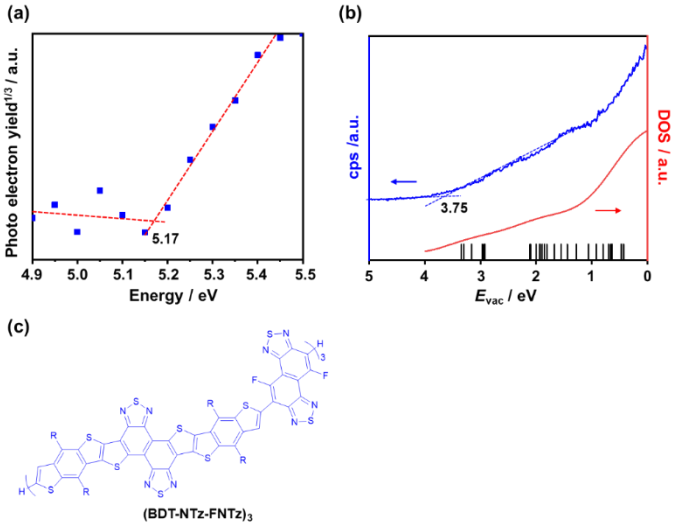

Figure S1-13. (a) PYS and (b) LEIPS spectra of **poly(BDT-NTz-FNTz)** film. (c) The trimer structure **(BDT-NTz-FNTz)$_3$**. DOS spectrum (red solid line) and LUMO energy levels (black solid line) for **(BDT-NTz-FNTz)$_3$** were estimated by DFT calculation B3LYP/6-31G(d,p) level.

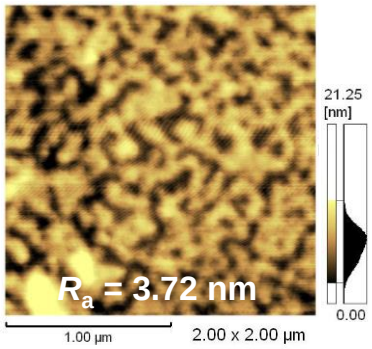

Figure S1-14. AFM image of **poly(BDT-NTz-FNTz)** film. R_a denotes average surface roughness of **poly(BDT-NTz-FNTz)** film.

XRD measurements revealed a sharp diffraction peak at $2\theta = 4.4°$ in the out-of-plane direction, corresponding to a *d*-spacing of 19.6 Å (Fig. 1-7c). The π-conjugated backbone in the polymer structure is longer than in **BDT-NTz** (l = 23.4 Å), while the end-to-end lengths of the alkyl chains (h = 22.4 Å) change only slightly after polymerization. This resulted in a lamellar packing structure, with the alkyl chains oriented perpendicular to the Si substrate and the π-π stacking structure parallel to the substrate. The author concludes that this arrangement facilitates charge transport.

1.8 Conclusion

In summary, the author reports the development of the fused DAD type π-extended molecule **BDT-NTz**, synthesized via an S_NAr reaction involving fluorine atoms in **NTz** and thiomethyl groups, followed by cyclization. TGA measurements indicated that **BDT-NTz** exhibits high thermal stability in the solid state. The absorption and fluorescence spectra show a sharp absorption band and bright red emission, with a high quantum yield of 75% in $CHCl_3$ solution. In FET devices, **BDT-NTz** exhibited hole transport with a mobility of 1.1×10^{-3} $cm^2\ V^{-1}\ s^{-1}$. A copolymer, **poly(BDT-NTz-FNTz)**, was also synthesized, and its properties and semiconducting behavior were studied. These findings demonstrate that fused π-extended DAD systems can be synthesized using **FNTz**, which opens the door to the development of a series of organic semiconducting materials. The author is currently working on the synthesis of electron-transporting materials and nanometer-scale π-conjugated systems with high hopping-transport properties based on **BDT-NTz**.

1.9 Experimental Section

General Information

Column chromatography was performed on silica gel (KANTO Chemical (Tokyo, Japan) silica gel 60N with 40–50 μm mesh for normal phase). Microwave irradiation was performed using a Biotage Initiator+ 4.2.1. The microwave power output was set at 400 W, and the internal temperature during the reaction was monitored by an IR sensor. ^{1}H and ^{13}C NMR spectra of $CDCl_3$ or CD_2Cl_2 solutions were recorded on a JEOL JNM-ECS400 spectrometer with tetramethylsilane (TMS) or dichloromethane as internal standards. Data are reported as follows: chemical shift in ppm (δ), multiplicity (s = singlet, d = doublet, t = triplet, q = quartet, m = multiplet), coupling constant (Hz), and integration. High-resolution mass spectra (HRMS) were obtained by atmospheric pressure chemical ionization (APCI) or electrospray ionization (ESI) methods using a Thermo Scientific LTQ Orbitrap XL. Elemental analyses were performed on a Perkin Elmer LS-50B instrument at the Elemental Analysis Section of the Comprehensive Analysis Center (CAC), SANKEN, Osaka University. Preparative GPC was performed on a JAPAN Analytical Industry LC-918 equipped with JAI-GEL 1H/2H. All chemicals and reagents were purchased from commercial sources (FUJIFILM Wako Chemicals (Tokyo, Japan), TCI (Tokyo, Japan) and Sigma Aldrich (MO, USA). **FNTz-Br** and **BDT_EH-Sn** were synthesized according to the literature procedures.[34, 37] It should be noted that several ^{13}C NMR peaks overlapped due to the molecular symmetries of the materials.

Measurement of photophysical properties

UV-vis spectra were recorded on a Shimadzu UV-3600 spectrophotometer. Fluorescence spectra were recorded using a Fluoromax-2 spectrometer in the photon-counting mode equipped with a Hamamatsu R928 photomultiplier. All spectra were obtained in spectrograde solvents. Fluorescence quantum yields in solution were determined by a Hamamatsu Photonics Absolute quantum yield measurement system C6620-02G. Fluorescence lifetimes were recorded on a Hamamatsu Photonics picosecond fluorescence lifetime measurement system C11200 equipped with a picosecond light pulser PLP-10, spectrograph C11119−01, and streak scope C10627. Excitation was carried out by a laser diode, where the wavelength was λ = 465 nm (pulse width around 57 ps).

Measurement of Electrochemical Properties

Cyclic voltammetry (CV) was carried out on a BAS CV-620C voltammetric analyzer using a platinum disk as the working electrode, platinum wire as the counter electrode, and $Ag/AgNO_3$ as the reference electrode at a scan rate of 100 mV s^{-1}. CV measurement was conducted in CH_2Cl_2/CH_3CN (10/1) solutions containing 0.1 M Tetrabutylammonium hexafluorophosphate ($TBAPF_6$).

Evaluation of thin film properties

The surface structures of the deposited organic film were observed by atomic force microscopy (Shimadzu, SPM9600), and the film crystallinity was evaluated by X-ray diffractometer measurements (Rigaku, SmartLab). X-ray diffraction patterns were obtained using Bragg-Brentano geometry with Cu$K\alpha$ radiation as an X-ray source with

an acceleration voltage of 45 kV and a beam current of 200 mA. The scanning mode was set to $2\theta\chi/\phi$ scans between 2º–30º with scanning steps of 0.1º, and the incidence angle was fixed at 0.20°.

Evaluation of polymers

Analytical GPC was performed on a Hitachi High-Technologies Corporation L-2401/L-2130 equipped with a Shodex K-803L at 40 ºC using chloroform ($CHCl_3$) as an eluent.

Photo-electron yield spectroscopy (PYS)

Photo-electron yield spectroscopy (PYS) was performed using Bunko Keiki BIP-KV202GD instrument or Bunko Keiki BIP-KV2016K instrument. The sample was prepared onto glass substrate by spin-coating method.

Low-energy inverse photoemission spectroscopy (LEIPS)

Low-energy inverse photoemission spectroscopy (LEIPS) on indium-tin-oxide (ITO) glass was performed using Ulvac-Phi, Inc. LEIPS system (734170). The film of the monomer or polymer for the LEIPS measurement was fabricated onto ITO substrates by the spin-coating of the 1 mg/mL $CHCl_3$ solution.

OFET device fabrication and evaluation

The field-effect electron mobility was measured using bottom-gate bottom-contact OFET devices. The p-doped silicon substrate functions as the gate electrode. A thermally grown silicon oxide (SiO_2) dielectric layer on the gate substrate has 300 nm thick and a capacitance of 10.0 nF cm^{-2}. Interdigital source and drain electrodes were constructed with gold (30 nm) that were formed on the SiO2 layer. The channel width (W) and channel length (L) are 38 mm and 5 μm, respectively. The silicon oxide surface was first washed with toluene, acetone and 2-propanol. It was then activated by ozone treatment and pretreated with ODTS. The semiconducting layer was fabricated by spin coating from 1.0 wt% $CHCl_3$ solution at 1000 rpm for 1 min or drop-cast method onto the substrate in air, followed by annealing for 60 min at various temperatures under a vacuum condition (10^{-3} Pa). The characteristics of the OFETs were measured at room temperature under a pressure of 10^{-3} Pa by using a KEITHLEY 4200 semiconductor parameter analyzer. The μ_h was calculated in the saturated region at the V_{DS} of 100 V by the following equation:

$$I_{DS} = \frac{W}{2L} C_i \mu (V_{GS} - V_{th})^2$$

Current on/off ratio was determined from the I_D sat V_{GS}= 0 V (I_{off}) and V_{GS}= 100 V (I_{on}).

Synthesis and characterization

*Synthesis of **1***: **FNTz-Br**[48] (191 mg, 0.436 mmol), **BDT_EH-Sn**[37] (770 mg, 1.038 mmol), and $Pd(PPh_3)_4$ (103 mg, 0.090 mmol) were placed in a test tube with a screw cap and dissolved in toluene (7 mL). After the reaction mixture was refluxed overnight, the resulting mixture was concentrated under reduced pressure, and then the residue was purified by column chromatography on silica gel (hexane:$CHCl_3$ = 2:1) to give **1** as a dark red solid (531 mg, 0.370 mmol, 84%). ^{1}H NMR (400 MHz, $CDCl_3$, TMS, δ): 0.90-1.02 (m, 24H), 1.35-1.54 (m, 32H), 1.69-1.79 (m, 4H), 2.90 (d, J = 6.8 Hz, 4H), 2.94 (d, J = 6.8 Hz, 4H), 6.93 (d, J = 3.2 Hz, 2H), 6.98 (d, J = 3.2 Hz, 2H), 7.35 (m, 4H), 7.42 (d, J = 3.2 Hz, 2H), 7.60 (d, J = 5.6 Hz, 2H), 9.06 (s, 2H); ^{13}C NMR (100 MHz, $CDCl_3$, δ): 146.9, 145.9, 145.8, 138.8, 137.3, 137.2, 136.9, 135.5, 132.5, 128.8, 128.4, 128.3, 128.1, 125.7, 125.5, 124.9, 123.6, 123.1, 41.5, 41.4, 34.3, 32.9, 32.6, 29.1, 25.6, 23.4, 23.3, 14.5, 14.5, 11.2, 10.9; HRMS (APCI) m/z: $[M+H]^+$ calcd. for $C_{78}H_{82}F_2N_4S_{10}$, 1433.3787; found, 1433.3800.

*Synthesis of **2***: Compound **1** (150 mg, 0.105 mmol) and $NaSCH_3$ (168 mg, 2.40 mmol) were placed in a test tube with a screw cap and dissolved in CH_3CN (20 mL). After stirring, the reaction was refluxed overnight, and the resulting mixture was washed with water. The combined organic layer was concentrated under reduced pressure, and then the resulting solid was washed with MeOH to give **2** as a dark red solid (145 mg, 0.097 mmol, 97%). 1H NMR (400 MHz, $CDCl_3$, TMS, δ): 0.86-0.93 (m, 24H), 1.31-1.42 (m, 32H), 1.66-1.69 (m, 4H), 2.33 (S, 6H), 2.85 (d, J = 6.4 Hz, 8H), 6.88 (t, J = 5.6 Hz, 4H), 7.39 (m, 4H), 7.52 (d, J = 5.2 Hz, 2H), 7.72 (d, J = 6 Hz, 2H), 8.18 (s, 2H); 13C NMR (100 MHz, $CDCl_3$, δ): 154.8, 151.2, 146.0, 146.0, 141.0, 140.1, 139.2, 138.5, 137.2, 136.2, 130.9, 128.1, 128.0, 127.4, 125.6, 125.5, 125.0, 124.0, 123.8, 41.5, 41.5, 34.4, 32.6, 29.0, 25.8, 23.1, 21.8, 14.3, 14.3, 11.0; HRMS (APCI) m/z: [M+H]+ calcd. for $C_{80}H_{88}N_4S_{12}$, 1489.3730; found, 1489.3730.

*Synthesis of **3***: Compound **2** (167 mg, 0.112 mmol) was placed in a round-bottomed flask and dissolved in CH_2Cl_2 (60 mL). A solution of *m*CPBA (42.5 mg, 0.246 mmol) in CH_2Cl_2 (32 mL) was added at −40 °C. After the reaction mixture was stirred at −40 °C for 1 h, the reaction was quenched by addition of a $NaHCO_3$ aq. solution. The resulting mixture was extracted with $CHCl_3$, and the organic layer was washed with water. The residue was purified by column chromatography on silica gel (hexane:$CHCl_3$ = 1:1) to give **3** as a dark red solid (163 mg, 0.107 mmol, 96%). ^{1}H NMR (400 MHz, $CDCl_3$, TMS, δ): 0.88-0.91 (m, 24H), 1.29-1.37 (m, 32H), 1.60-1.66 (m, 4H), 2.81 (t, J = 8.0 Hz, 8H), 3.63 (d, J = 4.0 Hz, 6H), 6.85 (m, 4H), 7.36 (d, J = 3.6 Hz, 2H), 7.39 (t, J = 3.2 Hz, 2H), 7.51 (d, J = 5.2 Hz, 2H), 7.72 (d, 6.0 Hz, 2H), 7.86 (d, 5.2 Hz, 2H); ^{13}C NMR (100 MHz, $CDCl_3$, δ): 155.4, 150.5, 145.9, 145.8, 139.5, 137.2, 137.1, 136.1, 131.5, 131.4, 128.1, 128.0, 128.0, 127.0, 125.5, 124.6, 124.4, 124.0, 123.7, 44.2, 44.0, 41.5, 41.5, 34.3, 34.3, 32.5, 29.0, 25.8, 23.1, 23.1, 14.3, 14.2, 11.0; HRMS (APCI) m/z: $[M+H]^+$ calcd. for $C_{80}H_{88}N_4O_2S_{12}$, 1521.3629; found, 1521.3625.

*Synthesis of **BDT-NTz***: A solution of Compound **3** (96 mg, 0.063 mmol) in CH_2Cl_2 (1.5 mL), P_2O_5 (150 mg, 1.06 mmol), and TFA (20 mL) was placed in a round-bottomed flask. After the reaction mixture was stirred at 50 °C overnight, the reaction was quenched by addition of ice water. The resulting mixture was extracted with $CHCl_3$, and the organic layer was washed with water. The resulting solid was placed in a test tube with a screw cap and dissolved

in pyridine (20 mL). After the reaction mixture was refluxed overnight, the resulting mixture was evaporated. The residue was purified by column chromatography on silica gel (hexane:CH_2Cl_2 = 4:1), and the resulting solid was washed with MeOH to give **BDT-NTz** as a dark red solid (62 mg, 0.043 mmol, 68%). mp 256.2-257 °C, ^{1}H NMR (400 MHz, $CDCl_3$, TMS, δ): 0.94-0.97 (m, 20H), 1.16 (s, 4H), 1.36-1.42 (m, 22H), 1.53-1.57 (m, 8H), 1.63-1.64 (m, 4H), 2.02 (m, 2H), 2.73 (d, J = 6.4 Hz, 4H), 3.14 (d, J = 7.6 Hz, 4H), 6.52 (d, J = 35.2 Hz, 4H), 7.29 (s, 2H), 7.42 (d, J = 4.0 Hz, 2H), 7.54 (d, J = 4.8 Hz, 2H), 7.73 (s, 2H); ^{13}C NMR (100 MHz, $CDCl_3$, δ): 149.6, 148.5, 146.6, 145.6, 141.9, 141.1, 139.3, 138.0, 136.6, 135.8, 135.2, 134.1, 130.5, 128.0, 127.5, 125.9, 125.5, 125.2, 124.0, 123.2, 121.6, 118.3, 41.5, 41.3, 34.3, 32.9, 29.1, 25.6, 23.4, 23.3, 14.5, 14.5, 11.2, 10.9; HRMS (APCI) m/z: $[M+H]^+$ calcd. for $C_{78}H_{80}N_4S_{12}$, 1457.3110; found, 1457.3129., Anal. Calcd. for $C_{78}H_{80}N_4S_{12:}$ C 64.25, H 5.53, N 3.84; found: C 64.14, H 5.72, N 3.66.

*Synthesis of **BDT-NTz-Sn***: **BDT-NTz** (24 mg, 0.016 mmol) was dissolved in 5 ml of anhydrous THF and cooled to -78 °C in a MeOH/dry ice bath under nitrogen protection. A 1.0 M Me_3SnCl/hexane solution (0.80 mL, 0.80 mmol) was added dropwise with stirring. Then, 1.0 M LDA/hexane solution (0.80 mL, 0.80 mmol) was added dropwise with stirring. The mixture was kept in a dry ice bath for 1 h and then stirred at room temperature for 16 h, quenched with 10 mL of water, and extracted with $CHCl_3$. The organic extract was dried with anhydrous sodium sulfate and evaporated in vacuo. Column chromatography was performed on alumina gel (hexane:$CHCl_3$ = 1:5) and GPC. A dark red solid of **BDT-NTz-Sn** (15 mg, 0.0084 mmol, 51%) was obtained. ^{1}H NMR (400 MHz, CD_2Cl_2, δ): 0.45 (s, 18H), 0.95 (t, J = 14.8 Hz. 20H), 1.18 (m, 5H), 1.26 (s, 1H), 1.37-1.45 (m, 22H), 1.65 (m, 6H), 1.72-1.75 (m, 4H), 1.98 (m, 2H), 2.73 (d, J = 6.0 Hz, 4H), 3.17 (m, 4H), 7.34 (s, 4H), 7.63 (t, J = 28.8 Hz, 2H), 7.72-7.82 (m, 2H), ^{13}C NMR (100 MHz, $CDCl_3$, δ): 176.2, 150.0, 149.0, 145.7, 143.1, 142.1, 140.1, 138.3, 138.2, 136.2, 136.5, 134.6, 131.4, 130.1, 128.1, 126.3, 125.4, 124.9, 122.7, 122.2, 115.0, 41.5, 34.4, 34.1, 32.8, 32.6, 29.3, 29.1, 25.7, 23.2, 14.4, 11.1, 11.0, 0.08, -8.1; HRMS (ESI) m/z: $[M-H]^-$ calcd. for $C_{84}H_{95}N_4S_{12}Sn_2$, 1783.2327; found, 1783.2333.

*Synthesis of **poly(BDT-NTz-FNTz)***: **BDT-NTz-Sn** (13 mg, 0.0073 mmol), **FNTz-Br** (3.2 mg, 0.0073 mmol), $Pd(PPh_3)_4$ (0.9 mg, 0.00078 mmol), and 0.6 mL of toluene were added to a 2 mL reaction vessel. The vessel was purged with N_2 gas and sealed. The vessel was put into a microwave reactor and heated at 180 °C for 20 min. After cooling to room temperature, the reaction mixture was poured into methanol (5 mL). The precipitate was filtered and subjected to sequential Soxhlet extractions with methanol, hexane, and dichloromethane to remove low-molecular-weight fractions. The residue was extracted with $CHCl_3$, which was then reprecipitated in methanol. The precipitate was filtered and dried in vacuo to obtain **poly(BDT-NTz-FNTz)** as a dark blue solid (9 mg, 0.0052 mmol, 71%).

Computational details

All calculations were conducted using Gaussian 09 program. The geometry was optimized with the restricted Becke Hybrid (B3LYP) at 6-31G(d,p) level implemented on the Gaussian 09, Revision D.01.[46] The optimized local minimum structures at the ground states (S_0) were subjected to TD−DFT calculations with CAM-B3LYP/6-31g(d,p) level in the gas phase to obtain 10 excited states from the lowest energy states (S_1) at the identical level of theory. Torsional scan analysis and population analysis were conducted by DFT calculationat B3LYP/6-31g(d,p) level. Population was calculated by the following equation: [47]

$$P(\varphi) = \exp\left(-E(\varphi) / k_B T\right)$$

Density of states, torsional analysis, and population analysis were reproduced by GaussSum ver 3.

1.10 References

1. Padinger, F.; Rittberger, R. S.; Sariciftci, N. S. *Adv. Funct. Mater.* **2003**, *13*, 85-88.
2. Takimiya, K.; Ebata, H.; Sakamoto, K.; Izawa, T.; Otsubo, T.; Kunugi, Y. *J. Am. Chem. Soc.* **2006**, *128*, 12604-12605.
3. Pisula, W.; Feng, X.; Müllen, K. *Chem. Mater.* **2010**, *23*, 554-567.
4. Sun, Z.; Ye, Q.; Chi, C.; Wu, J. *Chem. Soc. Rev.* **2012**, *41*, 7857-7889.
5. Takimiya, K.; Bulgarevich, K.; Abbas, M.; Horiuchi, S.; Ogaki, T.; Kawabata, K.; Ablat, A. *Adv. Mater.* **2021**, *33*, e2102914.
6. Umeyama, T.; Igarashi, K.; Sasada, D.; Tamai, Y.; Ishida, K.; Koganezawa, T.; Ohtani, S.; Tanaka, K.; Ohkita, H.; Imahori, H. *Chem Sci* **2020**, *11*, 3250-3257.
7. Yu, C. P.; Kumagai, S.; Kushida, T.; Mitani, M.; Mitsui, C.; Ishii, H.; Takeya, J.; Okamoto, T. *J. Am. Chem. Soc.* **2022**, *144*, 11159-11167.
8. Zhang, L.; Cao, Y.; Colella, N. S.; Liang, Y.; Bredas, J. L.; Houk, K. N.; Briseno, A. L. *Acc. Chem. Res.* **2015**, *48*, 500-509.
9. Cui, X.; Xiao, C.; Winands, T.; Koch, T.; Li, Y.; Zhang, L.; Doltsinis, N. L.; Wang, Z. *J. Am. Chem. Soc.* **2018**, *140*, 12175-12180.
10. Kitamura, M.; Arakawa, Y. *J. Phys.: Condens. Matter* **2008**, *20*, 184011.
11. Markiewicz, J. T.; Wudl, F. *ACS Appl Mater Interfaces* **2015**, *7*, 28063-28085
12. Zhan, X.; Facchetti, A.; Barlow, S.; Marks, T. J.; Ratner, M. A.; Wasielewski, M. R.; Marder, S. R. *Adv. Mater.* **2011**, *23*, 268-284.
13. Cui, Y.; Yao, H.; Zhang, J.; Zhang, T.; Wang, Y.; Hong, L.; Xian, K.; Xu, B.; Zhang, S.; Peng, J.; Wei, Z.; Gao, F.; Hou, J. *Nat Commun* **2019**, *10*, 2515.
14. Lai, H.; Chen, H.; Zhu, Y.; Chen, L.; Huang, H.-H.; He, F. *J. Mater. Chem. A* **2020**, *8*, 9670-9676.
15. Lin, Y.; He, Q.; Zhao, F.; Huo, L.; Mai, J.; Lu, X.; Su, C. J.; Li, T.; Wang, J.; Zhu, J. *J. Am. Chem. Soc.* **2016**, *138*, 2973-2976.
16. Yuan, J.; Zhang, Y.; Zhou, L.; Zhang, C.; Lau, T. K.; Zhang, G.; Lu, X.; Yip, H. L.; So, S. K.; Beaupre, S. *Adv. Mater.* **2019**, *31*, e1807577.
17. Facchetti, A.; Deng, Y.; Wang, A.; Koide, Y.; Sirringhaus, H.; Marks, T. J.; Friend, R. H. *Angew. Chem. Int.*

Ed. **2000**, *39*, 4547-4551.

18. Sakmoto, Y.; Komatsu, S.; Suzuki, T. *J. Am. Chem. Soc*. **2001**, *123*, 4643-4644.
19. Sakamoto, Y.; Suzuki, T.; Kobayashi, M.; Gao, Y.; Fukai, Y.; Inoue, Y.; Sato, F.; Tokito, S. *J. Am. Chem. Soc*. **2004**, *125*, 8138-8140.
20. Ie, Y.; Nitani, M.; Ishikawa, M.; Nakayama, K.; Tada, H.; Kaneda, T.; Aso, Y. *Org. Lett*. **2007**, *9*, 2115-2118.
21. Ie, Y.; Jinnai, S.; Nitania, M.; Aso, Y. *J. Mater. Chem. C* **2013**, *1*, 5373-5380.
22. Melucci, M.; Durso, M.; Bettini, C.; Gazzano, M.; Maini, L.; Toffanin, S.; Cavallini, S.; Cavallini, M.; Gentili, D.; Biondo, V. *J. Mater. Chem. C* **2014**, *2*, 3448-3456.
23. Park, S. K.; Kim, J. H.; Yoon, S.-J.; Kwon, O. K.; An, B.-K.; Park, S. Y. *Chem. Mater.* **2012**, *24*, 3263-3268.
24. Cheng, Y.; Chen, C.; Ho, Y.; Chang, S.; Witek, H.; Hsu, C. *Org. Lett*. **2011**, *136*, 1484-5487.
25. Cai, Z.; Zhang, N.; Awais, M. A.; Filatov, A. S.; Yu, L. *Angew. Chem. Int. Ed.* **2018**, *57*, 6442-6448.
26. Kojima, M.; Tamoto, A.; Aratani, N.; Yamada, H. *Chem Commun.* **2017**, *53*, 5698-5701.
27. Su, F.; Chen, S.; Mo, X.; Wu, K.; Wu, J.; Lin, W.; Lin, Z.; Lin, J.; Zhang, H. J.; Wen, T. B. *Chem. Sci.* **2019**, *11*, 1503-1509.
28. Wen, J.; Qiu, F.; Liu, H.; Liu, X.; Hu, H.; Duan, Y.; Wang, Z.; Zhang, L. *Angew. Chem. Int. Ed.* **2022**, *61*, e202112482.
29. Yang, Y.; Wang, Y.; Xie, Y.; Xiong, T.; Yuan, Z.; Zhang, Y.; Qian, S.; Xiao, Y. *Chem. Commun.* **2011**, *47*, 10749-10751.
30. Zhou, Z.; Liu, W.; Zhou, G.; Zhang, M.; Qian, D.; Zhang, J.; Chen, S.; Xu, S.; Yang, C.; Gao, F. *Adv. Mater.* **2020**, *32*, e1906324.
31. Chatterjee, S.; Ie, Y.; Karakawa, M.; Aso, Y. *Adv. Funct. Mater.* **2016**, *26*, 1161-1168.
32. Osaka, I.; Takimiya, K. Naphthobischalcogenadiazole Conjugated Polymers: Emerging Materials for Organic Electronics. *Adv. Mater.* **2017**, *29*, 1625218.
33. Wang, M.; Hu, X.; Liu, P.; Li, W.; Gong, X.; Huang, F.; Cao, Y. *J. Am. Chem. Soc.* **2011**, *133*, 9638-9641.
34. Chatterjee, S.; Ie, Y.; Seo, T.; Moriyama, T.; Wetzelaer, G.-J. A. H.; Blom, P. W. M.; Aso, Y. *NPG Asia Mater.* **2018**, *10*, 1016-1028.
35. Ie, Y.; Jinnai, S.; Oi, A.; Seo, T.; Moriyama, T.; Minami, R.; Higashida, S. *Synthesis* **2021**, *53*, 3390-3396.
36. Iguchi, K.; Mikie, T.; Saito, M.; Komeyama, K.; Seo, T.; Ie, Y.; Osaka, I. *Chem. Mater.* **2021**, *33*, 2218-2228.
37. Aldrich, T. J.; Dudnik, A. S.; Eastham, N. D.; Manley, E. F.; Chen, L. X.; Chang, R. P. H.; Melkonyan, F. S.; Facchetti, A.; Marks, T. J. *macromolecules* **2018**, *51*, 9140-9155.
38. Conboy, G.; Spencer, H. J.; Angioni, E.; Kanibolotsky, A. L.; Findlay, N. J.; Coles, S. J.; Wilson, C.; Pitak, M. B.; Risko, C.; Coropceanu, V. *Mater. Horiz.* **2016**, *3*, 333-339.
39. Nielsen, C. B.; White, A. J.; McCulloch, I. *J. Org. Chem.* **2015**, *80*, 5045-5048.
40. Thorley, K. J.; McCulloch, I. *J. Mater. Chem. C* **2018**, *6*, 12413-12421.
41. da Silva Filho, D. A.; Kim, E. G.; Brédas, J. L. *Adv. Mater.* **2005**, *17*, 1072-1076.
42. Yoshida, H. *Chem. Phys. Lett.* **2012**, *539-540*, 180-185.
43. Yoshida, H. *Anal Bioanal Chem* **2014**, *406*, 2231-2237.
44. Yoshida, H. *J. Phys. Chem. C* **2015**, *119*, 24459-24464.

45. Jinnai, S.; Ie, Y.; Kashimoto, Y.; Yoshida, H.; Karakawa, M.; Aso, Y. *J. Mater. Chem. A* **2017**, *5*, 3932-3938.
46. Gaussian 09, Revision D.01, Frisch MJ, Trucks GW, Schlegel HB, Scuseria GE, Robb MA, Cheeseman JR, Scalmani G, Barone V, Mennucci GAP, Nakatsuji H, Caricato M, Li X, Hratchian HP, Izmaylov AF, Bloino J, Zheng G, Sonnenberg JL, Hada M, Ehara M, Toyota K, Fukuda R, Hasegawa J, Ishida M, Nakajima T, Honda Y, Kitao O, Nakai H, Vreven T, Montgomery JA, Peralta JE, Ogliaro F, Bearpark M, Heyd, JJ, Brothers E, Kudin KN, Staroverov VN, Keith T, Kobayashi R, Normand J, Raghavachari K, Rendell A, Burant JC, Iyengar SS, Tomasi J, Cossi M, Rega N, Millam JM, Klene M, Knox JE, Cross JB, Bakken V, Adamo C, Jaramillo J, Gomperts R, Stratmann RE, Yazyev O, Austin AJ, Cammi R, Pomelli C, Ochterski JW, Martin RL, Morokuma K, Zakrzewski VG, Voth GA, Salvador P, Dannenberg JJ, Dapprich S, Daniels AD, Farkas O, Foresman JB, Ortiz JV, Cioslowski J., Fox DJ, Gaussian, Inc. Wallingford CT, 2013.
47. Yuxuan C, Dmitrii FP. *Angew*. *Chem*. *Int*. *Ed*. **2021**, *60*, 1364-1373.
48. O'Boyle, NM, Tenderholt, AL, Langner KM. *J. Comp*. *Chem.* **2008,** *29*, 839-845.

Chapter 2
Development of periodically twisted molecular wires based on a fused unit

2.1 Introduction

Extended π-conjugated systems, such as molecular wires in single-molecule electronics and organic semiconducting materials in organic thin-film electronics, have been extensively developed as key components. Understanding the relationship between the chemical structure of these π-conjugated systems and their charge transport characteristics is crucial for developing materials suitable for electronic applications. Charge transport in π-conjugated systems is governed by coherent tunneling over short distances and incoherent hopping mechanisms over long distances. While extensive experimental studies on tunneling transport at the single-molecule scale have been conducted, studies on intramolecular hopping charge transport are relatively scarce.

In hopping transport, the movement of charge carriers requires energy to overcome energy barriers between adjacent localized states, that is, hopping sites. The rate of charge flow in hopping transport can be expressed using the Arrhenius equation (1):

$$k = Ae^{\frac{-E_a}{k_B T}} \qquad (1)$$

where k is the rate constant, A is the pre-exponential factor, k_B is the Boltzmann constant, T is the temperature, and E_a is the activation energy. Experimental studies have revealed that the electrical conductance (G) or resistance ($R = G^{-1}$) often follows the Arrhenius equation, with a linear relationship between resistance and molecular length (L) expected for hopping transport. The key factor, E_a, is understood to be the sum of the reorganization energy of the hopping site (λ) and the energy difference between hopping sites (ΔE_{hs}), which is influenced by structural fluctuations due to thermal motion (Fig. 2-1a). For efficient intramolecular hopping transport, it is essential to reduce both λ and ΔE_{hs}. However, experimental studies on these aspects remain challenging due to the lack of appropriate model molecular systems.

To reduce λ, structural fluctuations between the neutral and charged states (radical cations/anions) must be minimized. In this context, fused π-conjugated structures have been found effective in achieving low λ values. For example, fully fused porphyrin tapes exhibit low conductance decay and function as highly conductive molecular wires. Nakamura *et al*. reported that carbon-bridged oligo(*p*-phenylenevinylene) molecular wires exhibit a high photoinduced electron transfer rate. In contrast, experimental studies aimed at reducing ΔE_{hs} are still in the early stages. Terao *et al*. reported enhanced charge mobility in zigzag-type poly(*p*-phenylene-ethynylene) frameworks, specifically **IMWs 10**, where π-orbitals are intentionally separated by meta-junctions (Fig. 2-1b). Ie and coworkers demonstrated that structures with repeated twisted thiophene units can be used to control the electronic structures of hopping sites in oligothiophenes, reducing ΔE_{hs}. Periodically twisted oligothiophenes containing head-to-head 3,3'-dihexyl-2,2'-bithiophene skeletons (**NCS-(6T^{seg})$_n$-SCN**) exhibited efficient intramolecular hopping-transport characteristics (Fig. 2-1b). However, the flexible C–C single bonds in *p*-phenylene-ethynylene and oligothiophenes may contribute toλ and inhomogeneous ΔE_{hs} due to thermal fluctuations.

In this study, the author presented the molecular design and synthesis of a twisted π-extended system based on a rigid repeating unit, fused thienobenzo[b]indacenothiophene (**TBID**), which is based on indacenodithiophene (**IDT**)

and two benzothiophenes (Fig. 2-1c). Building on previous molecular design for reducing ΔE_{hs},[33] octyl groups were attached to the β-positions of the terminal thiophene rings. This modification introduces a twist between neighboring **TBID** units, achieved through head-to-head steric repulsion. To suppress intermolecular π-π interactions, orthogonally oriented *p*-hexylphenyl groups were introduced into the cyclopentadiene segments. Thiocyanate (SCN) groups were attached to the molecular terminals as anchors to the Au electrodes. The resulting molecule is referred to as **NCS-(TBID)$_n$-SCN**. Given that the calculated molecular length of **TBID** is only 0.3 nm shorter than that of **6T^{seg}**, the conductance of these molecules can be compared, as they have similar lengths and numbers of hopping sites. Single-molecule conductance measurements in the hopping regime revealed that **NCS-(TBID)$_n$-SCN** exhibited higher molecular conductance and a lower E_a compared to **NCS-(6T^{seg})$_n$-SCN**.

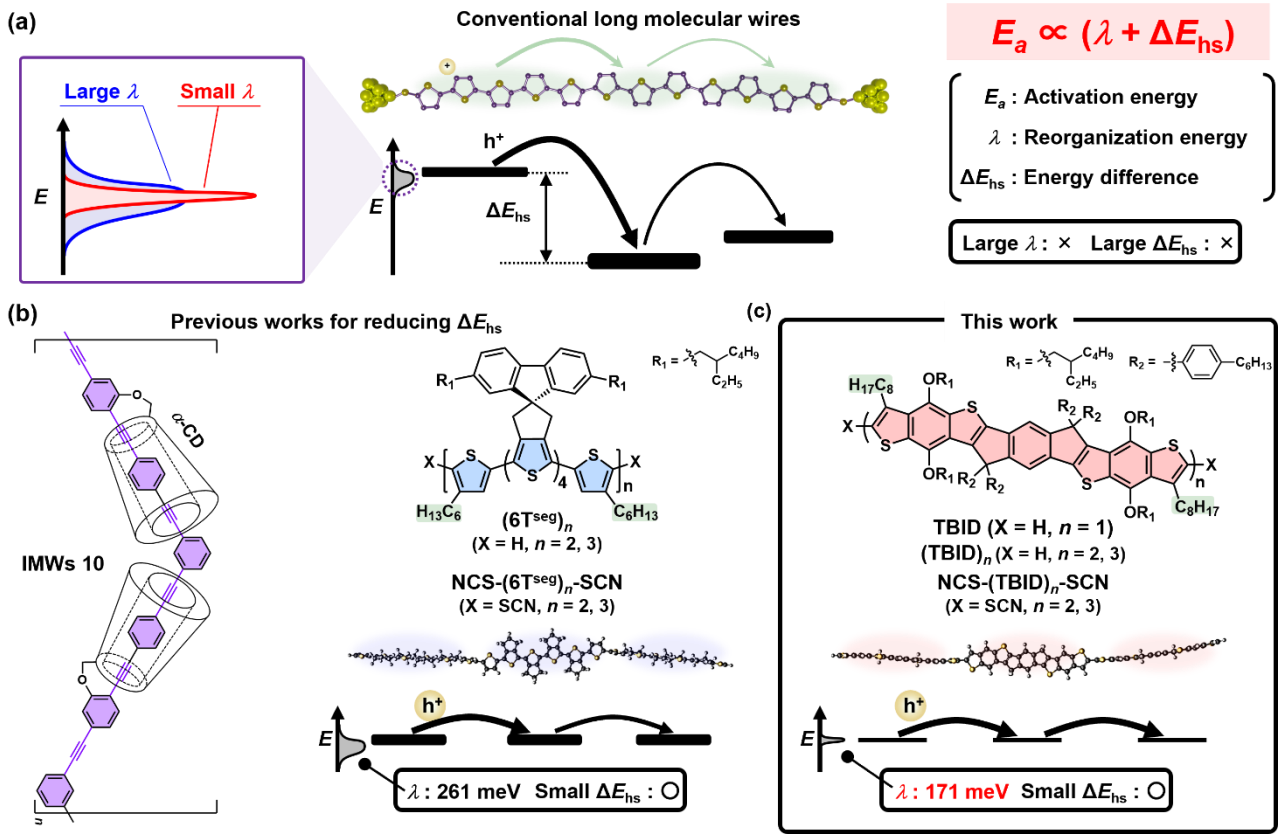

Figure 2-1. (a) Schematic of hopping transport and relationship between E_a, λ, and ΔE_{hs}; h^+ stands for holes. Molecular structures of (b) **IMWs 10**, **6T^{seg}**, and **NCS-(6T^{seg})$_n$-SCN** and (c) **(TBID)$_n$**, **NCS-(TBID)$_n$-SCN** along with their schematic structure models and energy diagrams. The difference in the line thickness in the energy diagrams represents fluctuations due to thermal motion.

2.2 Calculated electronic structures

Tuning the electronic structures of π-conjugated molecules to be suitable for hopping transport is crucial for utilizing them as hopping sites. To elucidate the relationship between chemical and electronic structures, the author analyzed the frontier molecular orbitals and λ of oligothiophenes and three **IDT**-based fused molecules (Fig. S2-1). Alkyl groups in these compounds were replaced with methyl groups to reduce computational costs (denoted as **6T^{seg}(Me)**, **8T^{seg}(Me)**, **IDT(Me)**, **TBID(Me)**, and **IDTTBDT(Me)** for clarity) (Fig. 2-2a, Fig. S2-2a). The calculated highest occupied molecular orbital (HOMO) energy levels and λ values for the cationic state were also plotted against molecular length (Fig. 2-2). The HOMO energy level and λ of **6T^{seg}(Me)** were calculated to be −4.54 eV and 261 meV, respectively. Extending the molecular length from **6T^{seg}(Me)** (2.4 nm) to **8T^{seg}(Me)** (3.2 nm) resulted in a shallower HOMO energy level of −4.42 eV and a decreased λ value of 223 meV. These trends suggest that **8T^{seg}(Me)** may be conducive to acting as a hopping site due to the reduced charge injection barrier and structural fluctuations. However, single-molecule conductance measurements showed that **NCS-(8T^{seg})$_3$-SCN** exhibited lower hopping conductance than **NCS-(6T^{seg})$_3$-SCN**.[33] Focusing on the molecular orbitals, the HOMO of **6T^{seg}(Me)** is delocalized over the entire oligothiophene framework, whereas the HOMO of **8T^{seg}(Me)** is mainly localized in the central thiophene 6-mer unit (Fig. S2-2a). Based on these results, the author concludes that achieving the desired HOMO energy level and λ together with a delocalized HOMO orbital is crucial for designing effective hopping sites.

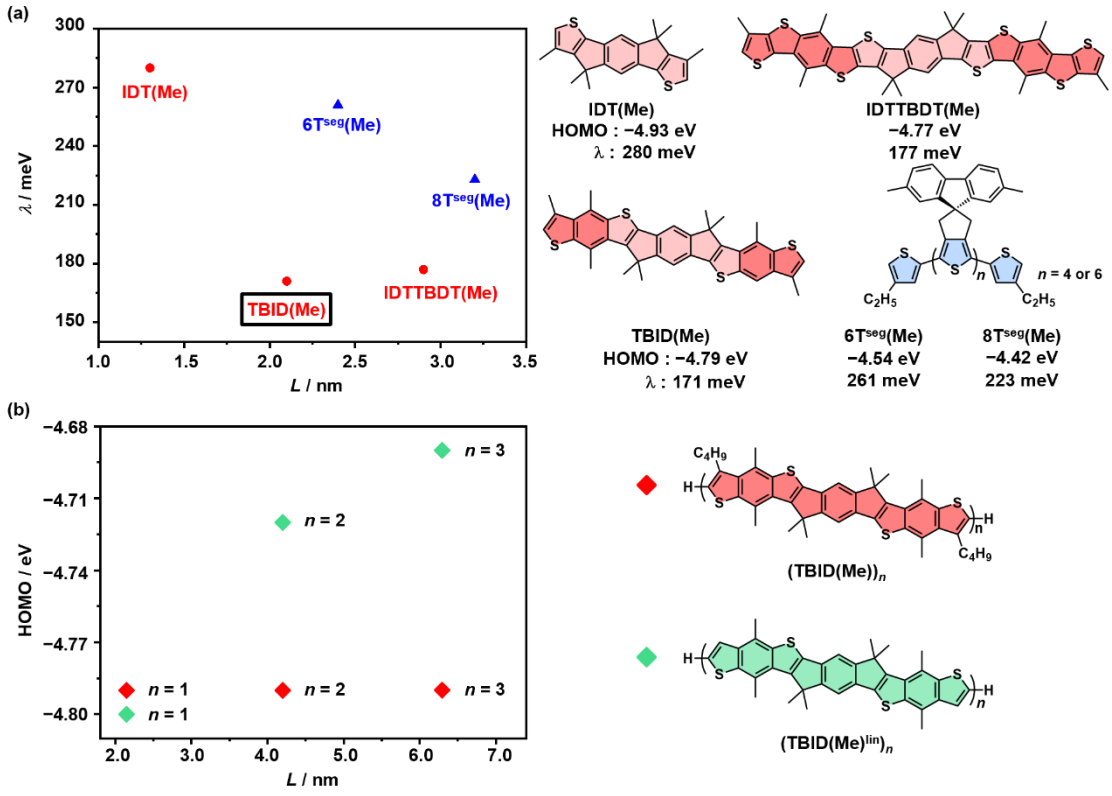

Figure2-2. Optimized chemical structures obtained via density functional theory (DFT) calculations performed at the B3LYP/6-31g(d,p) level. (a) Reorganization energies against molecular length. (b) HOMO energy levels against molecular length. For the calculations of **(TBID(Me))$_n$** (n = 2, 3), butyl groups are attached at the β-positions of terminal thiophene rings.

Table S2-1. Calculated energy levels of **[TBID(Me)]$_n$** and **(TBID(Me)^{lin})$_n$** at the B3LYP/6-31g(d,p) level.

Compounds	HOMO / eV	LUMO / ev	HOMO-LUMO gap / eV
TBID(Me)	−4.79	−1.61	3.19
[TBID(Me)]$_2$	−4.79	−1.77	3.02
[TBID(Me)]$_3$	−4.79	−1.75	3.04
TBID(Me)^{lin}	−4.80	−1.64	3.16
(TBID(Me)^{lin})$_2$	−4.72	−2.05	2.67
(TBID(Me)^{lin})$_3$	−4.69	−2.13	2.56

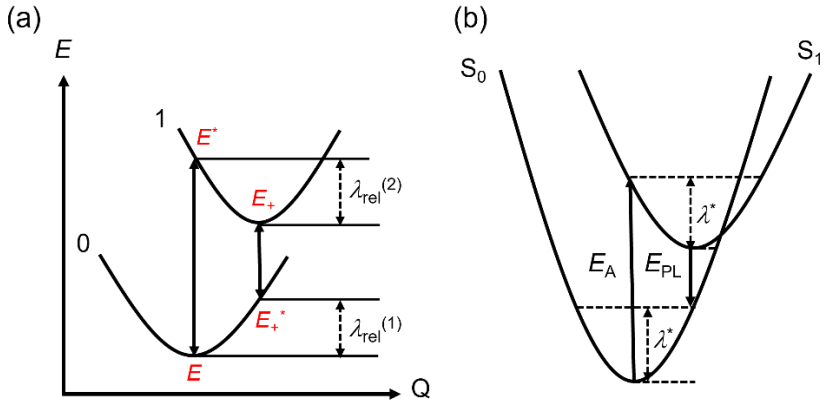

Figure S2-1. Schematic energy diagrams of (a) λ and (b) λ^*.

The author examined the electronic structures of the fused molecules **IDT(Me)**, **TBID(Me)**, and **IDTTBDT(Me)**. The HOMO energy level of **TBID(Me)** (−4.79 eV) was shallower than that of **IDT(Me)** (−4.93 eV), and it demonstrated a similar value to that of **IDTTBDT(Me)** (−4.77 eV). The λ value of **TBID(Me)** (171 meV) was significantly lower than that of **IDT(Me)** (280 meV). However, further extension of the fused structure from **TBID(Me)** to **IDTTBDT(Me)** had a negligible effect on decreasing λ (**IDTTBDT(Me)**: λ = 177 meV). Moreover, the HOMO of **IDTTBDT(Me)** was localized in the central region, leading to a decreased HOMO distribution at the terminal thiophene units, in contrast to the delocalized HOMO of **TBID(Me)**. Therefore, the author chose **TBID(Me)** as the repeating unit to investigate chain-length dependence.

To understand the influence of twisting on the molecular and electronic structures, the author optimized **[TBID(Me)]$_2$** and **[TBID(Me)]$_3$**, as well as the corresponding non-twisted structures (**(TBID(Me)^{lin})$_n$** (n = 1–3)). As shown in Fig. S2-2b, both **[TBID(Me)]$_2$** and **[TBID(Me)]$_3$** exhibited significantly twisted structures with dihedral angles of approximately 80° between neighboring **TBID(Me)** units. This result contrasts sharply with the planar structures of **(TBID(Me)^{lin})$_n$**. The calculated HOMO and lowest unoccupied molecular orbital (LUMO) energy levels are summarized in Table S2-1. The length-dependent HOMO energy levels of **[TBID(Me)]$_n$** (n = 1–3) and **(TBID(Me)^{lin})$_n$** (n = 1–3) are illustrated in Fig. 2-2b. For **(TBID(Me)^{lin})$_n$**, shallower HOMO energy levels were observed with an increase in the number of repeating units, which is consistent with the conventional trend for extended π-conjugated systems. This phenomenon indicates that the hopping sites of **(TBID(Me)^{lin})$_n$** are not aligned at the same energy level due to variations in the local molecular structure, resulting in a large ΔE_{hs}. In contrast,

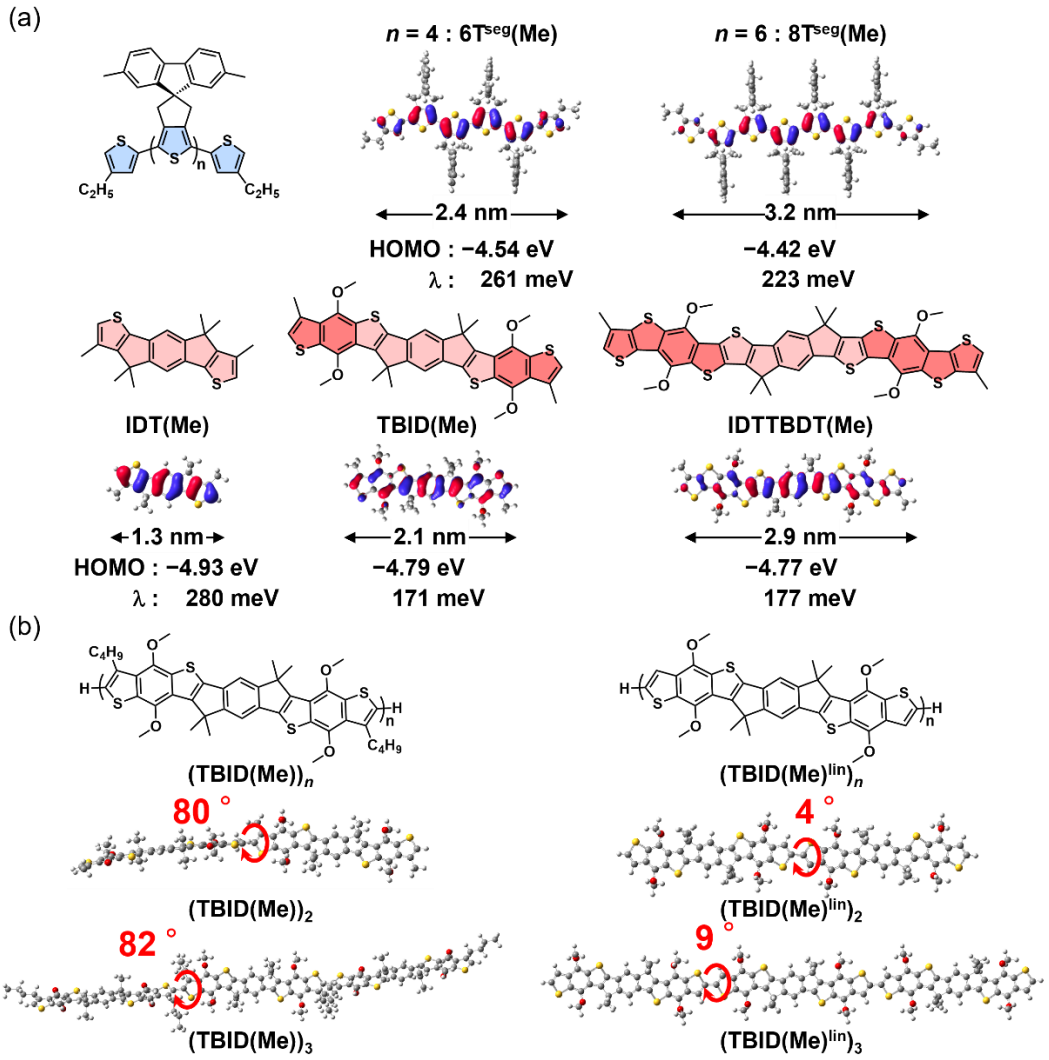

Figure S2-2. (a) Molecular structures, HOMO orbitals, calculated HOMO energy levels, and λ values of oligothiophenes and fused-type compounds. (b) Molecular structures and Kohn-Sham optimized molecular structures for **[TBID(Me)]$_n$** and **(TBID(Me)^{lin})$_n$**. The structures were optimized at the B3LYP/6-31g(d,p) level.

for the twisted structures, the effective conjugation of **[TBID(Me)]$_2$** and **[TBID(Me)]$_3$** was disrupted, leading to HOMO energy levels similar to that of **TBID(Me)**. Based on these results, the author concludes that **TBID(Me)** is an ideal chemical structure for the hopping sites in this study.

2.3 Synthesis

The synthesis routes for **(TBID)$_n$** (n = 1–3) and **NCS-(TBID)$_n$-SCN** (n = 1–3) are illustrated in Scheme 2-1. The starting material, stannylated benzodithiophene ***β*-C8-BDT-Sn**, was synthesized in four steps from a known di-alkoxylated benzodithiophene (Scheme S2-1). Compound **1** was synthesized via a Stille coupling of ***β*-C8-BDT-Sn** with diethyl 2,5-dibromoterephthalate. The nucleophilic addition of *p*-hexylphenyl lithium to **1**, followed by cyclization under acidic conditions, yielded **TBID**. This was then treated with NBS to obtain **TBID-Br**. A subsequent Stille coupling reaction of **TBID-Br** with hexamethylditin $(SnMe_3)_2$ was conducted.

Scheme 2-1. Synthetic routes of **(TBID)$_n$** (n = 1–3) and **NCS-(TBID)$_n$-SCN** (n = 1–3).

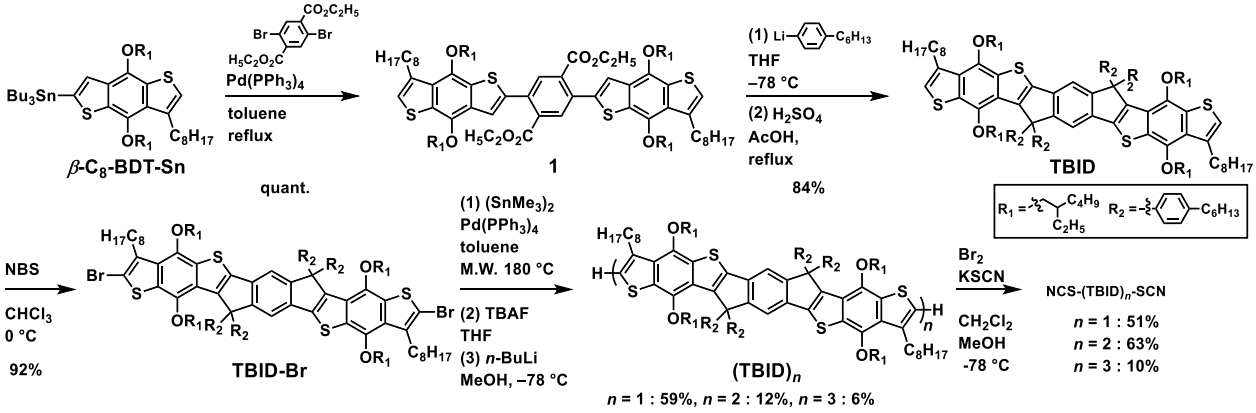

Scheme S2-1. Synthetic routes for ***β*-C8-BDT-Sn** and **BPB**.

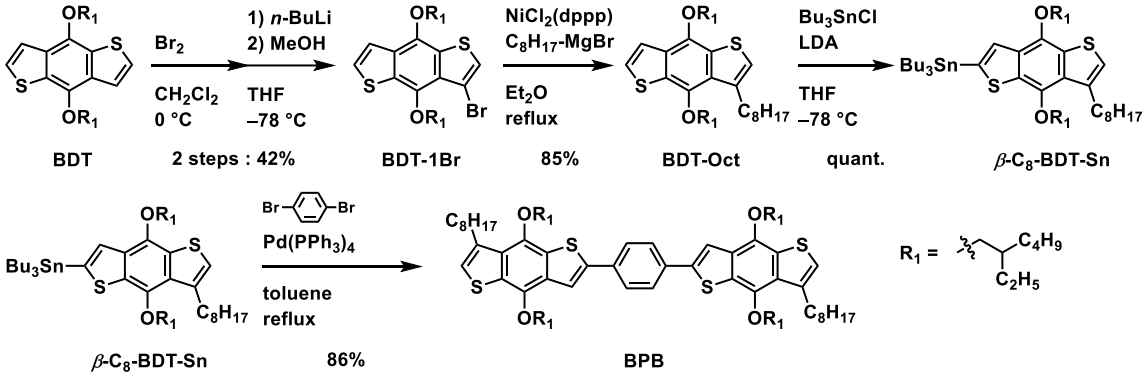

The remaining $SnMe_3$ and Br groups in the products were removed by destannylation and protonation reactions. The resulting mixtures of oligomers were separated by gel permeation chromatography. Finally, the SCN groups were introduced through treatment with bromine and potassium thiocyanate, yielding **NCS-(TBID)$_n$-SCN**. All compounds were comprehensively characterized using ^{1}H NMR, ^{13}C NMR, and mass spectrometry techniques.

2.4 Photophysical and electrochemical properties

To investigate the effect of the electronic structures of the hopping sites on the photophysical properties, the UV-vis spectra of **TBID** and its non-fused counterpart **BPB** (chemical structure shown in Fig. 2-3a) in dichloromethane (CH_2Cl_2) solution were measured. As shown in Figs. 2-3a and S2-3, **TBID** exhibited three sharp absorption bands

Table 2-1. Summary of physical properties.

Compounds	L /nm[a]	$\lambda_{abs,max}$ /nm[b]	ε / L mol^{-1} cm^{-1}[b]	$\lambda_{PL,max}$ / nm [b]	E_{ox} / eV[c]	HOMO / eV
TBID	2.12	442	5.3 ×10^5	551	0.35	−5.15
(TBID)$_2$	4.39	453	9.8 ×10^5	551	0.37	−5.17
(TBID)$_3$	6.47	456	15 ×10^5	551	0.37	−5.17

[a]The L value of each structure is estimated from the optimized structures of **(TBID)$_n$**. [b]In CH_2Cl_2. [c]E_{ox} denotes the first oxidation potential determined by DPV in CH_2Cl_2 containing 0.1 M of $TBAPF_6$. [d]Estimated by $E_{HOMO} = -(E_{ox} + 4.80)$ eV

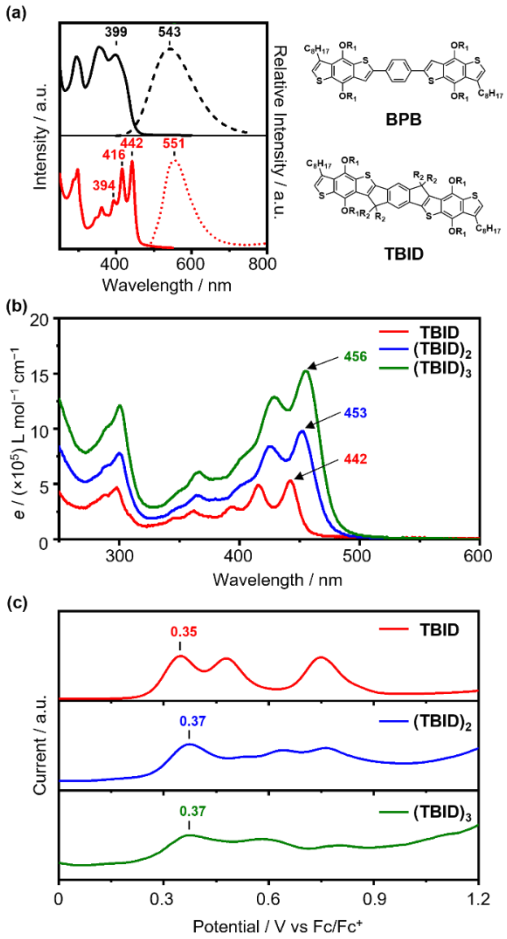

Figure 2-3. (a) UV-vis absorption (solid line) and fluorescence spectra (dashed line) of **TBID** (red) and **BPB** (black) in CH_2Cl_2. (b) UV-vis absorption spectra of **TBID** (red), **(TBID)$_2$** (blue), and **(TBID)$_3$** (green) in CH_2Cl_2. (c) Differential pulse voltammograms of **TBID** (red), **(TBID)$_2$** (blue), and **(TBID)$_3$** (green) in CH_2Cl_2 containing 0.1 M $TBAPF_6$.

at 394, 416, and 442 nm. In contrast, **BPB** displayed a relatively broad absorption band without the vibronic structures. The presence of vibronic structures in **TBID** indicates a rigid structure due to the fused ring system. Fluorescence measurements of **TBID** and **BPB** in CH_2Cl_2 solution were performed, as the photophysical properties in the excited state are influenced by the molecular dynamics. As illustrated in Fig. 2-3a and Table S2-2, **TBID** exhibited a maximum emission wavelength of 551 nm, similar to that of **BPB** (543 nm).

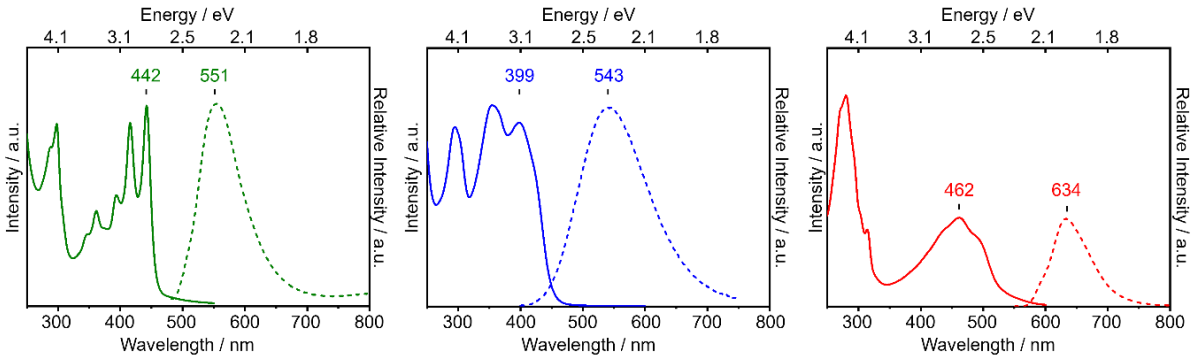

Figure S2-3. UV-vis absorption and fluorescence spectra of **TBID** (green), **BPB** (blue), and **6T^{seg}** (red) in CH_2Cl_2.

Table S2-2. Electronic properties.

Compounds	$\lambda_{abs,max}$ / nm	$\lambda_{PL,max}$ / nm	λ_{hw} / cm^{-1}	Stokes shift / cm^{-1}	λ^* / eV
TBID	442	551	2600	4500	0.28
BPB	399	543	4300	6600	0.41
6T^{seg}	462	634	17000	5900	0.37

λ_{hw} : The half-width of the emission band.

However, the half-width of the emission band for **TBID** (2600 cm^{-1}) was noticeably narrower compared to **BPB** (4300 cm^{-1}). The Stokes shift of **TBID** was determined to be 4500 cm^{-1}, which is significantly smaller than that of BPB (6600 cm^{-1}). These results indicate that: 1) **TBID** underwent smaller conformational changes in the excited state due to its rigid chemical structure, and 2) the local excited state of **TBID** was similar to that of **BPB**. To support this hypothesis, theoretical structural optimization of the first excited state (S_1) was performed for **TBID(Me)** and **BPB(Me)**. As shown in Fig. S2-4, the non-fused **BPB** displayed a large conformational change during excitation, eventually forming a planar structure in the S_1 state due to the formation of bonding molecular orbitals. In contrast, **TBID(Me)** showed only limited structural changes. These observations are further supported by the reorganization energy upon photoexcitation (λ^*) (Fig. S2-1). The λ^* value for **TBID** (0.28 eV) was smaller than those for **BPB** (0.41 eV) and **6T^{seg}** (0.37 eV). As shown in Fig. 2-3b, the absorption spectra of **(TBID)$_n$** (n = 1–3) in CH_2Cl_2 solution exhibited nearly identical spectral shapes with clear vibronic structures, regardless of the number of units.

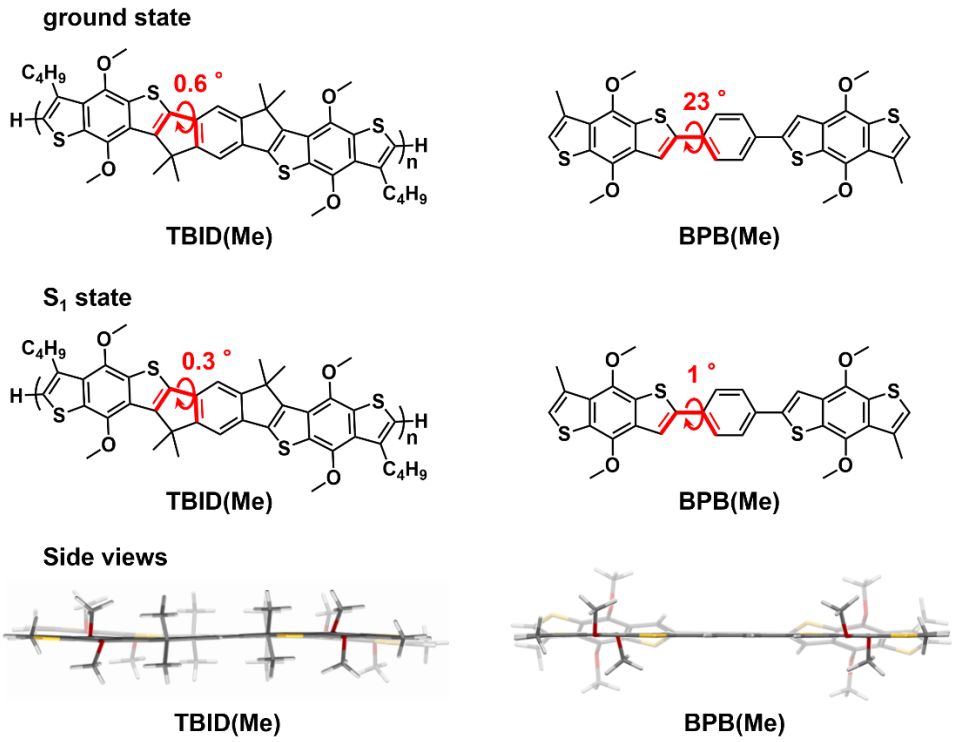

Figure S2-4. Optimized structures of **TBID(Me)** and **BPB(Me)** at the ground (top) and S_1 state (middle). The bottom images show the side views of S_1 (solid stick) and the ground (semitransparent stick) states. Optimization was conducted at the B3LYP/6-31g(d,p) level for the ground state and CAM-B3LYP/6-31g(d,p) level for the S_1 state.

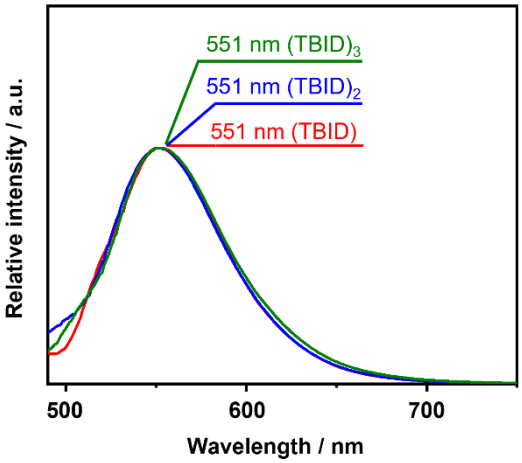

Figure S2-5. Fluorescence spectra of **TBID** (red), **(TBID)$_2$** (blue), and **(TBID)$_3$** (green) in CH_2Cl_2.

However, the molar absorption coefficients (ε) increased linearly from **TBID** to **(TBID)$_3$** due to the increase in the number of **TBID** units. The $\lambda_{abs,max}$ value was 442 nm for **TBID**, whereas those of the dimer **(TBID)$_2$** and trimer **(TBID)$_3$** were 453 and 456 nm, respectively (Table 2-1). The observed slight redshift for **(TBID)$_2$** and **(TBID)$_3$** originated from electronic perturbations due to the inductive effect of the electron-rich **TBID** units. Time-dependent DFT calculations predicted that **[TBID(Me)]$_2$** has a slightly narrower HOMO-LUMO energy gap compared to that of **TBID(Me)** (Table S2-1). As shown in Fig. S2-5, the fluorescence spectra of **(TBID)$_n$** exhibited identical shapes with the same maximum emission peak at 551 nm. This result suggests that these oligomers form similar molecular structures with nearly equal energy levels in the excited states, regardless of the number of units.

To investigate the electrochemical properties, the oxidation potentials of **(TBID)$_n$** (n = 1–3) and **BPB** were measured using differential pulse voltammetry (DPV) in a CH_2Cl_2 solution containing tetrabutylammonium hexafluorophosphate ($TBAPF_6$). As shown in Fig. 2-3c, all compounds exhibited oxidation waves. The first oxidation potential of **(TBID)$_n$** (0.35 V) was positively shifted compared to that of **BPB** (0.41 V) (Fig. S2-6), consistent with the shallower calculated HOMO energy level of **BPB(Me)**. Increasing the molecular length had minimal effect on the first oxidation potential (Table 2-1). Assuming that the Fc/Fc^+ couple is below 4.8 eV from the vacuum level, the experimentally determined HOMO energy levels of **TBID**, **(TBID)$_2$**, and **(TBID)$_3$** were calculated to be −5.15, −5.17, and −5.17 eV, respectively (Table 2-1). These photophysical and electrochemical results suggest that electronic communication between the TBID units is restricted, indicating that the electronic states of **(TBID)$_n$** are suitable for hopping transport in single-molecule junctions.

2.5 Photophysical properties of radical cationic species

As the radical cationic species (polaronic state) of conjugated molecules are directly related to the carrier species in single-molecule conduction, the UV-vis-NIR spectra of **TBID** and **(TBID)$_2$** in a one-electron oxidation state were investigated in CH_2Cl_2 solution. Tris(4-bromophenyl)ammoniumyl hexachloroantimonate (magic blue) was used as the oxidant. As shown in Fig. 2-4a, upon the addition of 1 equivalent of magic blue, **TBID**$^{\cdot+}$ formed with two absorption bands at P1 = 0.95 eV and P2 = 1.98 eV. Based on the calculation of **[TBID(Me)]**$^{\cdot+}$ at the CAM-

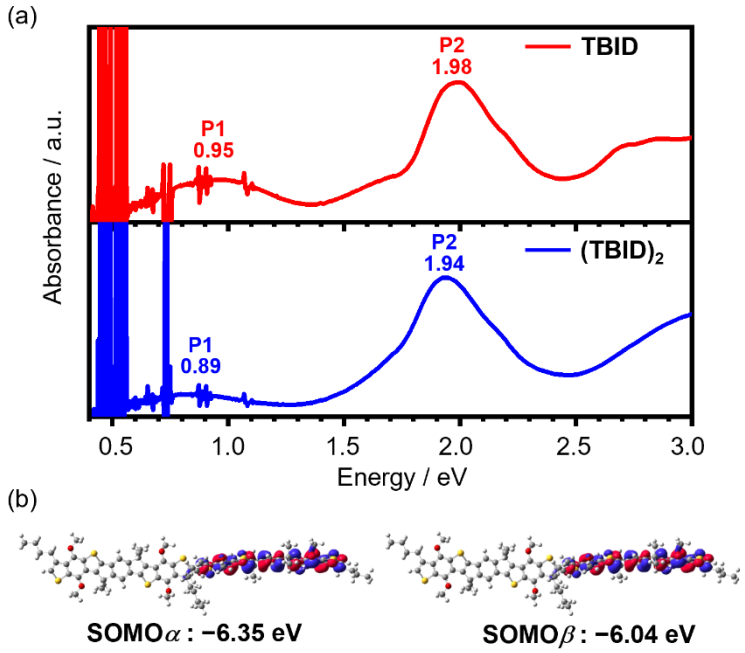

Figure 2-4. (a) UV-vis-NIR spectra of **TBID** (top) and **(TBID)$_2$** (bottom) in CH_2Cl_2 under oxidation with magic blue. (b) Calculated SOMO orbitals of **(TBID(Me))$_2$**$^{\cdot+}$ at the CAM-B3LYP/6-31g(d,p) level.

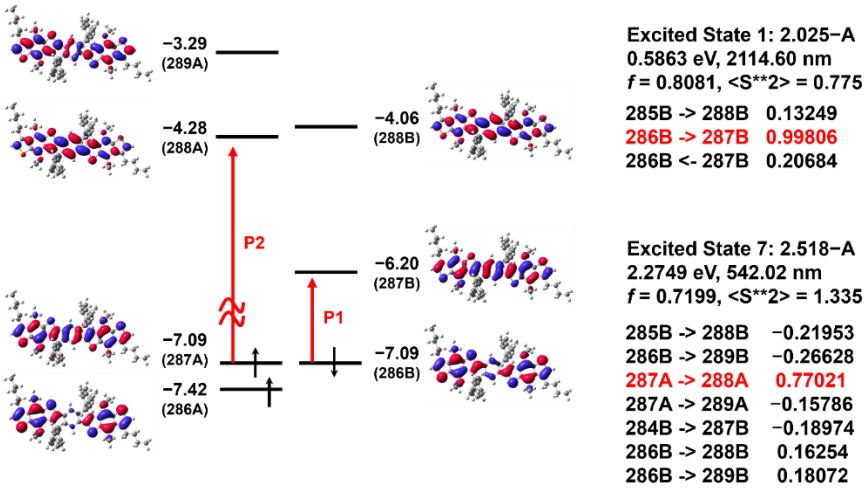

Figure S2-7. Calculated energy levels of radical cationic state for **TBID(Me)** and estimated excited states. Optimization was conducted at the B3LYP/6-31g(d,p) level. Optimized local minimum structures at the excited state were subjected to TD-DFT calculations at the CAM-B3LYP/6-31g(d,p) level.

B3LYP/6-31g(d,p) level, the P1 and P2 bands were assigned as HOMO-singly occupied molecular orbital (SOMO) and SOMO-LUMO transitions, respectively (Fig. S2-7). The corresponding P1 and P2 bands of**(TBID)$_2$**$^{\cdot+}$ were observed at 0.89 eV and 1.94 eV, respectively, which closely resembled those of **(TBID)**$^{\cdot+}$. To understand this phenomenon, the most stable structure of **[TBID(Me)]$_2$** in its radical cationic state was determined.

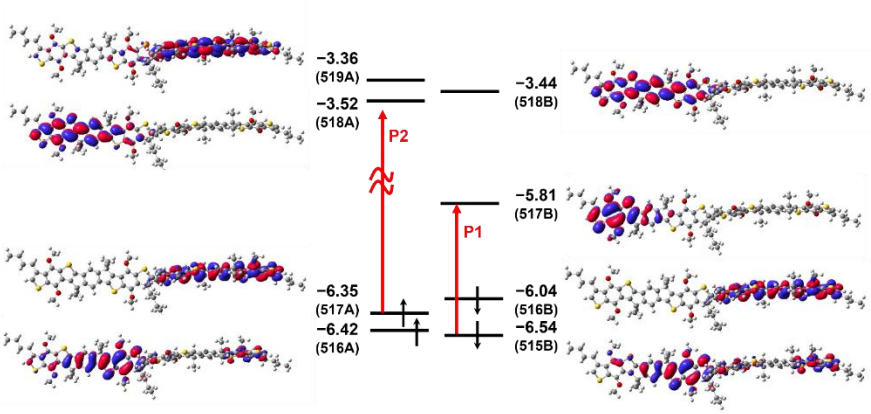

Figure S2-8. Calculated energy levels of radical cationic state for **(TBID(Me))$_2$** and estimated excited states. Optimization was conducted at the B3LYP/6-31g(d,p) level. Optimized local minimum structures at the excited state were subjected to TD-DFT calculations at the CAM-B3LYP/6-31g(d,p) level.

As illustrated in Fig. S2-8, **[TBID(Me)]$_2^{\cdot+}$** exhibited a highly twisted conformation with a dihedral angle of 78°, caused by the steric repulsion in its head-to-head conformation. Therefore, the electronic distributions of the SOMOs for **[TBID(Me)]$_2^{\cdot+}$** were localized on either side of the **TBID(Me)** unit (Fig. 2-4b). These results indicate that the P1 and P2 bands of **(TBID)$_2^{\cdot+}$** arise from the **TBID** unit, owing to the periodically twisted structures. From this perspective, the hopping sites of **(TBID)$_n$** are aligned at the same energy levels due to the restricted effective conjugation length, making them suitable as molecular wires for effective hopping transport.

2.6 Single-molecule conductance measurements

The electrical conductance of **NCS-(TBID)$_n$-SCN** (n = 1–3) was measured using the scanning tunneling microscope-break junction (STM-BJ) method.[18, 38] Briefly, a gold STM tip was repeatedly brought into contact with a gold substrate modified with the molecules. Molecular junctions formed when the contact between the gold tip and gold substrate was broken during the tip retraction process. Steps or plateaus were observed in the conductance traces measured during tip retraction when single-molecule junctions were formed.

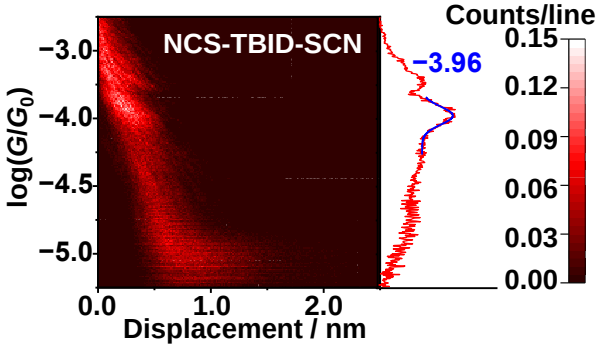

Figure S2-9. 2D conductance histogram of **NCS-TBID-SCN** at 300 K. The corresponding conductance histogram is shown beside the 2D histograms. Blue curves represent the Gaussian function fitted to the histogram to determine the conductance values.

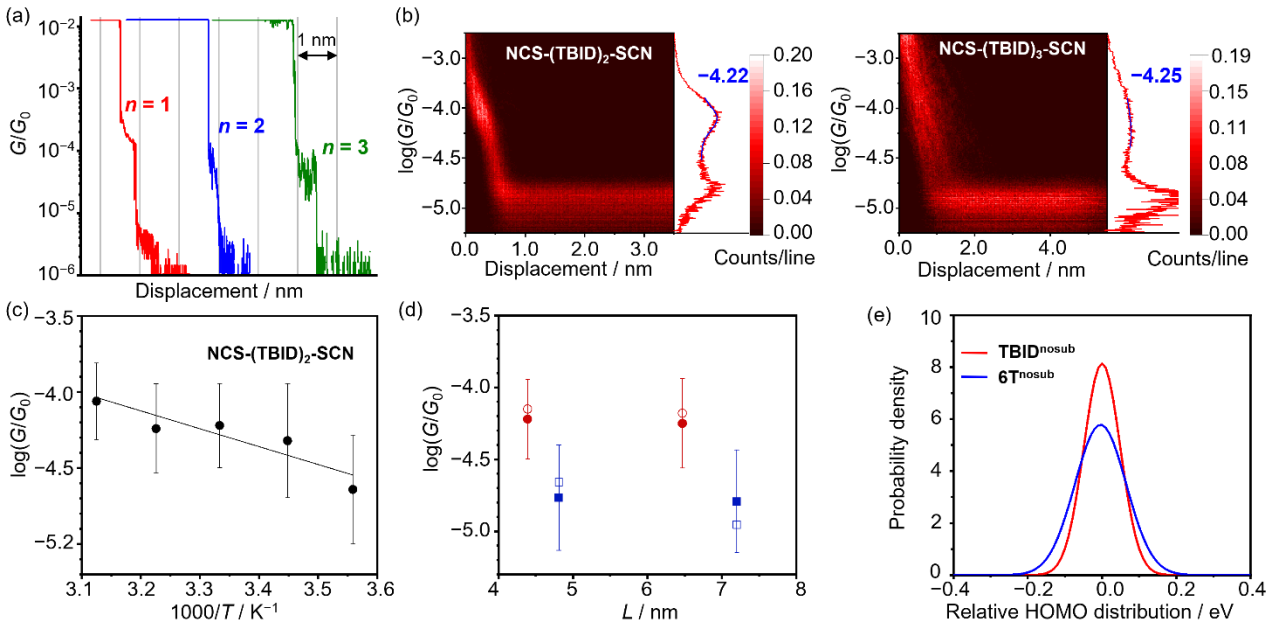

Figure 2-5. (a) Typical conductance transients observed for **NCS-(TBID)$_n$-SCN** (n = 1−3). Note that $G_0 = 2e^2h^{-1}$, where e and h are the elementary charge and Planck's constant, respectively. (b) 2D conductance histograms of **NCS-(TBID)$_n$-SCN** (n = 2, 3). The corresponding conductance histograms of each molecule are illustrated beside the 2D histograms. Blue curves represent the Gaussian function fitted to the histogram to determine the conductance values. (c) Log(G/G_0) versus T^{-1} for **NCS-(TBID)$_2$-SCN**. (d) Log(G/G_0) versus molecular length for **NCS-(TBID)$_n$-SCN** (n = 2, 3) (red circle) and **NCS-(6T^{seg})$_n$-SCN** (n = 2, 3) (blues square). Filled and open symbols denote experimental and simulated values, respectively. (e) Probability density functions obtained by fitting the histograms.

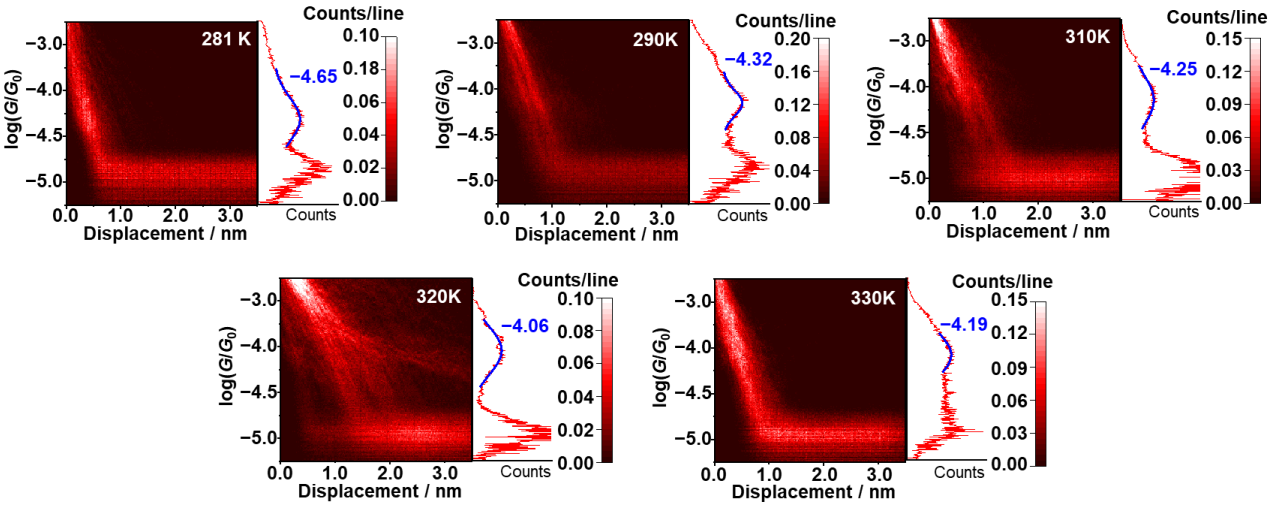

Figure S2-10. 2D conductance histograms of **NCS-(TBID)$_2$-SCN** at 281, 290, 310, 320, and 330 K. The corresponding conductance histograms of each molecule are shown beside the 2D histograms. Blue curves represent the Gaussian function fitted to the histogram to determine the conductance values. The peaks around 10^{-5} G_0 are attributed to background noise of our measurement system and the peak except the background noise was used to determine the conductance values.

Figs. 2-5a, b, and S2-9 illustrate typical conductance traces with plateaus observed for **NCS-(TBID)$_n$-SCN** and the corresponding two-dimensional (2D) conductance-displacement histograms derived from the conductance traces with plateau lengths greater than 0.5 nm. The plateau lengths observed in the 2D histograms are shorter than the calculated molecular lengths, which can be attributed to the breaking of molecular junctions and the change in tilting angle during the pulling process values,[39] $G = 1.7\times10^{-4}$, 9.8×10^{-5}, and 4.0×10^{-5} G_0 in G histograms, determined by Gaussian fitting, correspond to the conductance values for **NCS-(TBID)$_n$-SCN** : n = 1, 2, and 3, respectively. To obtain E_a, the temperature dependence of G was measured for **NCS-(TBID)$_2$-SCN**, and the 2D histograms are summarized in Fig. S2-10. As shown in Fig. 2-5c, typical Arrhenius behavior was observed between 290 and 330 K, and E_a = 0.12 eV was obtained, which is smaller than that of **NCS-(6T^{seg})$_2$-SCN** (0.15 eV). This result indicates that the **TBID** unit effectively reduces the activation energy. Fig. 2-5d illustrates G versus L for the molecular wires exhibiting hopping transport characteristics, i.e., **NCS-(TBID)$_n$-SCN** (n = 2, 3), compared to those of **NCS-(6T^{seg})$_n$-SCN** (n = 2, 3) (values taken from reference 33). All comparative data for **NCS-(TBID)$_n$-SCN** (n = 1, 2, 3) are shown in Fig. S2-11. The reported single-molecule conductance values for representative molecular wires with hopping transport characteristics are summarized in Fig. S2-12 and Table S2-3. The G values of **NCS-(TBID)$_n$-SCN** are higher than those of **NCS-(6T^{seg})$_n$-SCN** and other molecular wires with similar molecular lengths. The length dependence of G is extremely small for both molecules, as illustrated in Fig. 2-5d. These results indicate that the fused π-conjugated compounds are effective structures for hopping sites due to the reduced λ for efficient intramolecular hopping charge transport.

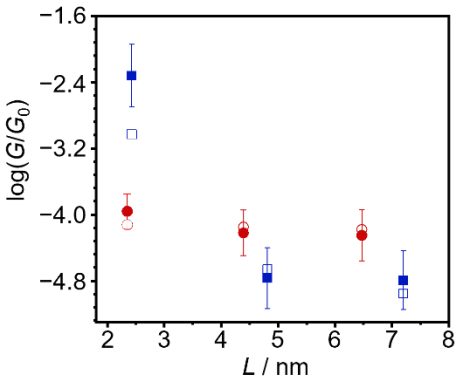

Figure S2-11. Log(G/G_0) versus molecular length for **NCS-(TBID)$_n$-SCN** (n = 1, 2, and 3) (red circle) and **NCS-(6T^{seg})$_n$-SCN** (n = 1, 2, and 3) (blues square). Filled and open symbol denotes experimental and simulated values, respectively.

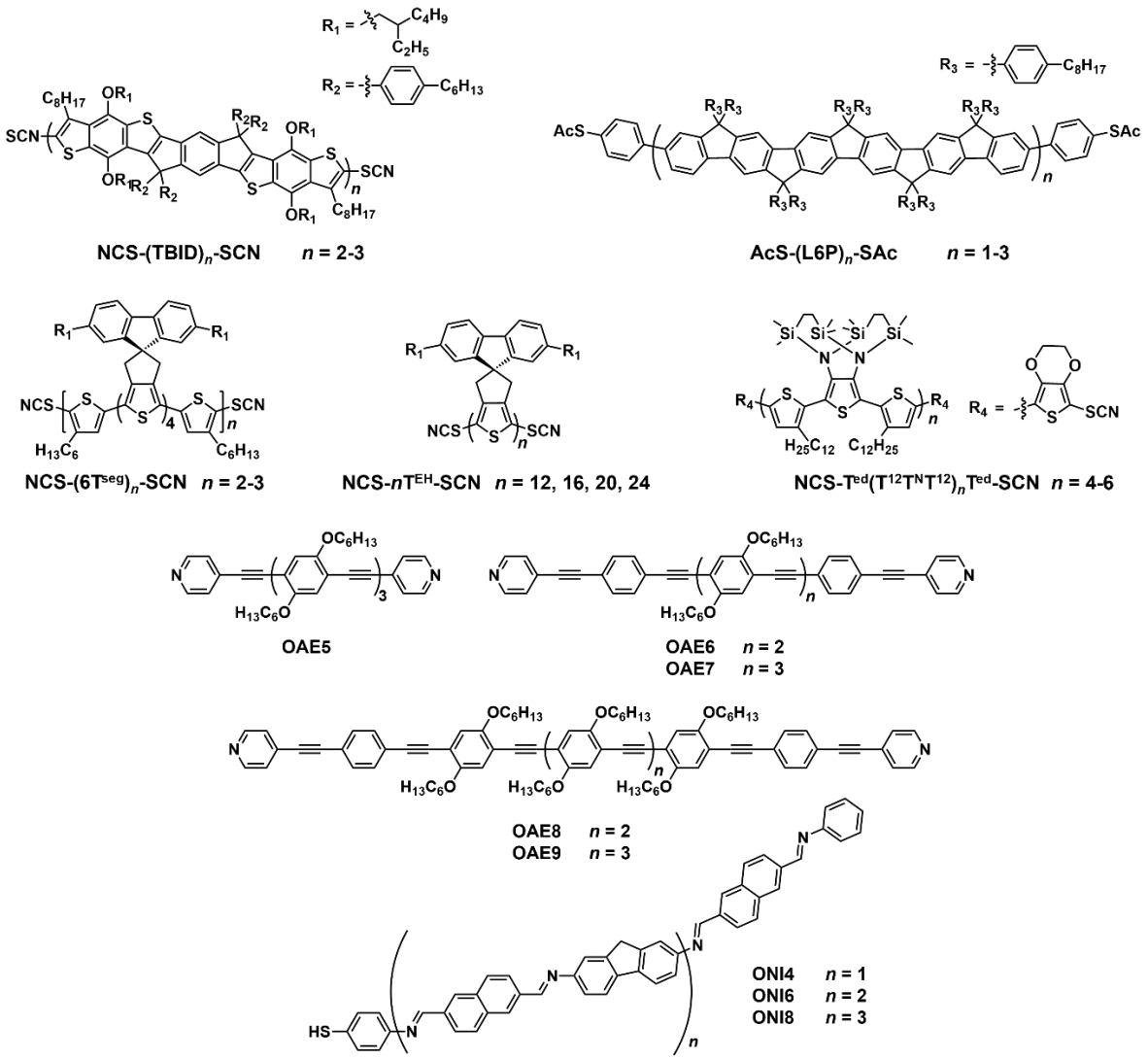

Figure S2-12. Molecular structures of molecular wires with hopping-transport characteristics.

Table S2-3. Conductance values of molecular wires with hopping-transport characteristics.

Compounds	L / nm [a]	$\log(G/G_0)$	Methods	Reference
NCS-(TBID)$_2$-SCN	**4.3**	**−4.2**	STM-BJ	This work
NCS-(TBID)$_3$-SCN	**6.4**	**−4.3**		This work
AcS-(L6P)-SAc	3.1	−5.0		52
AcS-(L6P)$_2$-SAc	5.2	−6.9		52
AcS-(L6P)$_3$-SAc	6.8	−6.8		52
NCS-(6T^{seg})$_2$-SCN	4.8	−4.8		33
NCS-(6T^{seg})$_3$-SCN	7	−4.8		33
NCS-12T^{EH}-SCN	4.6	−4.7		8
NCS-16T^{EH}-SCN	6	−4.9		8
NCS-20T^{EH}-SCN	7.4	−5.4		8
NCS-24T^{EH}-SCN	8.8	−5.6		8
NCS-T^{ed}(T^{12}T^{N}T^{12})$_4$T^{ed}-SCN	4.7	−4.9		12
NCS-T^{ed}(T^{12}T^{N}T^{12})$_5$T^{ed}-SCN	5.8	−5.5		12
NCS-T^{ed}(T^{12}T^{N}T^{12})$_6$T^{ed}-SCN	6.4	−5.7		12
OAE5	3	−6.7	MCBJ [b]	53
OAE6	3.7	−6.8		53
OAE7	4.4	−6.9		53
OAE8	5.1	−6.8		53
OAE9	5.8	−6.9		53
ONI4	3.7	−8.0 ~ −9.0	CP-AFM [c]	54
ONI6	5.7	−9.0 ~ −10.0		54
ONI8	7.5	−10.0 ~ −11.0		54

[a]The L value of each structure is estimated via structural optimization at the PM6 level.

[b]MCBJ: Mechanically controllable break junction. [c]CP-AFM: Conductive-prove atomic force microscopy.

2.7 Theoretical calculations

The author performed Landauer-Büttiker probe (LBP) simulations to investigate the origin of the high hopping conductance of **TBID**.[40] The LBP method (details in the Experimental section) describes hopping transport through an artificial probe attached to each hopping site. The parameters in the simulation include the molecular orbital level with respect to the Fermi level (e_a), the transfer integral between the hopping sites (t), the coupling to the left/right electrode $g_{L/R}$, the coupling to the probe g_d, and the transmission coefficient T. Initially, the author determined e_a, t, g_d for **TBID** based on DFT calculations and adjusted $g_{L/R}$ to reproduce the length-dependent conductance values observed experimentally. For simulating **6T^{seg}**, the same $g_{L/R}$ and g_d values from the DFT calculations were adopted. The value of e_a was shifted 0.28 eV towards the higher side, according to the calculated HOMO level. The small injection barrier of the **TBID** unit (the energy difference between the Fermi level and the HOMO) was also

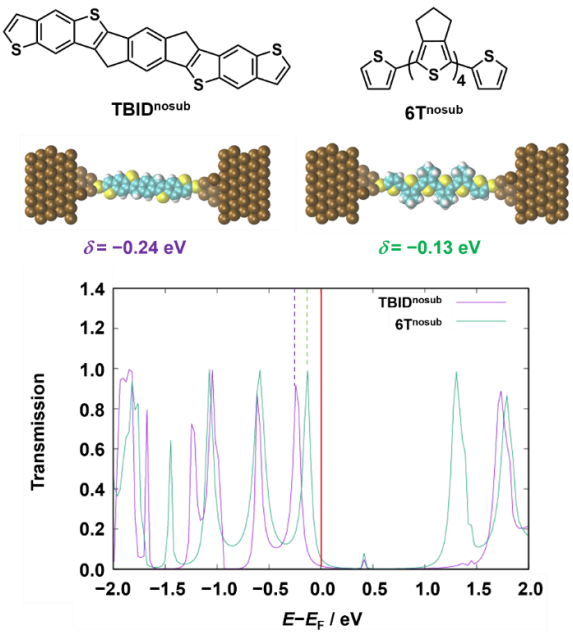

Figure S2-13. Transmission functions were calculated for monomers using the nonequiribrium Green's function method combined with DFT. δ indicates the charge injection barrier (the gap between the Fermi level and HOMO). The molecular structures were simplified by omitting alkyl chains and added S anchors.

confirmed using the non-equilibrium Green's function method combined with DFT (Fig. S2-13). The small energy offset of **6T^{seg}** clearly leads to a higher conductance. This similarity between **TBID** and **6T^{seg}** is observed when the transfer integral (t) from the DFT calculations is considered. To reproduce the lower hopping conductance of **6T^{seg}**, the author had to reduce t and T. The effective t is small, indicating that charge transfer between the hopping sites is inefficient due to thermal fluctuations in the HOMO distributions. The full width at half maximum (fwhm) values for **TBID^{nosub}** (red) and **6T^{nosub}** (blue) are 0.12 and 0.16 eV, respectively, indicating fluctuations at finite temperatures. DFT molecular dynamics simulations showed that the fwhm of the HOMO distribution for **6T^{nosub}** at room temperature is approximately 1.5 times larger than that for TBIDnosub (Figs. 2-5e and S2-14). Thermal fluctuations enhance ΔE_{hs}, thereby increasing E_a. In the LBP model, T is considered a parameter that controls the efficiency of long-range transport, and a small T also implies that coherent tunneling is suppressed due to thermal fluctuations. These results suggest that ΔE_{hs} is reduced for **TBID** due to its rigid structure.

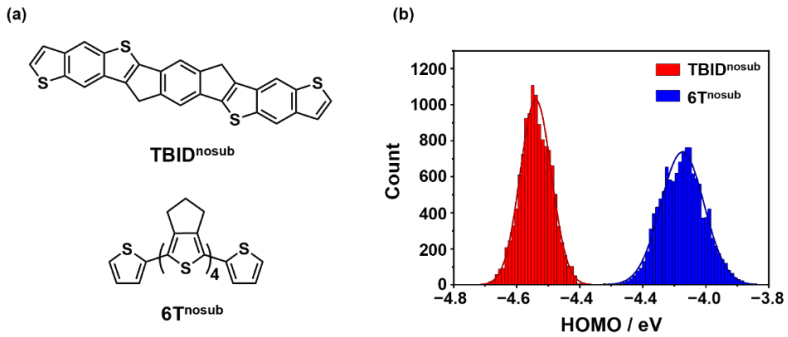

Figure S2-14. Distribution of HOMO energy levels calculated from DFT-MD for **TBID^{nosub}** (red) and **6T^{nosub}** (blue).

2.8 Conclusion

To establish design principles for efficient long-distance intramolecular charge transport based on a hopping mechanism, the author focused on molecular design strategies to decrease both λ of the hopping site and ΔE_{hs} in the molecular wire. Based on these principles, the author designed **TBID** as the hopping site and synthesized **TBID**-repeated oligomers with periodically twisted structures between neighboring **TBID** units. Photophysical and electrochemical measurements revealed that the twisted structures effectively restricted the conjugation of **(TBID)**, aligning the energy levels to those of the **TBID** unit. In single-molecule conductance measurements, **NCS-(TBID)$_n$-SCN** exhibited higher conductance than **NCS-(6T^{seg})$_n$-SCN** with similar molecular lengths. Furthermore, **NCS-(TBID)$_n$-SCN** displayed minimal length-dependent hopping charge transport characteristics. Temperature-dependent conductance measurements revealed that **NCS-(TBID)$_2$-SCN** exhibited a lower E_a than **NCS-(6T^{seg})$_2$-SCN**. Theoretical calculations indicated that smaller λ and ΔE_{hs} for **(TBID)$_n$** are essential to explain the higher conductance despite the smaller energy offset between the HOMO and Fermi energy levels. This study suggests that E_a can be reduced by tuning both λ and ΔE_{hs}, which can be achieved through a combination of fused chemical structures of hopping sites with periodically twisted hopping sites in the conjugated system. This molecular design paves the way for the development of nanometer-scale molecular wires for single-molecule electronics, as well as high-performance semiconducting oligomers/polymers for organic electronics.

2.9 Experimental Section

General Information

Column chromatography was conducted on KANTO Chemical silica gel 60N (40–50 μm). Microwave irradiation was performed using a Biotage Initiator+ 4.2.1. The microwave power output was set to 400 W, and the internal temperature during the reaction was monitored by an IR sensor. Preparative gel permeation chromatography (GPC) was carried out using a Japan Analytical Industry LC-9210 NEXT system equipped with a JAI-GEL 1HH/2HH or JAI-GEL 2.5HH/3HH column. ^{1}H and ^{13}C NMR spectra were recorded on a JEOL JNM-ECS400, JNM-ECA600 and Bruker AVANCE III 700 spectrometer in $CDCl_3$ with tetramethylsilane (TMS) as an internal standard or $C_2D_2Cl_4$. Chemical shifts are reported in ppm (δ), multiplicity (s = singlet, d = doublet, t = triplet, q = quartet, quin = quintet, sept = septet, brs = broad singlet, m = multiplet), coupling constant (Hz), and integration. High-resolution mass spectra (HRMS) were obtained by atmospheric pressure chemical ionization (APCI) or electrospray ionization (ESI) methods using a Thermo Scientific LTQ Orbitrap XL or a MALDI-spiral TOF method by using a JEOL JMS-S3000. All chemicals and reagents were produced from commercial sources (FUJIFILM Wako Chemicals (Tokyo, Japan), TCI (Tokyo, Japan) and Sigma Aldrich (MO, USA)).

Physical property measurements

UV-vis-NIR spectra were recorded on a Shimadzu UV-3600 spectrophotometer. Fluorescence spectra were recorded using a Fluoromax-2 spectrometer in the photon-counting mode equipped with a Hamamatsu R928 photomultiplier. All spectra were obtained in spectrograde solvents. Cyclic voltammetry was carried out on a BAS CV-620C voltammetric analyzer using a platinum disk as the working electrode, platinum wire as the counter electrode, and $Ag/AgNO_3$ as the reference electrode at a scan rate of 100 mV s^{-1}. DPV measurement was conducted in a CH_2Cl_2 solution containing 0.1 M $TBAPF_6$.

Electrical conductance measurements by the break junction method

The STM-BJ measurements were conducted using a PicoSPM (Molecular Imaging) controlled by a PicoScan2500 controller under an Ar atmosphere at room temperature. The sensitivity of the current-to-voltage converter was 10^{-6} A V^{-1}, which limited the largest current and thus the measured conductance. For temperature-dependence measurements, a heating stage provided by Molecular Imaging was utilized. The surface temperature at the heating stage was monitored using a resistive sensor. Gold STM tips were prepared by mechanical cutting of gold wires. Gold substrates were fabricated by thermally evaporating gold onto freshly cleaved mica sheets. During evaporation, the mica sheets were heated at approximately 500 K. Atomically flat Au(111) terraces could be observed on the surface of the gold substrate. The gold substrates were modified with the oligomers by immersing them in a 0.1 μM CH_2Cl_2 solution of the molecules at room temperature for 10 min. After removal from the solution, the substrates were dried by evaporation of the solvent. The peak in the conductance histogram was determined by fitting a Gaussian function.

Tunneling transport calculations

The transport properties of the molecules were calculated using an in-house program that automatically performed structure optimization from a given gas-phase structure using DFT, transport calculations with a nonequilibrium Green's function (NEGF), and post-process analysis. The package utilizes the SMEAGOL code[41-43] and SIESTA package[44]. Single zeta plus polarization (SZP) and double zeta plus polarization (DZP) basis sets were used for Au and other atoms, respectively. The author used the Perdew-Burke-Ernzerhof (PBE) exchange-correlation functional.[45] The electrode was modeled as an Au(111) slab with the p(6×6) periodicity. The k points were sampled using a 2×2×1 uniform grid.

Modeling of hopping transport

The author employed the LBP method[46, 47] to simulate length-dependent conductance, including tunneling and hopping contributions. In the LBP method, a molecular chain is represented by connected hopping sites, and the environmental effects are described using probes attached to each site. The probe has its own chemical potential, which is consistently determined by the voltage gradient applied between the left and right electrodes.

The author considers a one-dimensional tight-binding chain as the Hamiltonian,

$$\hat{H} = \sum_{i=1}^{N} \varepsilon_a \hat{c}_i^{\dagger} \hat{c}_i + \sum_{i=1}^{N-1} t\left(\hat{c}_i^{\dagger} \hat{c}_{i+1} + h.c.\right) \quad \text{(S1)}$$

where ε_a is the site energy of the oligomer unit and τ is the transfer integral. The retarded Green's function is given by

$$\hat{G}^r(\varepsilon) = \left[\hat{I}\varepsilon - \hat{H} + i\hat{\Gamma}/2\right]^{-1} \quad \text{(S2)}$$

where $\hat{\Gamma} = \hat{\Gamma}_L + \hat{\Gamma}_R + \sum_{i=1}^{N} \hat{\Gamma}_i^{\text{probe}}$. The first and N_{th} sites are coupled to the left and right electrodes, respectively. Therefore, the electrode coupling matrices become

$$\left[\hat{\Gamma}_L\right]_{1,1} = \gamma_L, \ \left[\hat{\Gamma}_R\right]_{N,N} = \gamma_R \quad \text{(S3)}$$

where $\gamma_{L,R}$ coupling energy of the electrode. Here, the author assume that $\gamma_{L,R}$ is independent of energy and ignores the energy shifts of molecular orbital due to the coupling with electrodes. The author also assumes that the coupling to the probe is local and independent of the site, which leads to

$$\left[\hat{\Gamma}_i^{\text{probe}}\right]_{i,i} = \gamma_d, \ i = 1,2,\ldots,N \quad \text{(S4)}$$

The transmission coefficients between all the electrodes and probes can be described as

$$\mathcal{T}_{\alpha,\alpha'}(\varepsilon) = \text{Tr}\left[\hat{\Gamma}_\alpha(\varepsilon)\hat{G}^r(\varepsilon)\hat{\Gamma}_{\alpha'}(\varepsilon)\hat{G}^a(\varepsilon)\right], \ \alpha = L,1,2,\ldots,N,R, \quad \text{(S5)}$$

where $\hat{G}^a(\varepsilon) = \left[\hat{G}^r(\varepsilon)\right]^{\dagger}$ is the advanced Green's function.

The chemical potentials of probes, $\{\mu_i\}$, which are given through the Fermi distribution function $f_\alpha(\varepsilon) = [\exp[(\varepsilon - \mu_\alpha)/k_B T] + 1]^{-1}$, where k_B is the Boltzmann constant and T is the temperature, should be determined to guarantee the charge conservation as follows,

$$I_i = \frac{2e}{h}\sum_\alpha \int_{-\infty}^{\infty} d\,\varepsilon \mathcal{T}_{i,\alpha}(\varepsilon)[f_i(\varepsilon) - f_\alpha(\varepsilon)] = 0. \quad \text{(S6)}$$

The author assumes the linear response regime and Taylor-expand the Fermi distribution function as

$$f_\alpha(\varepsilon, \mu_\alpha) = f(\varepsilon, \varepsilon_F) - \frac{\partial f(\varepsilon,\varepsilon_F)}{\partial \varepsilon}(\mu_\alpha - \varepsilon_F). \quad \text{(S7)}$$

Using equation S7, equation S6 can be rewritten as

$$\sum_\alpha \int_{-\infty}^{\infty} d\,\varepsilon \mathcal{T}_{i,\alpha}(\varepsilon)\left(-\frac{\partial f}{\partial \varepsilon}\right)\varepsilon(\mu_i - \mu_\alpha) = 0 \qquad \text{(S8)}$$

where we set $\varepsilon_F = 0$. By solving the above N simultaneous equations, the author obtains the set of probe parameters $\{\mu_i\}$. Finally, the source-drain current can be calculated as

$$I_L = \frac{2e}{h}\sum_\alpha \left[(\mu_L - \mu_\alpha)\int_{-\infty}^{\infty} d\varepsilon \mathcal{T}_{i,\alpha}(\varepsilon)\left(-\frac{\partial f}{\partial \varepsilon}\right)\right]. \qquad \text{(S9)}$$

The author performed the calculations with the bias voltage of 0.1 V and computed the conductance values.

First, the author determined the parameters for **TBID**. $\tau = 003$ eV was obtained from the energies of the HOMO and HOMO-1 of **TBID(Me)**. $\gamma_d = 0.170$ eV was taken from the calculated reorganization energy. The major source of γ_d is considered to be the electron-phonon coupling[48] that has a similar order of value with the reorganization energy.[49] Therefore, the author adopted 0.260 eV for γ_d of **TBID**, taken from the calculated reorganization energy. The author set $\varepsilon_a = -0.41$ eV, which is a typical value for molecular junctions. The other parameters were $\gamma_{L,R} = 0.0002$ eV, and $T = 280$ K, which were adjusted to fit the measured conductance values. As shown in Fig. S12, the LBP method can predict the almost length-dependent conductance of the **TBID** wires. Subsequently, the author determined the parameters for **6T**. The energy level was shifted to 0.28 eV according to the DFT calculated HOMO and set at $\varepsilon_a = -0.13$ eV. The author employed the same $\gamma_{L,R} = 0.0002$ eV and $\gamma_d = 0.260$ eV values obtained from the calculated reorganization energy. To reproduce the experimental results, the author set $\tau = 0.0006$ eV and $T = 140$ K. This indicated that the coupling between the hopping sites is small for **6T**. Note that the 'temperature' of the LBP method can be regarded as a parameter controlling the ballistic component.[50] The fact that a low temperature is required indicates that long-range tunneling transport is suppressed by finite temperature fluctuations in a real system.

Fluctuation of the HOMO levels

The author carried out DFT molecular dynamics (MD) simulations for **TBID^{nosub}** and **6T^{nosub}**, where alkyl chains are omitted for simplification. The author simulated one molecule in a cubic cell whose cell length is 50.0 Å. For the DFT-MD simulation, the author used the BLYP exchange correlation functional together with the Grimme's D3(0) van der Waals correction. The author employed the QUICKSTEP method implemented in the CP2K code.[51] For the Gaussian part of the basis set, the author used the DZVP basis set. The author set the plane wave density cutoff to 320 Ry. The author performed DFT-MD simulation in the NVT ensemble, where the target temperature was set to 300 K with canonical sampling through a velocity rescaling thermostat. The time step for integrating equation of motions was set to 0.4 fs. The author equilibrated the sample for 5 ps and then the author obtained 5 ps DFT-MD trajectory.

Synthesis and characterization

Synthesis of ***BDT-1Br***: **BDT**[55] (1.94 g, 4.35 mmol) was placed in a round-bottomed flask and dissolved in CH_2Cl_2 (50 mL). A solution of Br_2 (0.64 mL, 12.6 mmol) in CH_2Cl_2 (25 mL) was added at 0 °C. After stirring at 0 °C for 2 h, the reaction was quenched by the addition of a $Na_2S_2O_3$ aqueous solution. The resulting mixture was extracted with $CHCl_3$, and the organic layer was washed with water. The residue was purified by column chromatography on silica gel (hexane:toluene = 10:1) to give a tri-brominated product as a colorless oil.

The product was dissolved in anhydrous THF (10 mL). After cooling to −78 ℃ under a nitrogen atmosphere, a solution of *n*-BuLi (2.66 M, 3.60 mL, 9.57 mmol) in hexane was slowly added dropwise to the reaction mixture. The reaction mixture was stirred at −78 °C for 10 min, and then stirred at 0 ℃ for 20 min. The reaction was quenched by the addition of MeOH (2 mL) and then water. The resulting mixture was extracted with $CHCl_3$, and the organic layer was dried over anhydrous sodium sulfate, filtered and then evaporated in vacuo. The product was purified by column chromatography on silica gel (hexane:toluene = 10:1) to give **BDT-1Br** as a colorless oil (960 mg, 1.83 mmol, 42%). ^{1}H NMR (400 MHz, $CDCl_3$, δ): 0.93 (t, J = 7.2 Hz, 6H), 0.99-1.03 (m, 6H), 1.36-1.53 (m, 9H), 1.56-1.80 (m, 8H), 2.05 (sept, J = 6.2 Hz, 1H), 4.10 (d, J = 6.8 Hz, 2H), 4.16 (d, J = 5.6 Hz, 2H), 7.35 (s, 1H), 7.43 (d, J = 5.6 Hz, 1H), 7.46 (d, J = 5.2 Hz, 1H); ^{13}C NMR (100 MHz, $CDCl_3$, δ): 145.0, 144.7, 133.0, 131.8, 129.8, 127.6, 127.3, 124.9, 120.2, 103.3, 78.7, 76.6, 40.8, 40.4, 30.5, 30.3, 29.3, 29.2, 23.9, 23.8, 23.3, 23.2, 14.3, 11.4, 11.3; HRMS (ESI) m/z: $[M+H]^+$ calcd. for $C_{26}H_{38}BrO_2S_2$, 525.1491; found, 525.1499.

Synthesis of ***BDT-Oct***: In a two-necked round-bottom flask, **BDT-1Br** (960 mg, 1.82 mmol) and $NiCl_2$(dppp) (49 mg, 0.091 mmol) were dissolved in Et_2O (20 mL) under a nitrogen atmosphere. After adding a solution of C_8H_{17}-MgBr (2.0 M, 9.1 mL, 18.2 mmol) in Et_2O to the reaction mixture at 0 ℃, the reaction mixture was refluxed overnight. After cooling to room temperature, the reaction was quenched with 1N HCl aqueous solution. The resulting mixture was filtered through a Celite bed, and the filtrate was extracted with hexane. The combined organic layer was concentrated under reduced pressure, and then the resulting residue was purified by column chromatography on silica gel (hexane:toluene = 10:1) to give **BDT-Oct** as a yellow oil (865 mg, 1.55 mmol, 85%). ^{1}H NMR (400 MHz, $CDCl_3$, TMS, δ): 0.88 (t, J = 7 Hz, 4H), 0.92-0.95 (m, 6H), 1.01 (t, J = 7.2 Hz, 6H), 1.27-1.40 (m, 22H), 1.56-1.69 (m, 2H), 1.71-1.82 (m, 3H), 1.93-1.97 (m, 1H), 3.03 (t, J = 7.6 Hz, 2H), 4.02-4.09 (m, 2H), 4.14 (d, J = 6.4 Hz, 2H), 6.96 (s, 1H), 7.36 (d, J = 5.6 Hz, 2H), 7.45 (d, J = 5.6 Hz, 2H); ^{13}C NMR (100 MHz, $CDCl_3$, δ): 154.8, 144.9, 137.4, 131.8, 131.2, 131.0, 130.7, 125.9, 121.0, 120.3, 77.3, 76.2, 40.9, 40.7, 32.1, 31.8, 30.9, 30.6, 30.5, 30.1, 29.9, 29.8, 29.6, 29.4, 24.0, 23.8, 23.3, 23.3, 22.9, 14.3, 14.3, 11.5, 11.4; HRMS (ESI) m/z: $[M+H]^+$ calcd. for $C_{34}H_{55}O_2S_2$, 559.3640; found, 559.3630.

Synthesis of ***b-C8-BDT-Sn***: **BDT-Oct** (560 mg, 1.00 mmol) was dissolved in anhydrous THF (10 mL) and cooled to −78 ℃ under a nitrogen atmosphere. A solution of Me_3SnCl (1.0 M, 0.5 mL, 2.00 mmol) in hexane was added dropwise to the reaction mixture. Then, a solution of LDA (1.0 M, 1.4 mL, 1.40 mmol) in THF was added to the reaction mixture. The mixture was stirred at −78 °C for 1 h and then stirred at room temperature for 16 h. The reaction was quenched with the addition of water (10 mL). The resulting mixture was extracted with $CHCl_3$, and the organic layer was dried over anhydrous sodium sulfate, filtered and evaporated in vacuo. Column

chromatography was performed on alumina gel (hexane:$CHCl_3$ = 1:5). Further purification was conducted by recycling GPC (JAI-GEL 1HH/2HH, $CHCl_3$ as an eluent) to obtain ***b*-C8-BDT-Sn** as a yellow oil (850 mg, 1.00 mmol, quant.). ^{1}H NMR (400 MHz, $CDCl_3$, δ): 0.87-0.95 (m, 24H), 1.00-1.04 (m, 6H), 1.16-1.20 (m, 6H), 1.25-1.42 (m, 22H), 1.51-1.56 (m, 2H), 1.61-1.78 (m, 15H), 1.95 (sept, J = 6.1 Hz, 1H), 3.02 (t, J = 7.6 Hz, 2H), 4.09 (dd, J = 6.4, 2.4 Hz, 2H), 4.14 (d, J = 5.0 Hz, 2H), 6.93 (s, 1H), 7.48 (s, 1H); HRMS (APCI) m/z: $[M+H]^+$ calcd. for $C_{46}H_{81}O_2S_2Sn$, 849.4690; found, 849.4705.

*Synthesis of **1***: ***b*-C8-BDT-Sn** (550 mg, 0.65 mmol), diethyl 2,5-dibromoterephthalate (112 mg, 0.30 mmol), and $Pd(PPh_3)_4$ (34 mg, 0.030 mmol) were placed in a test tube with a screw cap and dissolved in toluene (4 mL). After refluxing for overnight, the reaction mixture was concentrated under reduced pressure. The residue was purified by column chromatography on silica gel (hexane:EtOAc = 10:1) to give **1** as a yellow solid (394 mg, 0.30 mmol, quant.). ^{1}H NMR (400 MHz, $CDCl_3$, TMS, δ): 0.88-1.04 (m, 36H), 1.29-1.54 (m, 42H), 1.59-1.84 (m, 14H), 1.97 (sept, J = 6.1 Hz, 2H), 2.62 (s, 6H), 3.03-3.06 (m, 4H), 4.05-4.13 (m, 4H), 4.20 (d, J = 4.1 Hz, 4H), 7.05 (s, 2H), 7.66 (s, 2H), 8.38 (s, 2H); ^{13}C NMR (100 MHz, $CDCl_3$, δ): 148.2, 145.6, 145.5, 137.7, 136.4, 133.1, 132.5, 131.8, 131.0, 126.8, 122.1, 121.9, 77.6, 42.1, 40.8, 40.7, 32.1, 30.8, 30.5, 30.5, 30.2, 29.8, 29.8, 29.5, 29.4, 29.3, 24.0, 23.9, 23.8, 23.8, 23.2, 22.8, 14.3, 14.3, 11.5, 11.4, 11.4; HRMS (APCI) m/z: $[M+H]^+$ calcd. for $C_{80}H_{119}O_8S_4$, 1335.7782; found, 1335.7792.

*Synthesis of **TBID***: 4-Hexylbromobenzene (674 mg, 2.79 mmol) was dissolved in anhydrous THF (2 mL), and the solution was cooled to −78 °C. A solution of *n*-BuLi (2.64 M, 1.06 mL, 2.79 mmol) in hexane was added dropwise under a nitrogen atmosphere. After stirring for 1 h, a solution of **1** (304 mg, 0.21 mmol) in THF was added dropwise to the reaction mixture. The mixture was kept at −78 °C for 1 h and then stirred at room temperature for 12 h. The reaction was quenched with water (10 mL) and extracted with $CHCl_3$. The combined organic layer was dried with anhydrous sodium sulfate and evaporated in vacuo.

Then, AcOH (5 mL) and sulfuric acid were added, and the reaction mixture was refluxed for 2 h. After the addition of water (20 mL) at room temperature, the reaction mixture was extracted with $CHCl_3$ for three times. The combined organic layer was dried with anhydrous sodium sulfate and evaporated in vacuo. Column chromatography was performed on silica gel (hexane:AcOEt = 10:1). Further purification was conducted by recycling GPC (JAI-GEL 1HH/2HH, $CHCl_3$ as an eluent) to give **TBID** as a yellow oil (326 mg, 0.18 mmol, 84%). ^{1}H NMR (400 MHz, $CDCl_3$, TMS, δ): 0.78-0.96 (m, 36H), 1.02 (t, J = 7.6 Hz, 6H), 1.16-1.40 (m, 76H), 1.57-1.74 (m, 14H), 1.97 (sept, J = 6.1 Hz, 2H), 2.53 (t, J = 9.6 Hz 8H), 2.78-2.99 (m, 4H), 3.49 (d, J = 5.6 Hz, 4H), 3.99-4.01 (m, 4H), 6.89 (s, 2H), 7.02 (d, J = 8.0 Hz, 8H) 7.30 (s, 2H), 7.37-7.40 (m, 8H); ^{13}C NMR (100 MHz, $CDCl_3$, δ): 157.6, 148.9, 147.4, 145.7, 145.5, 144.9, 142.7, 141.2, 139.3, 137.2, 136.0, 135.6, 135.4, 131.8, 130.7, 129.1, 127.9, 127.0, 126.9, 120.6, 116.6, 64.8, 40.6, 40.5, 39.2, 35.7, 32.1, 31.9, 31.4, 31.3, 29.8, 29.8, 29.6, 29.5, 23.9, 23.6, 23.3, 22.8, 22.7, 14.4, 14.4, 14.3, 14.0, 11.5, 10.8; HRMS (APCI) m/z: $[M+H]^+$ calcd. for $C_{124}H_{175}O_4S_4$, 1856.2368; found, 1856.2388.

*Synthesis of **TBID-Br***: NBS (22 mg, 0.12 mmol) was added to a solution of **TBID** (105 mg, 0.057 mmol) in $CHCl_3$ at 0 °C. After stirring at 0 °C for 2 h, the reaction mixture was quenched by the addition of a $Na_2S_2O_3$ aqueous

solution. The resulting mixture was extracted with $CHCl_3$, and the organic layer was washed with water. The residue was purified by column chromatography on silica gel (hexane:$CHCl_3$ = 5:1) to give **TBID-Br** as a yellow oil (105 mg, 0.052 mmol, 92%). ^{1}H NMR (400 MHz, $C_2D_2Cl_4$, δ): 0.79-0.95 (m, 36H), 1.02 (t, J = 7.6 Hz, 6H), 1.16-1.61 (m, 86H), 1.67-1.71 (m, 4H), 1.98 (sept, J = 6.1 Hz, 2H), 2.55 (t, J = 7.8 Hz, 8H), 2.92 (brs, 4H), 3.44 (brs, 4H), 3.99-4.06 (m, 4H), 7.05 (d, J = 8.2 Hz, 8H), 7.33 (s, 2H), 7.36 (d, J = 7.2 Hz, 8H); ^{13}C NMR (150 MHz, $CDCl_3$, δ): 157.6, 148.8, 144.8, 144.5, 143.0, 139.1, 136.0, 130.6, 129.1, 129.0, 126.9, 116.7, 116.6, 112.1, 64.8, 40.5, 39.1, 35.7, 31.8, 29.4, 23.3, 22.8, 22.7, 14.3, 14.3, 14.2, 14.2, 11.4, 10.8; HRMS (APCI) m/z: $[M+H]^+$ calcd. for $C_{124}H_{173}Br_2O_4S_4$, 2012.0578; found, 2012.0607.

Synthesis of ***(TBID)$_2$*** and ***(TBID)$_3$***: **TBID-Br** (98 mg, 0.049 mmol), $(SnMe_3)_2$ (16 mg, 0.049 mmol), $Pd(PPh_3)_4$ (5.6 mg, 0.0049 mmol), and toluene (4 mL) were placed in a microwave proof walled glass vial equipped with a snap cap. The glass vial was purged with nitrogen, securely sealed, and heated in a microwave reactor with keeping the temperature at 180 ºC for 20 min. After cooling to room temperature, the mixture was concentrated under reduced pressure, and then the residue was purified by column chromatography on silica gel (hexane:$CHCl_3$ = 5:1).

A solution of TBAF (1.0 M, 5 mL, 5 mmol) in THF was added, and the reaction mixture was refluxed for 1 h. Then, an NH_4Cl aqueous solution (20 mL) and Et_2O (20 mL) were added to the reaction mixture, and the mixture was extracted with Et_2O for three times. The combined organic layer was dried with anhydrous sodium sulfate and evaporated in vacuo.

Anhydrous THF (5 mL) was added to the residue, and the solution was cooled to −78 ℃. A solution of *n*-BuLi (1.59 M, 8.3 mL, 13.2 mmol) in hexane was added dropwise under a nitrogen atmosphere. After stirring for 1 h, MeOH (2 mL) was added dropwise. The reaction mixture was kept at −78 ℃ for 1 h and then stirred at room temperature for 1 h. The resulting reaction was quenched with water (10 mL) and extracted with $CHCl_3$. The organic layer was dried with anhydrous sodium sulfate and evaporated in vacuo. Column chromatography was performed on silica gel (hexane:AcOEt = 10:1). Then, recycling GPC (JAIGEL 2.5HH/3HH, $CHCl_3$ as an eluent) was performed to obtain **(TBID)$_2$** (22 mg, 0.0059 mmol, 12%) and **(TBID)$_3$** (17 mg, 0.0031 mmol, 6%).

(TBID)$_2$: Yellow solid; ^{1}H NMR (400 MHz, $CDCl_3$, δ): 1.04-0.75 (m, 82H), 1.39-1.14 (m, 167H), 1.68 (q, J = 7.9 Hz, 8H), 1.94-2.02 (m, 4H), 2.53 (t, J = 7.8 Hz, 22H), 2.79 (s, 6H), 2.97 (t, J = 7.6 Hz, 2H), 3.50 (brs, 8H), 4.01 (brs, 8H), 6.89 (s, 2H), 7.03 (d, J = 8.2 Hz, 16H), 7.30-7.32 (m, 4H), 7.39 (d, J = 7.3 Hz, 16H); ^{13}C NMR (175 MHz, $CDCl_3$, δ): 157.6, 148.9, 145.7, 145.7, 145.5, 144.8, 143.0, 141.3, 139.3, 137.2, 137.1, 135.8, 135.6, 135.6, 135.5, 135.4, 131.1, 130.8, 130.7, 129.1, 128.7, 128.1, 127.9, 127.2, 116.6, 75.9, 75.7, 65.5, 64.8, 42.1, 40.6, 40.5, 39.2, 35.8, 32.1, 32.1, 32.0, 31.9, 31.8, 31.4, 31.3, 30.6, 30.4, 30.4, 30.2, 30.2, 30.1, 30.0, 29.9, 29.8, 29.8, 29.6, 29.6, 29.5, 29.5, 29.4, 29.3. 29.3, 29.3, 28.7, 23.9, 23.6, 23.5, 23.5, 23.3, 23.3, 23.3, 22.8, 22.7, 22.7, 14.4, 14.3, 14.3, 14.3, 14.0, 11.5, 11.5, 11.3, 10.8, 10.7; MS (MALDI-spiralTOF) m/z: $[M+H]^+$ calcd. for $C_{248}H_{346}O_8S_8$, 3708.43; found, 3708.98.

(TBID)$_3$: Yellow solid; ^{1}H NMR (600 MHz, $CDCl_3$, δ): 0.74-0.94 (m, 172H), 1.00-1.03 (m, 15H), 1.11-1.17 (m, 26H), 1.25-1.38 (m, 133H), 1.66-1.74 (m, 8H), 1.98-2.01 (m, 8H), 2.53 (t, J = 7.2 Hz, 32H), 2.79 (s, 12H), 2.97 (t, J = 7.2 Hz, 4H), 3.49 (brs, 16H), 4.01 (brs, 16H), 6.89 (brs, 2H), 7.02-7.04 (m, 32H), 7.29-7.32 (m, 10H), 7.38-7.40 (m, 32H); ^{13}C NMR (175 MHz, $CDCl_3$, δ): 157.7, 145.7, 144.8, 141.3, 139.2, 137.1, 135.8, 131.7, 131.1, 129.1,

128.7, 128.1, 127.9, 78.4, 75.8, 65.5, 64.8, 42.1, 40.5, 39.2, 35.7, 32.1, 31.8, 31.7, 31.4, 31.3, 30.6, 30.4, 30.3, 30.1, 29.9, 29.8, 29.8, 29.6, 29.5, 29.5, 29.4, 29.3, 29.3, 29.3, 28.7, 23.9, 23.6, 23.5, 23.5, 23.3, 23.3, 22.8, 22.7, 22.7, 14.3, 14.3, 14.2, 11.5, 11.5, 11.3, 10.8, 10.8.

Synthesis of ***NCS-TBID-SCN***: Potassium thiocyanate (29 mg, 0.30 mmol) was dissolved in CH_2Cl_2 (0.4 mL) and MeOH (0.6 mL) and then cooled to 0 ℃ under a nitrogen atmosphere. A solution of Br_2 (1.5 M, 0.1 mL, 0.15 mmol) in MeOH was added dropwise to the reaction mixture. After stirring for 1 h, a solution of **TBID** (27 mg, 0.015 mmol) in THF was added dropwise to the reaction mixture. The mixture was kept at 0 ℃ for 1 h and then stirred at room temperature for 4 h. The reaction was quenched with water (10 mL), and the resulting mixture was extracted with $CHCl_3$. The organic layer was extracted and dried with anhydrous sodium sulfate. After evaporation of the solvent, column chromatography was performed on silica gel (hexane:$CHCl_3$ = 1:5). Further purification was performed by recycling GPC (JAIGEL 2.5HH/3HH, $CHCl_3$ as an eluent) to give **NCS-TBID-SCN** as a yellow solid (15 mg, 0.0076 mmol, 51%). ^{1}H NMR (400 MHz, $CDCl_3$, δ): 0.80-0.97 (m, 42H), 1.03 (t, J = 7.3 Hz, 6H), 1.18-1.40 (m, 76H), 1.59-1.70 (m, 8H), 1.99 (sept, J = 6.3 Hz, 2H), 2.54 (t, J = 8.0 Hz, 8H), 3.11 (t, J = 7.8 Hz, 4H), 3.45 (d, J = 4.6 Hz, 4H), 4.00-4.03 (m, 4H), 7.04 (d, J = 8.2 Hz, 8H), 7.33 (s, 2H), 7.36 (dd, J = 8.2, 2.7 Hz, 8H); ^{13}C NMR (150 MHz, $CDCl_3$, δ):167.9, 157.9, 157.7, 149.2, 148.9, 148.6, 146.3, 144.8, 144.5, 144.4, 141.8, 141.4, 139.2, 139.1, 139.0, 136.2, 136.0, 135.8, 135.0, 132.6, 132.2, 131.0, 130.6, 129.0, 128.7, 128.0, 126.9, 116.9, 116.7, 137.7, 113.6, 112.3, 110.0, 68.3, 64.9, 64.8, 64.4, 40.6, 40.5, 39.9, 39.2, 39.2, +35.7, 32.1, 32.0, 31.9, 31.4, 31.0, 30.7, 30.5, 30.4, 30.3, 30.0, 29.8, 29.8, 29.7, 29.5, 29.4, 29.4, 29.3, 29.1, 28.8, 24.0, 23.9, 23.5, 23.3, 23.1, 22.8, 22.7, 22.5, 15.4, 15.1, 14.4, 14.3, 14.2, 13.9, 11.4, 11.3, 11.1, 10.9; HRMS (APCI) m/z: $[M+H]^+$ calcd. for $C_{126}H_{173}N_2O_4S_6$, 1970.1714; found, 1970.1711.

The same procedure was used for the synthesis of **NCS-(TBID)$_2$-SCN** (16 mg, 63%) and **NCS-(TBID)$_3$-SCN** (1.2 mg, 10%).

NCS-(TBID)$_2$-SCN: Yellow solid; ^{1}H NMR (400 MHz, $CDCl_3$, δ): 0.90-1.02 (m, 82H), 1.17-1.28 (brs, 124H), 1.56 (brs, 64H), 1.99 (brs, 2H), 2.53 (brs, 24H), 2.77-2.96 (m, 2H), 3.11 (brs, 2H), 3.45 (brs, 4H), 4.01 (brs, 4H), 7.05 (brs, 16H), 7.37-7.56 (m, 20H); ^{13}C NMR (150 MHz, $CDCl_3$, δ): 171.6, 157.8, 157.6, 152.9, 148.4, 146.4, 146.3, 146.2, 145.7, 144.8, 144.8, 142.3, 141.3, 139.1, 139.0, 138.8, 136.3, 136.0, 135.8, 132.2, 132.2, 132.0, 131.7, 131.6, 131.6, 131.1, 130.1, 129.1, 128.7, 128.0, 128.0, 126.2, 126.1, 126.0, 120.5, 120.4, 120.3, 116.7, 116.0, 113.0, 110.1, 110.0, 109.9, 78.6, 78.3, 76.4, 76.2, 76.1, 75.8, 64.8, 64.5, 40.8, 40.6, 40.5, 39.6, 39.2, 39.1, 38.0, 37.3, 37.3, 36.9, 35.7, 33.9, 33.6, 32.9, 32.1, 32.0, 31.9, 31.7, 31.4, 31.3, 31.1, 30.6, 30.4, 30.2, 30.1, 29.9, 29.8, 29.8, 29.7, 29.5, 29.4, 29.3, 28.8, 27.7, 27.4, 27.3, 27.1, 26.7, 24.0, 23.9, 23.5, 23.5, 23.3, 22.8, 22.7, 22.4, 18.9, 15.0, 14.4, 14.3, 14.2, 13.8, 11.5, 10.9, 10.8; MS (MALDI-spiralTOF) m/z: $[M+H]^+$ calcd. for $C_{250}H_{344}N_2O_8S_{10}$, 3822.37; found, 3821.86.

NCS-(TBID)$_3$-SCN: Yellow solid; ^{1}H NMR (400 MHz, $CDCl_3$, δ): 0.75-0.94 (m, 120H), 1.01-1.03 (m, 6H), 1.14-1.38 (m, 194H), 1.55 (brs, 86H), 1.98 (brs, 4H), 2.53 (brs, 24H), 2.79-3.11 (brs, 12H), 3.34-3.49 (m, 8H), 4.01 (brs, 8H), 7.04 (brs, 24H), 7.31-7.45 (m, 30H); ^{13}C NMR (150 MHz, $CDCl_3$, δ): 183.8, 169.5, 144.5, 129.0, 128.0, 126.2, 119.9, 103.6, 99.1, 88.9, 85.4, 73.8, 64.6, 63.8, 57.6, 38.8, 38.5, 35.7, 32.0, 31.8, 31.3, 30.3, 30.1, 29.8, 29.6, 29.4, 29.2, 28.7, 25.8, 25.3, 25.2, 23.8, 23.5, 23.2, 22.8, 22.7, 21.9, 14.2, 11.4, 10.8, 10.2.*Synthesis of* ***S2***: Potassium

hydroxide (4.90 g, 87.3 mmol) was added to a solution of **S1** (1.23 g, 3.49 mmol) in H_2O (16 mL) and ethylene glycol (32 mL) and refluxed for 2 days. The precipitate was extracted with EtOAc and dried over $MgSO_4$. The solvent was removed under reduced pressure to give **S2** as a white solid (1.20 g, 88%). ^{1}H NMR (400 MHz, DMSO-d_6, TMS): δ 0.80-0.90 (m, 12H), 1.14-1.34 (m, 12H), 1.47-1.57 (m, 2H), 2.52-2.60 (m, 4H), 7.40 (s, 2H), 12.95 (s, 2H).

Computational Details

All calculations were conducted using Gaussian 09 program[56]. The geometry was optimized with the unrestricted Becke Hybrid (UB3LYP) at 6-31G(d,p) level. The time-dependent density functional theory (TD-DFT) calculation was conducted at the CAM-B3LYP/6-31G(d,p) level of theory.

2.10 References

1. Cui, X. P.; Xiao, C. Y.; Winands, T.; Koch, T.; Li, Y.; Zhang, L.; Doltsinis, N. L.; Wang, Z. H. Hexacene Diimides. *J. Am. Chem. Soc.* **2018**, *140*, 12175-12180.
2. Duan, Y. X.; Chen, M.; Hayashi, H.; Yamada, H.; Liu, X. Y.; Zhang, L. *Chem. Sci.* **2023**, *14*, 10420-10428.
3. Umeyama, T.; Igarashi, K.; Sasada, D.; Tamai, Y.; Ishida, K.; Koganezawa, T.; Ohtani, S.; Tanaka, K.; Ohkita, H.; Imahori, H. *Chem. Sci.* **2020**, *11*, 3250-3257.
4. Kiguchi, M. In *Single-Molecule Electronics: An Introduction to Synthesis, Measurement and Theory*; Springer: Singapore, 2016.
5. Ogawa, T. In *Molecular Architectonics: The Third Stage of Single Molecule Electronics*; Springer: Singapore, 2017.
6. Choi, S. H.; Frisbie, C. D. *J. Am. Chem. Soc.* **2010**, *132*, 16191-16201.
7. Choi, S. H.; Kim, B.; Frisbie, C. D. *Science* **2008**, *320*, 1482-1486.
8. Ie, Y.; Okamoto, Y.; Inoue, T.; Tone, S.; Seo, T.; Honda, Y.; Tanaka, S.; Lee, S. K.; Ohto, T.; Yamada, R.; Tada, H.; Aso, Y. *J. Phys. Chem. Lett.* **2019**, *10*, 3197-3204.
9. Lu, Q.; Liu, K.; Zhang, H. M.; Du, Z. B.; Wang, X. H.; Wang, F. S. *ACS Nano* **2009**, *3*, 3861-3868.
10. Luo, L.; Frisbie, C. D. *J. Am. Chem. Soc.* **2010**, *132*, 8854-8855.
11. Yamada, R.; Kumazawa, H.; Noutoshi, T.; Tanaka, S.; Tada, H. *Nano Lett.* **2008**, *8*, 1237-1240.
12. Yamada, R.; Kumazawa, H.; Tanaka, S.; Tada, H. *Appl. Phys. Exp.* **2009**, *2*, 025002.
13. Díez-Pérez, I.; Hihath, J.; Lee, Y.; Yu, L. P.; Adamska, L.; Kozhushner, M. A.; Oleynik, II; Tao, N. J. *Nat. Chem.* **2009**, *1*, 635-641.
14. Aradhya, S. V.; Venkataraman, L. *Nat. Nanotech.* **2013**, *8*, 399-410.
15. Metzger, R. M. Unimolecular Electronics. *Chem. Rev.* **2015**, *115*, 5056-5115.
16. Su, T. A.; Neupane, M.; Steigerwald, M. L.; Venkataraman, L.; Nuckolls, C. *Nat. Rev. Mater.* **2016**, *1*,16602.
17. Sun, L.; Diaz-Fernandez, Y. A.; Gschneidtner, T. A.; Westerlund, F.; Lara-Avila, S.; Moth-Poulsen, K. *Chem. Soc. Rev.* **2014**, *43*, 7378-7411.
18. Xiang, D.; Wang, X. L.; Jia, C. C.; Lee, T.; Guo, X. F. *Chem. Rev.* **2016**, *116*, 4318-4440.

19. Kocherzhenko, A. A.; Grozema, F. C.; Vyrko, S. A.; Poklonski, N. A.; Siebbeles, L. D. A. *J. Phys. Chem. C* **2010**, *114*, 20424-20430. DOI: 10.1021/jp104673h.
20. Segal, D.; Nitzan, A.; Ratner, M.; Davis, W. B. Activated Conduction in Microscopic Molecular Junctions. *J. Phys. Chem. B* **2000**, *104*, 2790-2793.
21. Berlin, Y. A.; Hutchison, G. R.; Rempala, P.; Ratner, M. A.; Michl, J. *J. Phys. Chem. A* **2003**, *107*, 3970-3980.
22. Bixon, M.; Jortner, J. *J. Am. Chem. Soc.* **2001**, *123*, 12556-12567.
23. Segal, D.; Nitzan, A.; Davis, W. B.; Wasielewski, M. R.; Ratner, M. A. *J. Phys. Chem. B* **2000**, *104*, 3817-3829.
24. Asakawa, R.; Seo, T.; Yokoyama, S.; Ie, Y. *Polym. J.* **2023**, *55*, 451-461.
25. Brückner, C.; Engels, B. *J. Comput. Chem.* **2016**, *37*, 1335-1344.
26. Geng, H.; Niu, Y. L.; Peng, Q.; Shuai, Z. G.; Coropceanu, V.; Brédas, J. L. *J. Chem. Phys.* **2011**, *135*, 104703.
27. Shi, Y. A.; Chang, Y. L.; Lu, K.; Chen, Z. H.; Zhang, J. Q.; Yan, Y. J.; Qiu, D. D.; Liu, Y. A.; Adil, M. A.; Ma, W.; Hao, X.; Zhu, L.; Wei, Z. *Nat. Commun.* **2022**, *13*, 3256-3263.
28. Xu, T.; Wang, W. L.; Yin, S. W. *J. Phys. Chem. A* **2018**, *122*, 8957-8964.
29. Zade, S. S.; Bendikov, M. *Chem. Eur. J.* **2008**, *14*, 6734-6741.
30. Sedghi, G.; Esdaile, L. J.; Anderson, H. L.; Martin, S.; Bethell, D.; Higgins, S. J.; Nichols, R. J. *Adv. Mater.* **2012**, *24*, 653-657.
31. Sukegawa, J.; Schubert, C.; Zhu, X. Z.; Tsuji, H.; Guldi, D. M.; Nakamura, E. *Nat. Chem.* **2014**, *6*, 899-905.
32. Terao, J.; Wadahama, A.; Matono, A.; Tada, T.; Watanabe, S.; Seki, S.; Fujihara, T.; Tsuji, Y. *Nat. Commun.* **2013**, *4*, 1691.
33. Ie, Y.; Okamoto, Y.; Inoue, T.; Seo, T.; Ohto, T.; Yamada, R.; Tada, H.; Aso, Y. *J. Am. Chem. Soc.* **2021**, *143*, 599-603.
34. Ie, Y.; Han, A. H.; Otsubo, T.; Aso, Y. *Chem. Commun.* **2009**, 3020-3022.
35. Ie, Y.; Endou, M.; Lee, S. K.; Yamada, R.; Tada, H.; Aso, Y. *Angew. Chem. Int. Ed.* **2011**, *50*, 11980-11984.
36. Wu, S. M.; González, M. T.; Huber, R.; Grunder, S.; Mayor, M.; Schönenberger, C.; Calame, M. *Nat. Nanotech.* **2008**, *3*, 569-574.
37. Sugiyasu, K.; Honsho, Y.; Harrison, R. M.; Sato, A.; Yasuda, T.; Seki, S.; Takeuchi, M. *J. Am. Chem. Soc.* **2010**, *132*, 14754-14756.
38. Xu, B. Q.; Tao, N. J. J. Measurement of Single-Molecule Resistance by Repeated Formation of Molecular Junctions. Science **2003**, *301*, 1221-1223.
39. Hines, T.; Diez-Perez, I.; Hihath, J.; Liu, H. M.; Wang, Z. S.; Zhao, J. W.; Zhou, G.; Muellen, K.; Tao, N. J. *J. Am. Chem. Soc.* **2010**, *132*, 11658-11664.
40. Jang, J.; Jo, J. W.; Ohto, T.; Yoon, H. J. Seebeck Effect in Molecular Wires Facilitating Long-Range Transport. *J. Am. Chem. Soc.* **2024**, *146*, 4922-4929.
41. Rocha, A. R.; García-Suárez, V. M.; Bailey, S.; Lambert, C.; Ferrer, J.; Sanvito, S. *Phys. Rev. B* **2006**, 73 085414.
42. Rungger, I.; Sanvito, S. *Phys. Rev. B* **2008**, *78* 035407.
43. Ohto, T.; Rungger, I.; Yamashita, K.; Nakamura, H.; Sanvito, S. *Phys. Rev. B* **2013**, *87*, 205439.

44. Soler, J. M.; Artacho, E.; Gale, J. D.; Garcia, A.; Junquera, J.; Ordejon, P.; Sanchez-Portal, D. *J. Phys. Condens. Matter*. **2002**, *14*, 2745-2779.
45. Perdew, J. P.; Burke, K.; Ernzerhof, M. *Phys. Rev. Lett.* **1996**, *77*, 3865-3868.
46. Park, S.; Jo, J. W.; Jang, J.; Ohto, T.; Tada, H.; Yoon, H. J. *Nano Lett.* **2022**, *22*, 7682-7689.
47. Jang, J.; Jo, J. W.; Ohto, T.; Yoon, H. J. *J. Am. Chem. Soc.* **2024**, *146*, 4922-4929.
48. Li, Y. Q.; Xiang, L. M.; Palma, J. L.; Asai, Y.; Tao, N. J. *Nat. Commun.* **2016**, *7*, 11294.
49. Hsu, C. P. *Phys. Chem. Chem. Phys.* **2020**, *22*, 21630-21641.
50. Korol, R.; Kilgour, M.; Segal, D. *J. Chem. Phys.* **2016**, *145*, 224702.
51. Kühne, T. D.; Iannuzzi, M.; Del Ben, M.; Rybkin, V. V.; Seewald, P.; Stein, F.; Laino, T.; Khaliullin, R. Z.; Sch・t, O.; Schiffmann, F.; *et al. J. Chem. Phys.* **2020**, *152*, 194193.
52. Hines, T.; Diez-Perez, I.; Hihath, J.; Liu, H.; Wang, Z.; Zhao, J.; Zhou, G.; Muellen, K.; Tao, N. *J. Am. Chem. Soc.* **2010**, *132*, 11658-11664.
53. Zhao, X.; Huang, C.; Gulcur, M.; Batsanov, A.; Baghernejad, M.; Hong, W.; Bryce, M.; Wandlowski, T. *Chem. Mater.* **2013**; *25*, 4340-4347.
54. Choi, S.; Risko, C.; Delgado, M.; Kim, B.; Brédas, J.; Frisbie, C. *J. Am. Chem. Soc.* **2010**, *132*, 4358-4368.
55. Doumon, N. Y., Wang, G., Chiechi, R. C. & Koster, L. J. A. *J. Mater. Chem. C* **2017**, ***5***, 6611-6619.
56. Gaussian 09, Revision D.01, Frisch, M. J.; Trucks, G. W.; Schlegel, H. B.; Scuseria, G. E.; Robb, M. A.; Cheeseman, J. R.; Scalmani, G.; Barone, V.; Mennucci, G. A. P.; Nakatsuji, H.; Caricato, M.; Li, X.; Hratchian, H. P.; Izmaylov, A. F.; Bloino, J.; Zheng, G.; Sonnenberg, J. L.; Hada, M.; Ehara, M.; Toyota, K.; Fukuda, R.; Hasegawa, J.; Ishida, M.; Nakajima, T.; Honda, Y.; Kitao, O.; Nakai, H.; Vreven, T.; Montgomery, J. A.; Peralta, J. E.; Ogliaro, F.; Bearpark, M.; Heyd, J. J.; Brothers, E.; Kudin, K. N.; Staroverov, V. N.; Keith, T.; Kobayashi, R.; Normand, J.; Raghavachari, K.; Rendell, A.; Burant, J. C.; Iyengar, S. S.; Tomasi, J.; Cossi, M.; Rega, N.; Millam, J. M.; Klene, M.; Knox, J. E.; Cross, J. B.; Bakken, V.; Adamo, C.; Jaramillo, J.; Gomperts, R.; Stratmann, R. E.; Yazyev, O.; Austin, A. J.; Cammi, R.; Pomelli, C.; Ochterski, J. W.; Martin, R. L.; Morokuma, K.; Zakrzewski, V. G.; Voth, G. A.; Salvador, P.; Dannenberg, J. J.; Dapprich, S.; Daniels, A. D.; Farkas, O.; Foresman, J. B.; Ortiz, J. V.; Cioslowski, J.; Fox, D. J.; Gaussian, Inc. Wallingford CT, **2013**.

Chapter 3
Evaluation of the effect of annelated structure on hopping transport

3.1 Introduction

Elucidating the relationship between molecular structures and carrier transport characteristics is crucial for the development of both organic thin-film electronics and single-molecule electronics.[1-4] Carrier transport in thin films, such as in organic field-effect transistors and organic solar cells, is generally explained by a hopping transport mechanism between neighboring molecules.[5,6] Therefore, the π-conjugated framework with appropriate hole/electron injection properties and the molecular alignment in the solid state are considered key factors for efficient intramolecular and intermolecular carrier transport.[7, 8]

In contrast, carrier transport in single-molecule electronics (i.e., metal/molecule/metal junctions) is primarily governed by the intramolecular carrier transport characteristics at the molecular level.[9-12] It is well known that the intramolecular carrier transport mechanism depends on the molecular length: tunneling transport occurs in shorter molecular lengths, while hopping transport is observed in longer molecular lengths, typically beyond a few nanometers.[13-17] Many efforts have been made to uncover correlations between molecular structures and charge transport characteristics in tunneling conduction mechanisms.[18-26] However, detailed studies on the influence of chemical structures on hopping transport are still limited, despite fundamental aspects such as length-dependent conductance and the crossover between tunneling and hopping having been revealed using representative long π-conjugated oligomers.[27-33]

In hopping transport, charge carriers move by hopping between localized electronic states, referred to as hopping sites.[34] First, charge carriers move from the electrode to the hopping site adjacent to the electrode, where the energy offset between the Fermi level of the electrode and the hopping site is referred to as the injection barrier. Charge flow in hopping transport within the molecular chain is described by the Arrhenius equation (eq 1).

$$k = Ae^{\frac{-E_a}{k_B T}} \qquad (1)$$

where k is the rate constant, A is the pre-exponential factor, k_B is the Boltzmann constant, T is the temperature, and E_a is the activation energy. To achieve highly efficient hopping transport, molecular design guidelines aimed at reducing E_a are essential. E_a is correlated with the reorganization energy of the hopping site (λ) and sum of energy difference between hopping sites (ΔE_{hs}) (Fig. 3-1a).[35-37]

To reduce ΔE_{hs}, the intramolecular hopping sites should be electronically identical and periodic.[38] To achieve this, Ie and coworkers introduced a periodically twisted structure in the molecular wire by incorporating head-to-head bithiophene units, resulting in the development of periodically twisted oligothiophenes.[39] Recently, the author designed an annelated structure of thienobenzo[b]indacenodithiophene (**TBID**) as a π-conjugated framework for the hopping site to reduce λ and developed its repeated, periodically twisted molecular wires, **NCS-(TBID)$_n$-SCN** (n = 2, 3) (Fig. 3-1b).[40] Reflecting the reduction of ΔE_{hs} and λ, **NCS-(TBID)$_n$-SCN** (n = 2, 3) exhibited improved hopping conductance compared to oligothiophenes. To establish rational design principles for the hopping site, an investigation of the structure-property relationship based on the **TBID** framework is a highly effective approach.

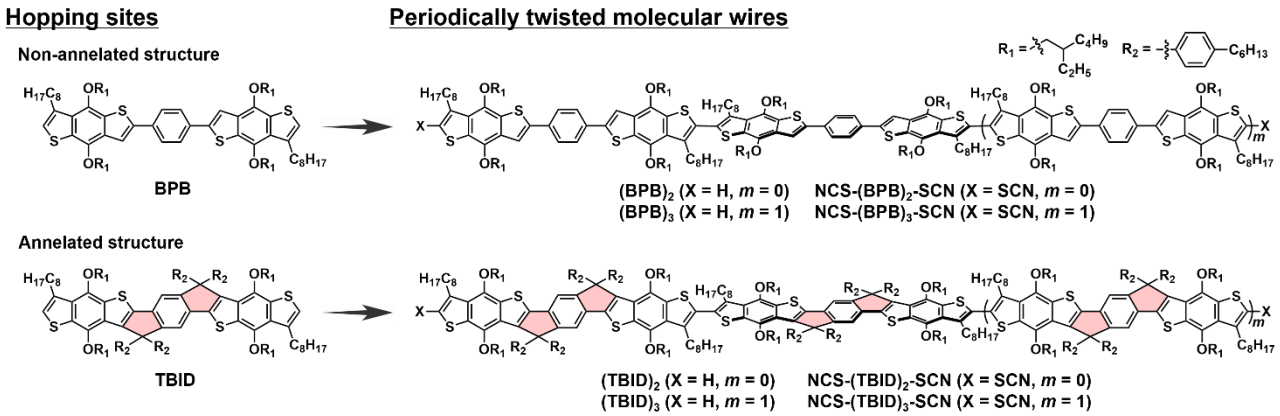

Figure 3-1. (a) Schematic of intramolecular hopping transport and relationship between E_a, λ, and ΔE_{hs}; h^+ stands for holes. (b) Molecular structures of hopping sites and periodically twisted molecular wires used in this study.

In this context, the author focused on the π-conjugated framework of 1,4-bis(benzo[1,2-b:4,5-b']dithiophen-2-yl)benzene (**BPB**), which is essentially the **TBID** structure without the annelation. In this study, the author designed and synthesized several nanometer-scale molecular wires, **NCS-(BPB)$_n$-SCN** (n = 2, 3), to investigate intramolecular hopping transport (Fig. 3-1b). Physical property measurements, single-molecule conductance measurements, and theoretical studies were conducted to clarify the influence of the annelated structure on the hopping site and its effect on hopping transport.

3.2 Synthesis

The synthetic route for **(BPB)$_n$** (n = 2, 3) and **NCS-(BPB)$_n$-SCN** (n = 2, 3) is shown in Scheme 3-1. The starting material, **BPB**, was synthesized according to a previous report.[39] The bromination of **BPB** was performed by treatment with *n*-BuLi and CBr_4, yielding **BPB-Br**. Stannylation of **BPB-Br** was carried out using hexamethylditin **(SnMe$_3$)$_2$**, followed by *in situ* Stille coupling under microwave irradiation to obtain oligomers. The destannylation and protonation reactions were then performed to remove the remaining $SnMe_3$ and Br groups, yielding **(BPB)$_n$**. Finally, SCN groups were introduced at the terminal positions of **(BPB)$_n$**, producing the target compounds, **NCS-(BPB)$_n$-SCN**.

Scheme 3-1. Synthetic route of **(BPB)$_n$** (n = 2, 3) and **NCS-(BPB)$_n$-SCN** (n = 2, 3).

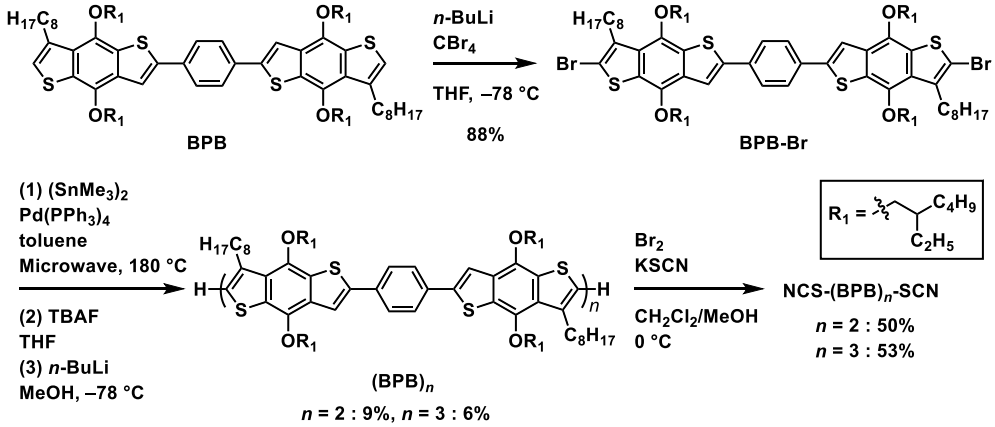

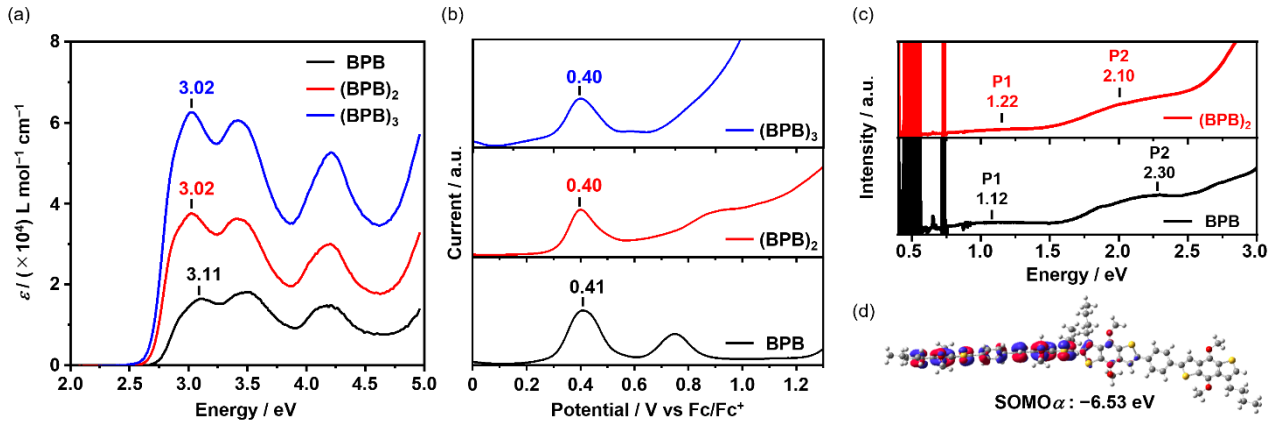

Figure 3-2. (a) UV-vis absorption spectra of **BPB** (black), **(BPB)$_2$** (red), and **(BPB)$_3$** (blue) in CH_2Cl_2. (b) Differential pulse voltammograms of **BPB** (black), **(BPB)$_2$** (red), and **(BPB)$_3$** (blue) in CH_2Cl_2 containing 0.1 M $TBAPF_6$. (c) UV-vis-NIR spectra of **(BPB)$_2$** (top) and **BPB** (bottom) in CH_2Cl_2 under oxidation with magic blue. (d) The calculated SOMO orbitals of **[BPB(Me)]$_2^{\bullet+}$** at the CAM-UB3LYP/6-31g(d,p) level.

3.3 Photophysical properties

To investigate the photophysical properties, UV-vis absorption spectra of **BPB** and **(BPB)$_n$** (n = 2, 3) in dichloromethane (CH_2Cl_2) solutions were measured (Fig. 3-2a and S3-1). The photophysical data, along with those for **TBID**-repeated oligomers, are summarized in Table 3-1. As shown in Fig. S3-1, **BPB**-based derivatives exhibited similar absorption spectra, with absorption maxima ($\lambda_{abs,max}$) at 410 nm and 411 nm for **(BPB)$_2$** and **(BPB)$_3$**, respectively. The slight red shift observed in **(BPB)$_n$** (n = 2, 3) compared to **BPB** ($\lambda_{abs,max}$ = 399 nm) can be attributed to the electron-donating nature of the **BPB** unit. The molar absorption coefficient (ε) increased proportionally from **BPB** to **(BPB)$_3$** as the number of **BPB** units increased. These results indicate that conjugation is effectively distributed due to the presence of head-to-head structures. The **BPB**-based molecules also showed relatively broader absorption spectra compared to the corresponding TBID-based counterparts. The fluorescence spectra of **BPB** and **(BPB)$_n$** (n = 2, 3) in CH_2Cl_2 solutions are shown in Fig. S3-2.

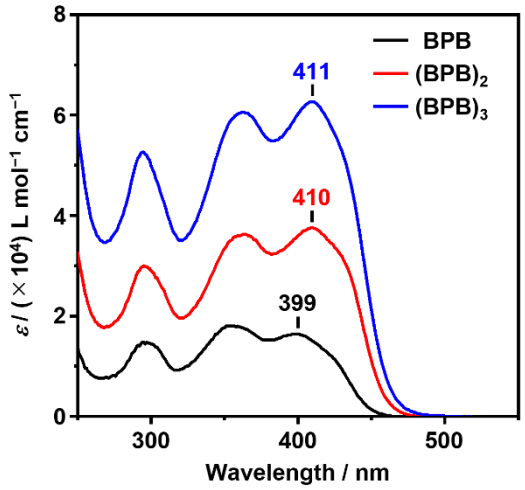

Figure S3-1. UV-vis absorption spectra of **BPB** (black), **(BPB)$_2$** (red), and **(BPB)$_3$** (blue) in CH_2Cl_2.

Table 3-1. Physical properties.

Compd.	$\lambda_{abs,\,max}$ / nm[a]	$\lambda_{PL,\,max}$ / nm[a]	fwhm$_{PL}$ / cm^{-1}[a]	Stokes shift / cm^{-1}[a]	E_{ox} / eV[b]	E_{HOMO} / eV[c]
BPB[d]	399	544	4300	6700	0.41	−5.21
(BPB)$_2$	410	543	4300	6000	0.40	−5.20
(BPB)$_3$	411	543	4200	5900	0.40	−5.20
TBID[d]	442	551	2600	4500	0.35	−5.15
(TBID)$_2$[d]	453	551	2600	3900	0.37	−5.17
(TBID)$_3$[d]	456	551	2500	3800	0.37	−5.17

[a]In CH_2Cl_2. [b]Determined by DPV in CH_2Cl_2 containing 0.1 M of $TBAPF_6$. [c]Estimated by $E_{HOMO} = -(E_{ox} + 4.80)$ eV. [d]Data are extracted from Ref 40.

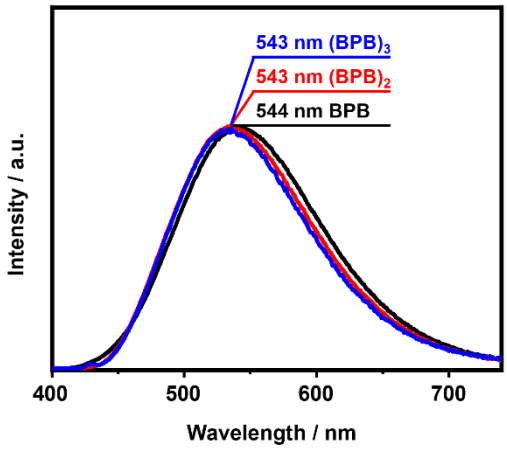

Figure S3-2. Fluorescence spectra of **BPB** (black), **(BPB)$_2$** (red), and **(BPB)$_3$** (blue) in CH_2Cl_2.

Regardless of the number of **BPB** units, the maximum emission ($\lambda_{PL,\,max}$) was observed around 543 nm for all the compounds. This suggests that the twisted chemical structures are retained even in the photoexcited state. Focusing on the full width at half maximum of the emission spectrum (fwhm$_{PL}$), **TBID** showed a value of around 2600 cm^{-1}, while **BPB** exhibited a larger value of approximately 4300 cm^{-1}. The Stokes shift of **BPB** was significantly larger than that of **TBID**. The fwhm$_{PL}$ and Stokes shift of **(BPB)$_n$** (n = 2, 3) and **(TBID)$_n$** (n = 2, 3) followed similar trends to those of **BPB** and **TBID**, respectively. These phenomena suggest that the flexible **BPB** framework increases vibrational transitions and induces larger structural changes in the excited state.

3.4 Electrochemical analysis

To investigate the electrochemical properties of **BPB** and **(BPB)$_n$** (n = 2, 3), oxidation potentials (E_{ox}) were determined by differential pulse voltammetry (DPV) in CH_2Cl_2 solutions containing tetrabutylammonium hexafluorophosphate ($TBAPF_6$) (Fig. 3-2b). The voltammograms were calibrated against the ferrocene/ferrocenium (Fc/Fc^+) couple. Assuming that the Fc/Fc^+ redox couple lies below 4.8 eV from the vacuum level, the highest occupied molecular orbital (HOMO) energy level of **BPB** was calculated to be −5.21 eV, which is lower than that of **TBID** (−5.15 eV). The E_{ox} values for **BPB**-repeated oligomers were observed at similar values, around 0.40 eV

(Table 3-1). This result indicates that the E_{ox} of **(BPB)$_n$** (n = 2, 3) originates from the **BPB** unit, reflecting the localized electronic distribution.

3.5 Photophysical properties of radical cationic species

To investigate the key species involved in carrier transport, UV-vis-NIR spectra of **BPB** and **(BPB)$_2$** in CH_2Cl_2 were measured in the presence of tris(4-bromophenyl)-ammoniumyl hexachloroantimonate (magic blue) as an oxidant. As shown in Fig. 3-2c, the addition of magic blue resulted in the one-electron oxidation of **BPB**, and the resulting **(BPB)$^{\bullet+}$** exhibited two absorption bands at P1 = 1.12 eV and P2 = 2.30 eV. To assign these transitions, time-dependent (TD) DFT calculations of **(BPB)$^{\bullet+}$** were performed at the CAM-UB3LYP/6-31g(d,p) level. As summarized in Fig. S3-3, the P1 and P2 bands were assigned to the HOMO-singly occupied molecular orbital (SOMO) and SOMO-lowest unoccupied molecular orbital (LUMO) transitions, respectively. **(BPB)$_2^{\bullet+}$** also exhibited two bands (P1: 1.22 eV, P2: 2.10 eV), with values similar to those observed for **(BPB)$^{\bullet+}$** (Fig. 3-2c and S3-4).

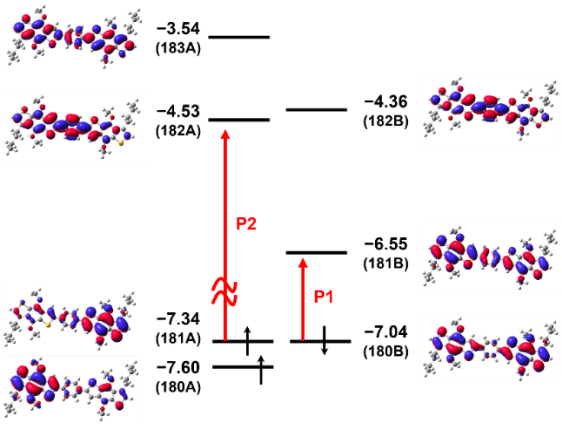

Figure S3-3. Calculated energy levels of **BPB$^{\bullet+}$** and estimated excited states. Optimization was conducted at the B3LYP/6-31g(d,p) level. Optimized local minimum structures at the excited state were subjected to TD-DFT calculations at the CAM-UB3LYP/6-31g(d,p) level.

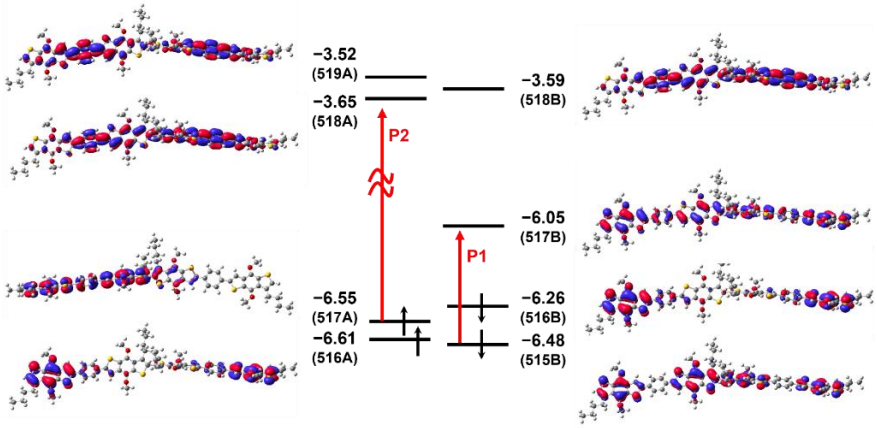

Figure S3-4. Calculated energy levels of **(BPB)$_2^{\bullet+}$** and estimated excited states. Optimization was conducted at the B3LYP/6-31g(d,p) level. Optimized local minimum structures at the excited state were subjected to TD-DFT calculations at the CAM-UB3LYP/6-31g(d,p) level.

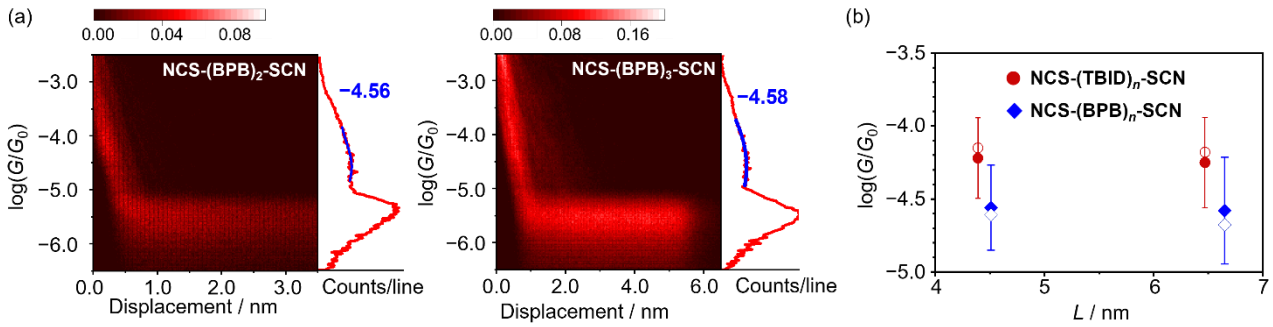

Figure 3-3. (a) 2D conductance histograms of **NCS-(BPB)$_n$-SCN** (n = 2, 3). Blue curves represent the result of Gaussian fit. Conductance values are determined from the peak top. $G_0 = 2e^2h^{-1}$, where e and h are the elementary charge and Planck constant, respectively. (b) Log(G/G_0) versus L for **NCS-(BPB)$_n$-SCN** (n = 2, 3) and **NCS-(TBID)$_n$-SCN** (n = 2, 3). Filled and open symbols denote experimental and simulated values, respectively. Note that error bars represent the standard error for the fitting Gaussian function to the histogram.

These results suggest that the periodically twisted structures of the **BPB**-repeating oligomers can localize the radical cationic state within the **BPB** unit (Fig. 3-2d), thus achieving aligned energy levels between hopping sites (small small ΔE_{hs}). The calculated transfer integrals between hopping sites at 300 K range from 18 to 83 meV (Fig. S3-5), indicating that charge transport between hopping sites is facilitated.

3.6 Single-molecule conductance measurements

The electrical conductance (G) of single-molecule junctions for **NCS-(BPB)$_n$-SCN** (n = 2, 3) was measured using the scanning tunneling microscope-break junction (STM-BJ) method.[12,42] In this method, gold metal contacts were initially formed by bringing a gold STM tip into contact with a gold substrate modified with molecules. Molecular junctions were formed when the gold metal junctions were broken upon retraction of the STM tip. During the retraction process, plateaus and steps appeared in the conductance trace, indicating the formation of the molecular junction between the gold electrodes.

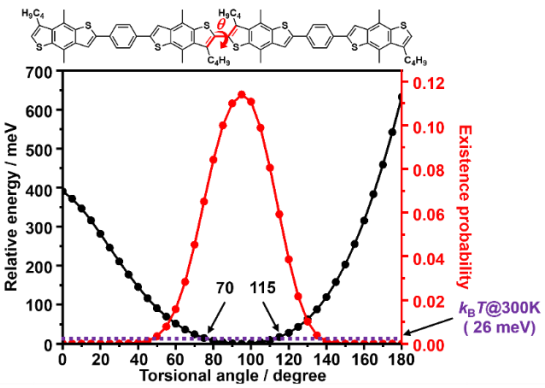

Torsional angle / degree	Existence probability	HOMO / eV	HOMO−1 / eV	Transfer integral / meV
95 (Most stable structure)	0.11	−5.036	−5.072	18
70	0.045	−5.028	−5.078	25
115	0.059	−4.982	−5.088	53

Figure S3-5. Torsional scans and population analysis.

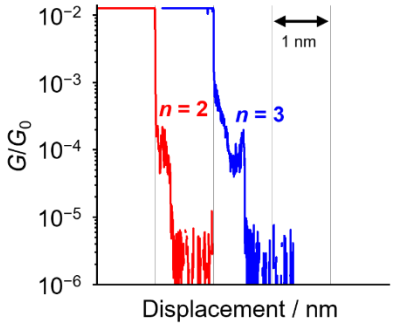

Figure S3-6. Typical conductance transients observed for **NCS-(BPB)$_n$-SCN** (n = 2, 3).

As shown in Fig. S3-6, typical conductance traces with plateaus were observed for **NCS-(BPB)$_n$-SCN** (n = 2, 3). The two-dimensional (2D) histograms and corresponding conductance histograms for **NCS-(BPB)$_n$-SCN** (n = 2, 3) are shown in Fig. 3-3a. Based on Gaussian fitting, the experimental G values were determined to be $1.2 \pm 0.3 \times 10^{-5}$ and $0.9 \pm 0.3 \times 10^{-5}$ G_0 for **NCS-(BPB)$_2$-SCN** and **NCS-(BPB)$_3$-SCN**, respectively. The plot of $\log(G/G_0)$ versus molecular length (L) for **NCS-(BPB)$_n$-SCN** (n = 2, 3) and **NCS-(TBID)$_n$-SCN** (n = 2, 3) (valued taken from Ref 40), were illustrated in Fig. 3-3b. The molecular lengths of these compounds correspond to the hopping-transport regime. As illustrated in Fig. 3-3b, **NCS-(BPB)$_n$-SCN** (n = 2, 3) showed lower G values compared with those of **NCS-(TBID)$_n$-SCN** (n = 2, 3). The author theoretically estimated the G values using Landauer-Büttiker probe (LBP) simulations. The details of these simulations are summarized in the Experimental section. Note that the contribution of tunneling conduction for these molecules was orders of magnitudes smaller than that of hopping conduction. The calculated G values were determined to be 2.5×10^{-5} and 2.1×10^{-5} G_0 for **NCS-(BPB)$_2$-SCN** and **NCS-(BPB)$_3$-SCN**, respectively. These values are in good agreement with the experimental results (Fig. 3-3b).

3.7 Theoretical studies

To discuss the single-molecule conductance behavior of **NCS-(BPB)$_n$-SCN** (n = 2, 3) and **NCS-(TBID)$_n$-SCN** (n = 2, 3), the author first compared the λ of the hopping sites (**BPB** and **TBID**) using DFT calculations at the B3LYP/6-31g(d,p) level of theory. The alkyl groups of **BPB** and **TBID** were replaced with methyl groups (denoted as **BPB(Me)** and **TBID(Me)**) to reduce computational cost (Fig. 3-4a). The λ value of **BPB(Me)** was calculated to be 198 meV, which is larger than that of **TBID(Me)** (171 meV). As shown in Fig. 3-4a, while **BPB(Me)** possesses a distorted structure with a dihedral angle of 24° between the benzodithiophene and benzene rings in the neutral state, this conformation changes to a planar structure in the radical cationic state. The superimposed side views of these electronic states are shown in Fig. 3-4b. In contrast, **TBID(Me)** exhibits planar structures in both the neutral and radical cationic states due to annelation. Therefore, the conformational change in **BPB(Me)** between neutral and radical cationic states contributes to a relatively larger λ compared to **TBID(Me)**.

To investigate the influence of the annelated structure on thermal fluctuations, the author next calculated the distribution of the highest occupied molecular orbital (HOMO) energy levels for **BPB** and **TBID** using DFT-molecular dynamics (MD) simulations. To focus on the thermal fluctuations of the π-conjugated framework, the molecular structures were simplified by omitting alkyl chains (denoted as **BPB^{nosub}** and **TBID^{nosub}**).

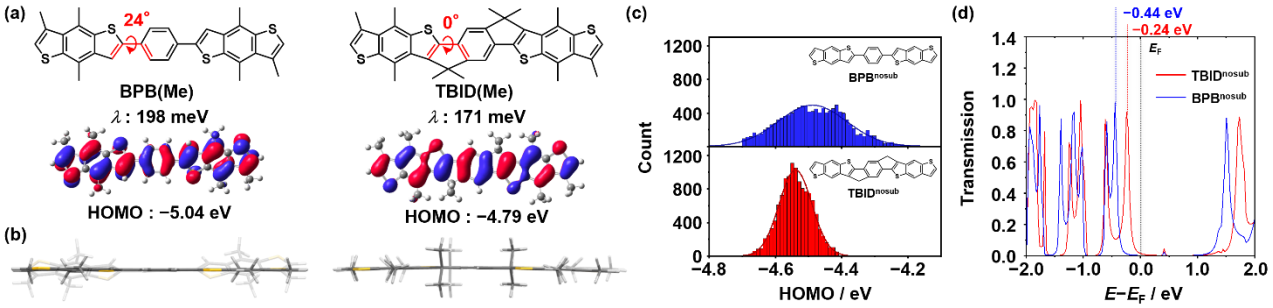

Figure 3-4. (a) Molecular structures, λ values, HOMO orbitals and calculated HOMO energy levels of **BPB(Me)** and **TBID(Me)**. (b) The side views of radical cationic (solid stick) and the ground (semitransparent stick) states for **BPB(Me)** and **TBID(Me)**. (c) Distribution of HOMO energy levels calculated from DFT-MD for **BPB^{nosub}** (blue) and **TBID^{nosub}** (red). (d) Transmission functions of **BPB^{nosub}** (blue) and **TBID^{nosub}** (red) calculated by NEGF-DFT.

The HOMO orbitals were delocalized across the entire π-conjugated framework in both **BPB(Me)** and **TBID(Me)**. The HOMO energy level of **BPB(Me)** was estimated to be −5.04 eV, which is lower than that of **TBID(Me)** (−4.79 eV). The higher HOMO energy level of **TBID(Me)** is explained by the electron-donating nature of its alkyl-annelated structure. To investigate the electrocoupling between gold electrodes and molecules, nonequilibrium Green's function method combined with DFT (NEGF-DFT) calculations were performed. As shown in Fig. 3-4d, **BPB^{nosub}** exhibited a larger negative $E-E_F$ value of −0.44 eV compared to **TBID^{nosub}** (−0.22 eV), indicating that **BPB^{nosub}** has a larger injection barrier than **TBID^{nosub}**.

As illustrated in Fig. 3-4c, **BPB^{nosub}** showed a broader HOMO distribution than **TBID^{nosub}**. This result suggests that the presence of annelation is effective in suppressing thermal fluctuations. Therefore, the author concluded that, in addition to the periodic twist in the molecular wire, the annelated structure at the hopping site is crucial for achieving a small ΔE_{hs}. This phenomenon aligns well with the experimentally determined high-lying HOMO energy level of **TBID(Me)**. These findings indicate that the electronic structure of annelation in **TBID(Me)** also contributes to increasing the single-molecule conductance. Through these theoretical studies, the author concluded that the annelated structure at the hopping site has the potential to enhance hopping-transport characteristics by tuning λ, ΔE_{hs}, and injection barrier.

3.8 Conclusion

In summary, to elucidate the relationship between the chemical structure of the hopping site and hopping transport in molecular wires, the author designed a non-annelated **BPB** by simply removing the annelation from **TBID**. As a result, the author successfully synthesized periodically twisted molecular wires based on the **BPB** unit, approximately 4-7 nm in length. Photophysical measurements indicated that **BPB** showed broader bands in both the absorption and fluorescence spectra compared to **TBID**, which can be attributed to the structural flexibility of **BPB**. Electrochemical measurements estimated the HOMO energy level of **BPB** to be −5.21 eV, which is lower than that of **TBID** (−5.15 eV). Single-molecule conductance measurements using the STM-BJ technique revealed that **NCS-(BPB)$_n$-SCN** (n = 2, 3) exhibited lower conductance values compared to **NCS-(TBID)$_n$-SCN** (n = 2, 3). Theoretical studies indicated that the structural change between the ground state and the radical cationic state in **BPB** is more significant than in **TBID**, resulting in an increase in λ. The distribution of the HOMO energy level is broader for **BPB** than for **TBID**. Additionally, **BPB** has a larger injection barrier than **TBID** due to its lower HOMO energy level. This study suggests that the introduction of the annelated structure at the hopping site, which reduces λ, ΔE_{hs}, and injection barrier, is effective for achieving efficient intramolecular hopping transport in molecular wires.

3.9 Experimental Section

General Information

Column chromatography was conducted on KANTO Chemical silica gel 60N (40–50 μm). Microwave irradiation was performed using a Biotage Initiator+ 4.2.1. The microwave power output was set to 400 W, and the internal temperature during the reaction was monitored by an IR sensor. Preparative gel permeation chromatography (GPC) was carried out using a Japan Analytical Industry LC-9210 NEXT system equipped with a JAI-GEL 1HH/2HH or JAI-GEL 2.5HH/3HH column. ^{1}H and ^{13}C NMR spectra were recorded on a JEOL JNM-ECS400, JNM-ECA600 in $CDCl_3$ with tetramethylsilane (TMS) as an internal standard. Chemical shifts are reported in ppm (δ), multiplicity (s = singlet, d = doublet, t = triplet, q = quartet, quin = quintet, sep = septet, brs = broad singlet, m = multiplet, dd = double doublet, td = triplet doublet), coupling constant (Hz), and integration. High-resolution mass spectra (HRMS) were obtained by atmospheric pressure chemical ionization (APCI) or electrospray ionization (ESI) methods using a Thermo Scientific LTQ Orbitrap XL or a MALDI-spiralTOF method by using a JEOL JMS-S3000. All chemicals and reagents were produced from commercial sources (FUJIFILM Wako Chemicals (Tokyo, Japan), TCI (Tokyo, Japan) and Sigma Aldrich (MO, USA)).

Physical property measurements

UV-vis-NIR spectra were recorded on a Shimadzu UV-3600 spectrophotometer. Fluorescence spectra were recorded using a Fluoromax-2 spectrometer in the photon-counting mode equipped with a Hamamatsu R928 photomultiplier. All spectra were obtained in spectrograde solvents. DPV measurement was carried out on a BAS CV-620C voltammetric analyzer using a platinum disk as the working electrode, platinum wire as the counter electrode, and $Ag/AgNO_3$ as the reference electrode at a scan rate of 100 mV s^{-1} in a CH_2Cl_2 solution containing 0.1 M $TBAPF_6$.

Electrical conductance measurements by the break junction method

The STM-BJ measurements were conducted using a PicoSPM (Molecular Imaging) controlled by a PicoScan2500 controller under an Ar atmosphere at room temperature. The sensitivity of the current-to-voltage converter was 10^{-6} A V^{-1}, which limited the largest current and thus the measured conductance. For temperature-dependence measurements, a heating stage provided by Molecular Imaging was utilized. The surface temperature at the heating stage was monitored using a resistive sensor. Gold STM tips were prepared by mechanical cutting of gold wires. Gold substrates were fabricated by thermally evaporating gold onto freshly cleaved mica sheets. During evaporation, the mica sheets were heated at approximately 500 K. Atomically flat Au(111) terraces could be observed on the surface of the gold substrate. The gold substrates were modified with the oligomers by immersing them in a 0.1 mM CH_2Cl_2 solution of the molecules at room temperature for 10 min. After removal from the solution, the substrates were dried by evaporation of the solvent. The peak in the conductance histogram was determined by fitting a Gaussian function.

Tunneling transport calculations

The transport properties of the molecules were calculated using the izanami package[40] containing the automatic construction of molecular junction structures from a given gas-phase structure using DFT, transport calculations with a nonequilibrium Green's function (NEGF), and post-process analysis. The package utilizes the SMEAGOL code[41-43] and SIESTA package[44]. Single zeta plus polarization (SZP) and double zeta plus polarization (DZP) basis sets were used for Au and other atoms, respectively. The author used the Perdew-Burke-Ernzerhof (PBE) exchange-correlation functional.[45] The electrode was modeled as an Au(111) slab with the p(6×6) periodicity. The k points were sampled using a 2×2×1 uniform grid.

Modeling of hopping transport

The author employed the Landauer-Büttiker probe (LBP) method[46, 47] to simulate length-dependent conductance, including tunneling and hopping contributions. In the LBP method, a molecular chain is represented by connected hopping sites, and the environmental effects are described using probes attached to each site. The probe has its own chemical potential, which is consistently determined by the voltage gradient applied between the left and right electrodes.

The author considers a one-dimensional tight-binding chain as the Hamiltonian,

$$\hat{H} = \sum_{i=1}^{N} \varepsilon_a \hat{c}_i^{\dagger} \hat{c}_i + \sum_{i=1}^{N-1} t\left(\hat{c}_i^{\dagger} \hat{c}_{i+1} + h.c.\right) \quad \text{(S1)}$$

where e_a is the site energy of the oligomer unit and t is the transfer integral. The retarded Green's function is given by

$$\hat{G}^r(\varepsilon) = \left[\hat{I}\varepsilon - \hat{H} + i\hat{\Gamma}/2\right]^{-1} \quad \text{(S2)}$$

where $\hat{\Gamma} = \hat{\Gamma}_L + \hat{\Gamma}_R + \sum_{i=1}^{N} \hat{\Gamma}_i^{\text{probe}}$. The first and N_{th} sites are coupled to the left and right electrodes, respectively. Therefore, the electrode coupling matrices become

$$\left[\hat{\Gamma}_L\right]_{1,1} = \gamma_L, \ \left[\hat{\Gamma}_R\right]_{N,N} = \gamma_R \quad \text{(S3)}$$

where $g_{L,R}$ coupling energy of the electrode. Here, the author assume that $g_{L,R}$ is independent of energy and ignores the energy shifts of molecular orbital due to the coupling with electrodes. The author also assumes that the coupling to the probe is local and independent of the site, which leads to

$$\left[\hat{\Gamma}_i^{\text{probe}}\right]_{i,i} = \gamma_d, \ i = 1,2,\ldots,N \quad \text{(S4)}$$

The transmission coefficients between all the electrodes and probes can be described as

$$\mathcal{T}_{\alpha,\alpha'}(\varepsilon) = \text{Tr}\left[\hat{\Gamma}_\alpha(\varepsilon)\hat{G}^r(\varepsilon)\hat{\Gamma}_{\alpha'}(\varepsilon)\hat{G}^a(\varepsilon)\right], \ \alpha = L, 1,2,\ldots,N,R, \quad \text{(S5)}$$

where $\hat{G}^a(\varepsilon) = \left[\hat{G}^r(\varepsilon)\right]^{\dagger}$ is the advanced Green's function.

The chemical potentials of probes, $\{\mu_i\}$, which are given through the Fermi distribution function $f_\alpha(\varepsilon) = [\exp[(\varepsilon - \mu_\alpha)/k_B T] + 1]^{-1}$, where k_B is the Boltzmann constant and T is the temperature, should be determined to guarantee the charge conservation as follows,

$$I_i = \frac{2e}{h}\sum_\alpha \int_{-\infty}^{\infty} d\,\varepsilon \mathcal{T}_{i,\alpha}(\varepsilon)[f_i(\varepsilon) - f_\alpha(\varepsilon)] = 0. \quad \text{(S6)}$$

The author assumes the linear response regime and Taylor-expand the Fermi distribution function as

$$f_\alpha(\varepsilon, \mu_\alpha) = f(\varepsilon, \varepsilon_F) - \frac{\partial f(\varepsilon, \varepsilon_F)}{\partial \varepsilon}(\mu_\alpha - \varepsilon_F). \quad \text{(S7)}$$

Using equation S7, equation S6 can be rewritten as

$$\sum_\alpha \int_{-\infty}^{\infty} d\,\varepsilon \mathcal{T}_{i,\alpha}(\varepsilon)\left(-\frac{\partial f}{\partial \varepsilon}\right)\varepsilon(\mu_i - \mu_\alpha) = 0 \qquad \text{(S8)}$$

where the author set $e_F = 0$. By solving the above N simultaneous equations, the author obtains the set of probe parameters $\{\mu_i\}$. Finally, the source-drain current can be calculated as

$$I_L = \frac{2e}{h}\sum_\alpha \left[(\mu_L - \mu_\alpha)\int_{-\infty}^{\infty} d\varepsilon \mathcal{T}_{i,\alpha}(\varepsilon)\left(-\frac{\partial f}{\partial \varepsilon}\right)\right]. \qquad \text{(S9)}$$

The author performed the calculations with the bias voltage of 0.1 V and computed the conductance values.
The author adopted the parameters for **TBID** from our previous paper[40]. $t = 0.03$ eV was obtained from the energies of the HOMO and HOMO-1 of **TBID(Me)**. The major source of γ_d is considered to be the electron-phonon coupling[48] that has a similar order of value with the reorganization energy.[49] Therefore, the author adopted 0.170 eV for γ_d of **TBID**, taken from the calculated reorganization energy. The author set $\varepsilon_a = -0.41$ eV, which is a typical value for molecular junctions. The other parameters were $\gamma_{L,R} = 0.0002$ eV, and $T = 280$ K, which were adjusted to fit the measured conductance values. Subsequently, the author determined the parameters for **BPB**. The energy level was shifted as −0.30 eV according to the DFT calculated HOMO. $\gamma_d = 0.200$ eV was obtained from the calculated reorganization energy. The author employed the same $\gamma_{L,R}$, t, and T with **TBID**. The calculated conductance values of **NCS-(BPB)$_n$-SCN** ($n = 2, 3$) were 2.5×10^{-5} and 2.1×10^{-5} G_0, respectively. The author also calculated tunneling conductance values by setting $\gamma_d = 0$. The calculated results were 8.0×10^{-11} and 1.4×10^{-13} G_0, respectively, which were significantly smaller than the hopping contributions.

Fluctuation of the HOMO levels

The author carried out DFT molecular dynamics (MD) simulations for **BPB$^{\text{nosub}}$**, where alkyl chains are omitted for simplification. The author simulated one molecule in a cubic cell whose cell length is 50.0 Å. For the DFT-MD simulation, the author used the BLYP exchange correlation functional together with the Grimme's D3(0) van der Waals correction. The author employed the QUICKSTEP method implemented in the CP2K code.[50, 51] For the Gaussian part of the basis set, the author used the DZVP basis set. The author set the plane wave density cutoff to 320 Ry. The author performed DFT-MD simulation in the NVT ensemble, where the target temperature was set to 300 K with canonical sampling through a velocity rescaling thermostat. The time step for integrating equation of motions was set to 0.4 fs. The author equilibrated the sample for 5 ps and then the author obtained 5 ps DFT-MD trajectory.

Synthesis and characterization

Synthesis of ***BPB-Br***: **BPB**[1] (90 mg, 0.076 mmol) was dissolved in anhydrous THF (10 mL) and cooled to −78 °C under a nitrogen atmosphere. A solution of *n*-BuLi (1.51 M, 1.0 mL, 1.51 mmol) in hexanes was added dropwise to the reaction mixture. The mixture was stirred at −78 °C for 1 h and then, a solution of CBr_4 (760 mg, 2.28 mmol) in THF (5 mL) was added to the reaction mixture and stirred at room temperature for 16 h. The reaction was quenched with the addition of water (10 mL). The resulting mixture was extracted with $CHCl_3$, and the organic layer was dried over anhydrous sodium sulfate, filtered and evaporated in vacuo. Column chromatography was performed on silica gel (hexane:$CHCl_3$ = 5:1). Further purification was conducted by recycling GPC (JAI-GEL 1HH/2HH, $CHCl_3$ as an eluent) to obtain **BPB-Br** as a yellow solid (90 mg, 0.067 mmol, 88%). ^{1}H NMR (400 MHz, $CDCl_3$, δ): 0.87-1.06 (m, 30H), 1.25-1.53 (m, 38H), 1.58-1.75 (m, 18H), 1.83 (quin, J = 6.0 Hz, 2H), 2.00 (quin, J = 6.4 Hz, 2H), 2.98 (t, J = 7.8 Hz, 4H), 4.05-4.12 (m, 4H), 4.15 (d, J = 5.5 Hz, 4H), 7.68 (s, 2H), 7.81 (s, 4H); ^{13}C NMR (101 MHz, $CDCl_3$, δ): 144.7, 144.0, 142.9, 136.5, 134.2, 132.1, 130.8, 130.7, 129.4, 127.0, 116.0, 112.8, 77.3, 76.5, 40.8, 40.6, 32.0, 30.5, 30.4, 30.2, 29.8, 29.8, 29.7, 29.5, 29.3, 29.3, 23.9, 23.8, 23.3, 22.8, 14.3, 14.2, 11.4, 11.3; HRMS (APCI) m/z: $[M+H]^+$ calcd. for $C_{74}H_{109}Br_2O_4S_4$, 1347.5570; found, 1347.5581.

Synthesis of ***(BPB)$_2$*** and ***(BPB)$_3$***: **BPB-Br** (169 mg, 0.13 mmol), $(SnMe_3)_2$ (66 mg, 0.20 mmol), $Pd(PPh_3)_4$ (14 mg, 0.012 mmol), and toluene (4 mL) were placed in a microwave proof walled glass vial equipped with a snap cap. The glass vial was purged with nitrogen, securely sealed, and heated in a microwave reactor with keeping the temperature at 180 °C for 13 min. After cooling to room temperature, the mixture was concentrated under reduced pressure, and then the residue was purified by column chromatography on silica gel (hexane:$CHCl_3$ = 5:1).

After addition of TBAF (1.0 M, 5 mL, 5 mmol) in THF, the reaction mixture was refluxed for 1 h. Then, an NH_4Cl aqueous solution (10 mL) and Et_2O (10 mL) were added to the reaction mixture, and the mixture was extracted with Et_2O three times. The combined organic layer was dried with anhydrous sodium sulfate and evaporated in vacuo.

Anhydrous THF (10 mL) was added to the residue, and the solution was cooled to −78 °C. A solution of *n*-BuLi (1.51 M, 0.4 mL, 0.60 mmol) in hexane was added dropwise under a nitrogen atmosphere. After stirring for 1 h, MeOH (2 mL) was added dropwise. The reaction mixture was kept at −78 °C for 1 h and then stirred at room temperature for 1 h. After quenching the reaction with the addition of water (10 mL), the resulting mixture was extracted with $CHCl_3$. The organic layer was dried with anhydrous sodium sulfate and evaporated in vacuo. Column chromatography was performed on silica gel (hexane:AcOEt = 10:1). Then, recycling GPC (JAIGEL 2.5HH/3HH, $CHCl_3$ as an eluent) was performed to obtain **(BPB)$_2$** (29 mg, 12 μmol, 9%) and **(BPB)$_3$** (27 mg, 7.5 μmol, 6%).
(BPB)$_2$: Yellow solid; ^{1}H NMR (400 MHz, $CDCl_3$, δ): 0.80-1.06 (m, 60H), 1.16-1.43 (m, 78H), 1.58-1.86 (m, 30H), 1.96- 2.06 (m, 4H), 2.91-2.94 (m, 4H), 3.04 (t, J = 6.0 Hz, 4H), 4.10-4.24 (m, 24H), 6.98 (s, 2H), 7.73-7.75 (m, 4H), 7.84 (s, 8H); ^{13}C NMR (151 MHz, $CDCl_3$, δ): 157.6, 145.7, 145.3, 144.4, 141.3, 139.3, 137.3, 137.2, 137.1, 137.0, 135.8, 135.1, 131.8, 131.2, 131.1, 131.0, 129.1, 128.7, 128.1, 127.9, 126.6, 119.9, 116.6, 78.3, 77.9, 65.5, 65.5, 65.4, 64.8, 64.7, 42.2, 42.1, 42.1, 40.7, 40.6, 40.5, 40.4, 39.3, 39.2, 39.1, 35.7, 32.1, 31.9, 31.7, 31.4, 31.3, 30.6, 30.4, 30.3, 30.2, 30.1, 29.8, 29.8, 29.6, 29.5, 29.3, 29.3, 29.3, 28.9, 28.7, 28.6, 23.9, 23.6, 23.5, 23.3, 23.3, 23.2, 22.8, 22.7, 22.4, 14.4, 14.3, 14.2, 13.7, 11.6, 11.5, 11.4, 11.3, 11.3, 11.2, 11.0, 10.8, 10.8, 10.7.

(BPB)$_3$: Yellow solid; ^{1}H NMR (400 MHz, $CDCl_3$, δ): 0.80-1.29 (m, 232H), 1.42 (brs, 26H), 1.67-1.85 (m, 8H), 1.94-2.04 (m, 4H), 2.86-3.04 (m, 12H), 4.10-4.23 (m, 24H), 6.99 (brs, 2H), 7.52 (brs, 4H), 7.70-7.75 (m, 6H), 7.84 (brs, 8H); ^{13}C NMR (151 MHz, $CDCl_3$, δ): 145.7, 145.1, 144.4, 143.0, 137.7, 134.3, 132.6, 132.3, 131.6, 131.2, 130.5, 130.3, 127.1, 116.1, 77.6, 76.4, 40.9, 40.7, 40.7, 32.1, 31.6, 30.9, 30.6, 30.5, 30.5, 30.2, 30.1, 29.9, 29.8, 29.5, 29.5, 29.4, 29.3, 24.0, 23.9, 23.3, 22.9, 22.8, 14.3, 14.3, 14.2, 11.5, 11.4, 11.4.

Synthesis of ***NCS-(BPB)$_2$-SCN***: Potassium thiocyanate (24 mg, 0.24 mmol) was dissolved in CH_2Cl_2 (0.4 mL) and MeOH (1.0 mL) and then cooled to 0 °C under a nitrogen atmosphere. A solution of Br_2 (1.2 M, 0.1 mL, 0.12 mmol) in MeOH was added dropwise to the reaction mixture. After stirring for 1 h, a solution of **(BPB)$_2$** (29 mg, 12 μmol) in THF was added dropwise to the reaction mixture. The mixture was kept at 0 °C for 1 h, and then stirred at room temperature for 4 h. The reaction was quenched with water (10 mL), and the resulting mixture was extracted with $CHCl_3$. The organic layer was extracted and dried with anhydrous sodium sulfate. After evaporation of the solvent, column chromatography was performed on silica gel (hexane:$CHCl_3$ = 1:5). Further purification was performed by recycling GPC (JAIGEL 2.5HH/3HH, $CHCl_3$ as an eluent) to give **NCS-(BPB)$_2$-SCN** as a yellow solid (15 mg, 6.0 μmol, 50%). ^{1}H NMR (400 MHz, $CDCl_3$, δ): 0.83-1.09 (m, 60H), 1.26-1.50 (m, 96H), 1.58-1.72 (m, 22H), 1.98-2.12 (m, 2H), 2.89-3.04 (m, 4H), 3.12-3.27 (m, 12H), 4.06-4.19 (m, 8H), 7.75-7.91 (m, 12H); ^{13}C NMR (151 MHz, $CDCl_3$, δ) 175.6, 174.9, 174.5, 174.4, 173.8, 152.1, 151.3, 146.2, 145.9, 145.1, 144.9, 144.4, 143.0, 141.1, 139.0, 136.3, 135.0, 134.2, 133.8, 132.2, 131.0, 130.7, 129.9, 129.5, 128.9, 127.1, 126.9, 126.8, 126.6, 122.5, 122.2, 109.6, 99.0, 98.6, 78.8, 78.7, 52.4, 52.3, 40.9, 40.7, 40.6, 32.0, 32.0, 31.6, 31.0, 30.8, 30.6, 30.3, 30.3, 30.2, 30.1, 30.0, 29.9, 29.7, 29.7, 29.6, 29.4, 29.3, 29.1, 28.2, 24.0, 23.7, 23.3, 23.2, 22.8, 14.3, 11.5, 11.4.

The same procedure was used for the synthesis of **NCS-(BPB)$_3$-SCN** (11 mg, 53%).
NCS-(TBID)$_3$-SCN: Yellow solid; 1H-NMR (600 MHz, $CDCl_3$, δ) 0.80-1.06 (m, 115H), 1.20-1.42 (m, 128H), 1.61 (s, 15H), 1.72 (brs, 8H), 1.86 (brs, 2H), 2.02 (brs, 2H), 2.92-3.22 (m, 12H), 4.19 (m, 24H), 7.76-7.85 (m, 18H); ^{13}C NMR (151 MHz, $CDCl_3$, δ): 146.5, 146.2, 145.7, 144.4, 144.4, 137.7, 133.9, 132.6, 131.6, 130.5, 129.8, 127.2, 127.1, 126.9, 117.8, 116.6, 115.7, 114.8, 112.4, 109.9, 102.1, 77.6, 76.4, 70.7, 40.9, 40.7, 32.1, 32.0, 31.6, 31.1, 30.6, 30.6, 30.5, 30.1, 30.0, 29.9, 29.8, 29.5, 29.4, 29.3, 24.0, 23.9, 23.3, 22.8, 22.8, 14.3, 14.3, 14.2, 11.5, 11.4.

Computational Details

All calculations were conducted using Gaussian 09 program.[52] The geometry was optimized with the restricted Becke Hybrid (B3LYP) at 6-31 G(d,p) level.

3.10 References

1. In “Molecular Architectonics: The Third Stage of Single Molecule Electronics”; Ogawa T,. Springer, **2017**.
2. Facchetti, A. *Chem. Mater.* **2011**, *23*, 733-758.
3. Heimel, G.; Salzmann, I.; Duhm, S.; Koch, N. *Chem. Mater.* **2011**, *23*, 359-377.
4. Su, T. A.; Neupane, M.; Steigerwald, M. L.; Venkataraman, L.; Nuckolls, C. *Nat. Rev. Mater.* **2016**, *1* 1.
5. Valenti, K.; Aveynier, E.; Leauté, S.; Laporte, F.; Hadjian, A. J. *Atherosclerosis* **1999**, *147*, 17-24.
6. Li, H. Y.; Brédas, J. L. Developing molecular-level models for organic field-effect transistors. *Natl. Sci. Rev.* **2021**, *8*, nwaa167.
7. Liu, C.; Huang, K. R.; Park, W. T.; Li, M. M.; Yang, T. Z.; Liu, X. Y.; Liang, L. J.; Minari, T.; Noh, Y. Y. *Mater. Horiz.* **2017**, *4*, 608-618.
8. Pradhan, R.; Khandelwal, K.; S, S. S.; Panda, S. J.; Purohit, C. S.; Bag, B. P.; Singhal, R.; Liu, W. R.; Zhu, X. Z.; Sharma, G. D.; Mishra, A. *Solar Rrl* **2023**, *7*, 2300487.
9. Sarkar, T.; Schneider, S. A.; Ankonina, G.; Hendsbee, A. D.; Li, Y. N.; Toney, M. F.; Frey, G. L. *Chem. Mater.* **2020**, *32*, 7338-7346.
10. McCreery, R. L. Molecular electronic junctions. *Chem. Mater.* **2004**, *16*, 4477-4496.
11. Sun, L.; Diaz-Fernandez, Y. A.; Gschneidtner, T. A.; Westerlund, F.; Lara-Avila, S.; Moth-Poulsen, K. *Chem. Soc. Rev.* **2014**, *43*, 7378-7411.
12. Tao, N. J. *Nat. Nanotechnol.* **2006**, *1*, 173-181.
13. Xiang, D.; Wang, X. L.; Jia, C. C.; Lee, T.; Guo, X. F. *Chem. Rev.* **2016**, *116*, 4318-4440.
14. Choi, S. H.; Kim, B.; Frisbie, C. D. *Science* **2008**, *320*, 1482-1486.
15. Ie, Y.; Okamoto, Y.; Inoue, T.; Tone, S.; Seo, T.; Honda, Y.; Tanaka, S.; Lee, S. K.; Ohto, T.; Yamada, R.; Tada, H.; Aso, Y. *J. Phys. Chem. Lett.* **2019**, *10*, 3197-3204.
16. Liu, H. M.; Zhao, Z. Z.; Wang, N.; Yu, C.; Zhao, J. W. *J. Comput. Chem.* **2011**, *32*, 1687-1693.
17. Yamada, R.; Kumazawa, H.; Noutoshi, T.; Tanaka, S.; Tada, H. *Nano Lett.* **2008**, *8*, 1237-1240.
18. Yamada, R.; Kumazawa, H.; Tanaka, S.; Tada, H. *Appl. Phys. Exp.* **2009**, *2*, 025002.
19. Chen, F.; Li, X. L.; Hihath, J.; Huang, Z. F.; Tao, N. J. *J. Am. Chem. Soc.* **2006**, *128*, 15874-15881.
20. Ie, Y.; Tanaka, K.; Tashiro, A.; Lee, S. K.; Testa, H. R.; Yamada, R.; Tada, H.; Aso, Y. *J. Phys. Chem. Lett.* **2015**, *6*, 3754-3759.
21. Li, X. L.; He, J.; Hihath, J.; Xu, B. Q.; Lindsay, S. M.; Tao, N. J. *J. Am. Chem. Soc.* **2006**, *128*, 2135-2141.
22. Ohto, T.; Inoue, T.; Stewart, H.; Numai, Y.; Aso, Y.; Ie, Y.; Yamada, R.; Tada, H. *J. Phys. Chem. Lett.* **2019**, *10*, 5292-5296.
23. Ohto, T.; Tashiro, A.; Seo, T.; Kawaguchi, N.; Numai, Y.; Tokumoto, J.; Yamaguchi, S.; Yamada, R.; Tada, H.; Aso, Y.; Ie, Y. *Small* **2021**, *17*, 2006709.
24. Troisi, A.; Ratner, M. A. *Small* **2006**, *2*, 172-181.
25. Venkataraman, L.; Klare, J. E.; Nuckolls, C.; Hybertsen, M. S.; Steigerwald, M. L. *Nature* **2006**, *442*, 904-907.
26. Hines, T.; Diez-Perez, I.; Hihath, J.; Liu, H. M.; Wang, Z. S.; Zhao, J. W.; Zhou, G.; Muellen, K.; Tao, N. J. Transition from Tunneling to Hopping in Single Molecular Junctions by Measuring Length and Temperature Dependence. *J. Am. Chem. Soc.* **2010**, *132*, 11658-11664.

27. Ouyang, C.; Hashimoto, K.; Tsuji, H.; Nakamura, E.; Majima, Y. *Acs Omega* **2018**, *3*, 5125-5130.
28. Aradhya, S. V.; Venkataraman, L. *Nat. Nanotechnol.* **2013**, *8*, 399-410.
29. Choi, S. H.; Risko, C.; Delgado, M. C. R.; Kim, B.; Brédas, J. L.; Frisbie, C. D. *J. Am. Chem. Soc.* **2010**, *132*, 4358-4368.
30. Korol, R.; Kilgour, M.; Segal, D. *J. Chem. Phys.* **2016**, *145*, 224702.
31. Mateus, P.; Jacquet, A.; Méndez-Ardoy, A.; Boulloy, A.; Kauffmann, B.; Pecastaings, G.; Buffeteau, T.; Ferrand, Y.; Bassani, D. M.; Huc, I. *Chem. Sci.* **2021**, *12*, 3743-3750.
32. Metzger, R. M. Unimolecular Electronics. *Chem. Rev.* **2015**, *115*, 5056-5115.
33. Pitié, S.; Dappe, Y. J.; Maurel, F.; Seydou, M.; Lacroix, J. C. *J. Phys. Chem. Lett.* **2024**, *15*, 6996.
34. Zhao, X. T.; Huang, C. C.; Gulcur, M.; Batsanov, A. S.; Baghernejad, M.; Hong, W. J.; Bryce, M. R.; Wandlowski, T. *Chem. Mater.* **2013**, *25*, 4340-4347.
35. Kocherzhenko, A. A.; Grozema, F. C.; Vyrko, S. A.; Poklonski, N. A.; Siebbeles, L. D. A. *J. Phys. Chem. C* **2010**, *114*, 20424-20430.
36. Berlin, Y. A.; Hutchison, G. R.; Rempala, P.; Ratner, M. A.; Michl, J. *J. Phys. Chem. A* **2003**, *107*, 3970-3980.
37. Bixon, M.; Jortner, J. Charge transport in DNA via thermally induced hopping. *J. Am. Chem. Soc.* **2001**, *123*, 12556-12567.
38. Segal, D.; Nitzan, A.; Davis, W. B.; Wasielewski, M. R.; Ratner, M. A *J. Phys. Chem. B* **2000**, *104*, 3817-3829.
39. Terao, J.; Wadahama, A.; Matono, A.; Tada, T.; Watanabe, S.; Seki, S.; Fujihara, T.; Tsuji, Y. *Nat. Commun.* **2013**, *4*, 1691.
40. Asakawa, R.; Yokoyama, S.; Yamada, R.; Maeda, S.; Ohto, T.; Tada, H.; Ie, Y. *J. Am. Chem. Soc.* **2024**, *146*, 23529-23536.
41. Ie, Y.; Okamoto, Y.; Inoue, T.; Seo, T.; Ohto, T.; Yamada, R.; Tada, H.; Aso, Y. *J. Am. Chem. Soc.* **2021**, *143*, 599-603.
42. Rocha, A. R.; García-Suárez, V. M.; Bailey, S.; Lambert, C.; Ferrer, J.; Sanvito, S. *Phys. Rev. B* **2006**, *73*, 085414.
43. Rungger, I.; Sanvito, S. *Phys. Rev. B* **2008**, *78* 085414.
44. Ohto, T.; Rungger, I.; Yamashita, K.; Nakamura, H.; Sanvito, S. *Phys. Rev. B* **2013**, *87*, 205439.
45. Soler, J. M.; Artacho, E.; Gale, J. D.; García, A.; Junquera, J.; Ordejón, P.; Sánchez-Portal, D. *J. Phys. Condens. Matter.* **2002**, *14*, 2745-2779.
46. Perdew, J. P.; Burke, K.; Ernzerhof, M. Generalized gradient approximation made simple. *Phys. Rev. Lett.* **1996**, *77*, 3865-3868.
47. Park, S.; Jo, J. W.; Jang, J.; Ohto, T.; Tada, H.; Yoon, H. J. *Nano Lett.* **2022**, *22*, 7682-7689.
48. Jang, J.; Jo, J. W.; Ohto, T.; Yoon, H. J. *J. Am. Chem. Soc.* **2024**, *146*, 4922-4929.
49. Li, Y. Q.; Xiang, L. M.; Palma, J. L.; Asai, Y.; Tao, N. J. *Nat. Commun.* **2016**, *7*, 11294.
50. Hsu, C. P. *Phys. Chem. Chem. Phys.* **2020**, *22*, 21630-21641.
51. Kühne, T. D.; Iannuzzi, M.; Del Ben, M.; Rybkin, V. V.; Seewald, P.; Stein, F.; Laino, T.; Khaliullin, R. Z.; Schütt, O.; Schiffmann, F.; et al. *J. Chem. Phys.* **2020**, *152*, 194193.
52. Gaussian 09, Revision D.01, M. J. Frisch, G. W. Trucks, H. B. Schlegel, G. E. Scuseria, M. A. Robb, J. R.

Cheeseman, G. Scalmani, V. Barone, G. A. Petersson, H. Nakatsuji, X. Li, M. Caricato, A. Marenich, J. Bloino, B. G. Janesko, R. Gomperts, B. Mennucci, H. P. Hratchian, J. V. Ortiz, A. F. Izmaylov, J. L. Sonnenberg, D. Williams-Young, F. Ding, F. Lipparini, F. Egidi, J. Goings, B. Peng, A. Petrone, T. Henderson, D. Ranasinghe, V. G. Zakrzewski, J. Gao, N. Rega, G. Zheng, W. Liang, M. Hada, M. Ehara, K. Toyota, R. Fukuda, J. Hasegawa, M. Ishida, T. Nakajima, Y. Honda, O. Kitao, H. Nakai, T. Vreven, K. Throssell, J. A. Montgomery, Jr., J. E. Peralta, F. Ogliaro, M. Bearpark, J. J. Heyd, E. Brothers, K. N. Kudin, V. N. Staroverov, T. Keith, R. Kobayashi, J. Normand, K. Raghavachari, A. Rendell, J. C. Burant, S. S. Iyengar, J. Tomasi, M. Cossi, J. M. Millam, M. Klene, C. Adamo, R. Cammi, J. W. Ochterski, R. L. Martin, K. Morokuma, O. Farkas, J. B. Foresman, and D. J. Fox, Gaussian, Inc., Wallingford CT, **2013**.

Conclusion

The findings obtained in this thesis are summarized as follows:

Chapter 1. The author successfully developed the fused π-conjugated molecule **BDT-NTz**, which is composed of the **NTz** backbone exhibiting significant intermolecular interactions. **BDT-NTz** demonstrated relatively good mobility in OFETs, attributed to its strong intermolecular interactions and rigid structure. Furthermore, by precisely controlling the energy levels through the use of the D-A-D type structure, it was revealed that **BDT-NTz** functions not only as a p-type material but also as an n-type material in solar cells.

Chapter 2. The author developed periodically twisted molecular wires based on a fused unit. By combining the significant reduction of λ through the use of fused-ring structures with the small ΔE_{hs} resulting from the introduction of the twisted structure, the author achieved a reduction in E_a and realized high-efficiency long-range hopping charge transport.

Chapter 3. To evaluate the structural characteristics of the hopping site **TBID** developed in chapter 2 in more detail, the author developed **BPB** by removing the fused structure from **TBID**. Theoretical calculations indicated that **BPB**, compared to **TBID**, exhibited larger λ and injection barriers, as well as a broader distribution of the HOMO. Moreover, molecular wires incorporating **BPB** as the hopping site showed lower conductance (G) compared to those composed of **TBID**. From these results, it was demonstrated that the strategy of using fused structures as hopping sites is essential for improving the efficiency of intramolecular hopping charge transport.

The findings in this thesis not only contribute to improving the single-molecule electrical conductance properties of long-chain molecular wires via hopping transport but are also effective in enhancing the efficiency of organic electronics and are expected to serve as a basis for further advances in these fields.

List of publications

1 A Fused π-Extended Molecule Containing an Electron-Accepting Naphthobisthiadiazole and its Incorporation into a Copolymer: Synthesis, Properties, and Semiconducting Performance
Asakawa, R.; Seo, T.; Yokoyama, S.; Ie, Y.
Polym. J. **2023**, *55*, 451-461.

2 Periodically Twisted Molecular Wires Based on a Fused Unit for Efficient Intramolecular Hopping Transport
Asakawa, R.; Yokoyama, S.; Yamada, R.; Maeda, S.; Ohto, T.; Tada, H.; Ie, Y.
J. Am. Chem. Soc. **2024**, *146*, 23529-23536.

3 Annelated vs. Non-Annelated Hopping Sites in Periodically Twisted Molecular Wires
Asakawa, R.; Yokoyama, S.; Yamada, R.; Ohto, T.; Tada, H.; Ie, Y.
Bull. Chem. Soc. Jpn. Accepted.

List of supplementary publication

1 Syntheses of Optically Active V-Shaped Molecules: Relationship Between their Chiroptical Properties and the Orientation of the Stacked π-Electron System
Asakawa, R.; Tabata, D.; Miki, N.; Tsuchiya, M.; Inoue, R.; Morisaki, Y.
Eur. J. Org. Chem. **2021**, 5725-5731.

Copyrights

Acknowledgements

The author would like to express his sincere gratitude to Professor Yutaka Ie, SANKEN (Institute of Scientific and Industrial Research), Osaka University for his thoughtful supervision and valuable help throughout this work. The author wishes to express his deeply thanks to Professor Michiya Matsusaki, Division of Applied Chemistry, Graduate School of Engineering, Osaka University for his reviewing this dissertation with helpful comments and suggestions. The author also greatly appreciates Professor Mamoru Fujitsuka for reviewing this dissertation with kind comments and suggestions.

The author wishes to make a grateful acknowledgement to Assistant Professor Soichi Yokoyama for his continuous guidance and invaluable advice during this study. The author is sincerely grateful to Assistant Professor Seihou Jinnai and Assistant Professor Naoki Ando for the valuable discussions, and heartly encouragement.

The author is indebted to Professor Hirokazu Tada, Division of Frontier Materials Science, Graduate School of Engineering Science, Osaka University and Associate professor Ryo Yamada for the single-molecule conductance measurement.

The author would like to thank Associate Professor Tatsuhiko Ohto, Division of Materials Design and Innovation Engineering, Graduate School of Engineering, Nagoya University, and Dr. Seiya Maeda, Division of Frontier Materials Science, Graduate School of Engineering Science, Osaka University for the theoretical analysis.

The author would like to express his deepest gratitude to Professor Akinori Saeki, Division of Applied Chemistry, Graduate School of Engineering, Osaka University for his assistance in PYS measurement.

The author is grateful to Professor Atsushi Wakamiya, Institute for Chemical Research, Kyoto University for the PYSA measurement.

The author would like to offer his special thanks to Professor Kenji Matsuda, Department of Synthetic Chemistry and Biological Chemistry, Graduate School of Engineering, Kyoto University and Assistant Professor Daiki Shimizu for the measurement of fluorescence lifetime and absolute quantum yield.

The author would like to express his gratitude to Professor Yasuhiro Morisaki, Department of Applied Chemistry for Environment, School of Biological and Environmental Sciences, Kwansei Gakuin University, and Assistant Professor Ryo Inoue, Department of Material Science, Graduate School of Science, University of Hyogo for the constructive comments and warm encouragement.

The author would like to Professor Toshiyuki Hamura, Department of Applied Chemistry for Environment, School of Biological and Environmental Sciences, Kwansei Gakuin University for his heartly encouragement.

The author would like to express his gratitude to Professor Masateru Taniguchi, SANKEN, Osaka University and Associate Professor Makusu Tsutsui and Assistant Professor Yuki Komoto and Ms. Sanae Murayama for the encouragement comments.

The author would like to express his appreciation to Dr. Yasuo Norikane, Electronics and Photonics Research Institute, National Institute of Advanced Industrial Science and Technology (AIST) and his group members for the valuable comments and warm encouragement.

The author particularly grateful to Professor Daniel T. Gryko, The Institute of Organic Chemistry of the Polish Academy of Sciences, Poland and Dr. Olena Vakuliuk, as well as his group members for encouragement comments and heartful support.

The author wishes to thank Material Analysis Center, SANKEN, and the Instrumental Analysis Center, Graduate School of Engineering, Osaka University, for measurement of spectral and analysis data.

The author thank all the members and alumini of Ie laboratory for their useful advices and discussions; Specially Appointed Professor Yoshito Tobe, Specially Appointed Professor Mikiji Miyata, Specially Appointed Professor Toshihiro Onishi, Specially Appointed Professor Hiroaki Sasai, Specially Appointed Professor Kaori Ando, Specially Appointed Assistant Professor Chatterjee Shreyam, Dr. Hajime Nitta, Dr. Keitaro Yamamoto, Dr. Navya Chauhan, Mr. Takuji Seo, Ms. Rumi Ozawa, Mr. Masaharu Matsumoto, Mr. Yasushi Hosoda, Ms. Yoshimi Fujiki, Ms. Yuka Yamauchi, Ms. Ayumi Oi, Mr. Kai Wang, Mr. Naoto Shimohara, Ms. Sakura Utsunomiya, Mr. Hiroki Mori, Mr. Kazuki Yukumatsu, Ms. Reina Yamada, Mr. Mikito Maruyama, Ms. Marina Kato, Mr. Yukiya Nagata, Mr. Yuto Shiono, Mr. Haruki Nishimura, Mr. Naoya Tagashira for their helpful suggestions and creating a pleasant atmosphere.

The author acknowledges Grant-in Aid for Research Fellowship for Young Scientists from the Japan Society for the Promotion of Science (JSPS) and Program for Leading Graduate Schools: Interactive Materials Science Cadet Program.

Finally, the author would like to express his sincerest thanks to his parents, Atsushi Asakawa and Masumi Asakawa for their perpetual support and affectionate encouragement.

Ryo Asakawa

Suita, Osaka

January 2025